SINGLE-CELL TRANSCRIPTOME ANALYSIS OF METABOLIC STRESS RESPONSE IN MACROPHAGES

A Dissertation

Submitted in Partial Fulfilment of the

Requirements for the Degree of

Doctor rerum naturalium (Dr. rer. nat.)

to the Department of Biology, Chemistry and Pharmacy

of Freie Universität Berlin

by

Maria Metsger

Berlin, 2017

Supervisor: Dr. Sascha Sauer

Second examiner: Prof. Dr. Stephan Sigrist

Date of defense: 29.11.2017

Acknowledgements

Table of Contents

1 Introduction

1.1 Epidemiology of diabetes mellitus

Diabetes has become a global burden in recent decades, causing premature deaths and a number of complications including cardiovascular disease, blindness, kidney failure and neuropathy [1]. According to the estimation made by the International Diabetes Federation (IFD) for 2015, 415 million people worldwide have diabetes, which corresponds to 8,8 % of the total world population [2]. By 2040 this number is expected to reach 642 million (10,4 % of the world population). Type 2 diabetes accounts for about 90 % of all diabetes cases [1, 2] and is rapidly expanding worldwide due to urbanization, i.e. changes in diet, lifestyle and other aspects of human life.

Regional prevalence of diabetes is shown in Figure 1-1. The top five countries with the highest numbers of adults suffering from diabetes include China (109,6 M), India (69,2 M), USA (29,3 M), Brazil (14,3 M) and the Russian Federation (12,1 M).
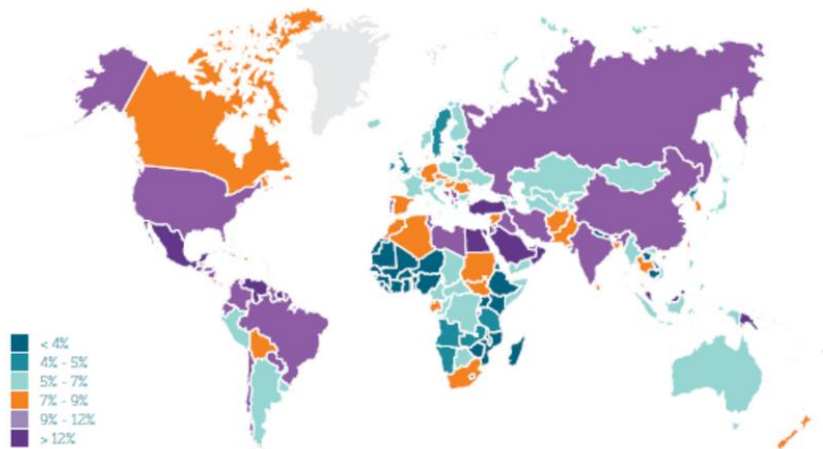
Figure 1-1 Estimated prevalence of diabetes in adults (20-79), 2015.
Figure source: IDF diabetes atlas -7th edition

1.2 Chronic inflammation in obesity-induced insulin resistance and type 2 diabetes.

1.2.1 Chronic inflammation in obesity

The dramatic increase in cases of type 2 diabetes (T2D) is largely due to an epidemic of obesity caused by lifestyle and diet changes, in particular calorie-rich diet. Often obese patients develop insulin resistance leading to the development of T2D. Patients with obesity are highly heterogeneous, differing in body mass index (BMI), age, genetic background and numerous other parameters influencing the risk in developing T2D [3-5]. Molecular mechanisms underlying the progression of insulin resistance include activation of inflammatory pathways, impaired lipid metabolism, endoplasmatic reticulum stress, oxidative stress and abnormal adipokine secretion. Essentially, all these processes contribute to chronic low-grade inflammation leading to insulin resistance [6, 7].

The first evidence of the connection between inflammation and obesity was shown in 1993 when G.S. Hotamisligil and B. M. Spiegelman found an increased level of TNFα secretion from adipose tissue of obese rodents [8]. It was later observed that not only TNFα, but many other pro-inflammatory molecules are overexpressed in obesity including interleukin 1-beta (IL1β), interleukin 6 (IL6), macrophage inhibitory factor (MIF), monocyte chemotactic protein 1 (MCP1) and others [6, 7].

1.2.2 Role of macrophages in chronic inflammation

A major mechanism contributing to chronic inflammation development is the accumulation and activation of proinflammatory immune cells. It may occur not only in adipose tissue, but also in the liver, skeletal muscles and pancreatic islets (Figure 1-2). Low-grade inflammation represents a cumulative effect of the diversity of activated immune cells aggregated in tissue; for example, macrophages play a major role in this process. Macrophages represent the most abundant pro-inflammatory immune cells in obese tissues. Notably, adipose tissue macrophages may make up to as much as 40 % of obese adipose tissue mass [9].

Recruitment of adipose tissue macrophages in obese conditions is prompted by adipocyte secretion of chemoattractant molecules MCP1 and LTB4, which are recognized by corresponding receptors CCR2 and BLT1 [10-13]. After recruitment and activation, macrophages also express attractant chemokines promoting further recruitment and inflammation in a feed-forward manner.

Not only increased macrophage recruitment, but also impaired emigration from adipose to lymphoid tissue contributes to increased macrophage accumulation. This phenomenon

was mainly studied in the context of atherosclerosis, where accumulation of lipid-loaded macrophages causes local inflammation in atherosclerotic plaques [14]. Macrophage recruitment to lymphoid tissues can be regulated by chemokines CCL19 and CCL21, expressed in macrophages, which bind to a CCR7 receptor.

In addition to macrophages, a number of other pro-inflammatory immune cells (such as neutrophils, mast cells, B lymphocytes, CD8+ T lymphocytes and CD4+ Th1 cells) are accumulated in obese adipose tissue [15-18]. Additionally, numbers of immune modulating cells including CD4+ regulatory T cells (Treg), Th2 cells, eosophils and natural killer cells are typically decreased in obesity [15, 19].
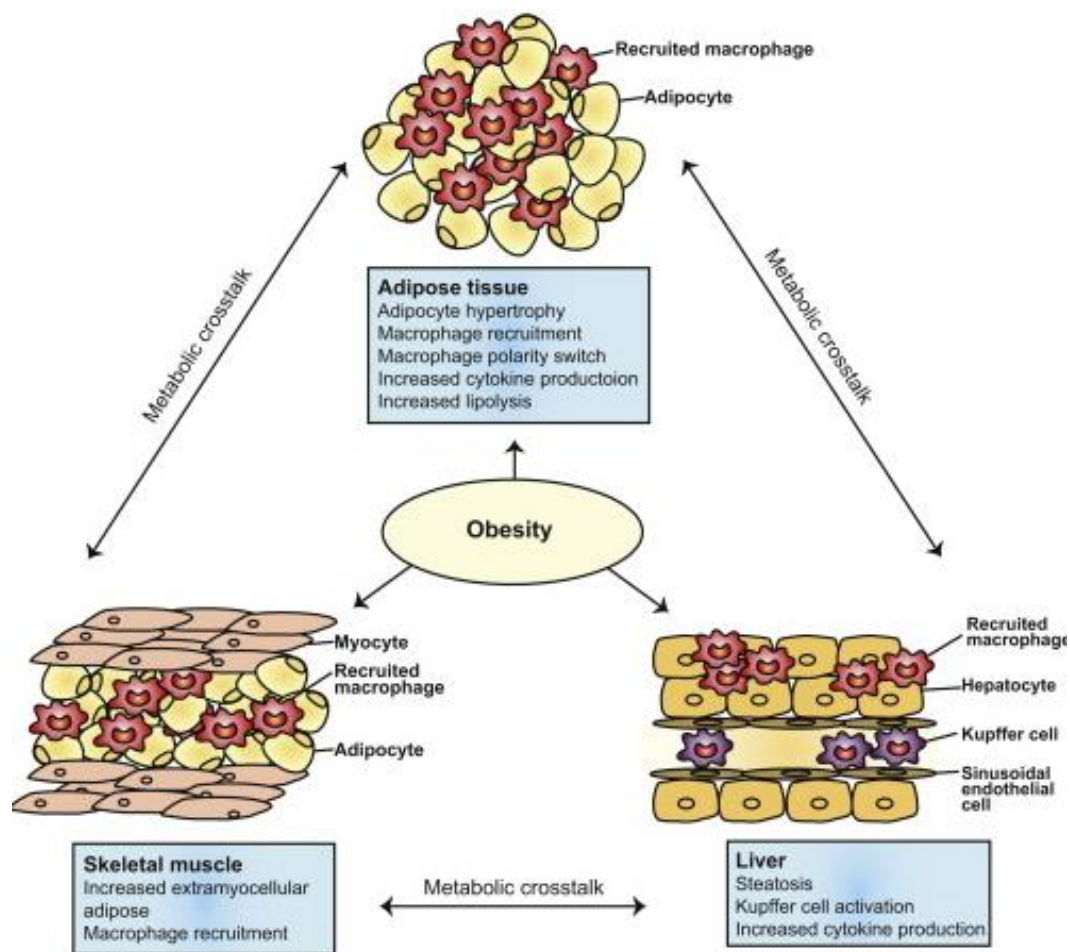
Figure 1-2 Obesity-induced inflammation in adipose tissue, skeletal muscle and liver.
Figure source: McNelis, J.C. and J.M. Olefsky, Macrophages, immunity, and metabolic disease. Immunity, 2014. 41(1): p. 36-48

In the liver, there are two main types of macrophages: Kupfer cells (KCs) and recruited hepatic macrophages (RHM). Kupfer cells play an important regulatory role in supporting

tissue homeostasis, whereas recruited hepatic macrophages are attracted to the liver during obesity and develop pro-inflammatory phenotype, causing hepatic insulin resistance [20].

Recent studies have shown that local inflammation is also developed in skeletal muscles and is caused by macrophage accumulation in intermuscular adipose depots [21, 22]. Inflammation-induced insulin resistance in muscles may play a major role in the development of hyperglycemia as muscles consume up to 80 % of the glucose.

1.2.3 Macrophage plasticity and polarization

Macrophages can be found in various tissue types where they play different functional roles such as supporting tissue homeostasis, immune response, tissue repair and development regulation. They demonstrate incredible plasticity, which underlies their ability to adjust to the microenvironment and respond to diverse environmental stimuli. A number of studies have been conducted to analyse the macrophage molecular phenotype in homeostasis and disease; however, the complete classification and description of the full spectrum of macrophage phenotypes is not established.

The commonly used concept of two major macrophage states describes classically activated macrophages (M1 state) and alternatively activated macrophages (M2 state) [23]. M1 macrophages are pro-inflammatory cells that were originally obtained by IFN-γ stimulation. It was shown later that other activators of toll-like receptors (such as LPS) also induce an M1 macrophage molecular phenotype [24]. Alternatively activated, or M2 macrophages were obtained via stimulation with IL4 or IL13. They show distinctions from the M1 anti-inflammatory profile and were originally linked to wound healing, as well as to Th2 type responses [25, 26].

Since the original definition of two major states was introduced, many studies have shown that the variety of macrophage phenotypes in different physiological conditions is much broader, and that there is a full spectrum of diverse macrophage states between M1 and M2 [24]. With the accumulating evidence of macrophage diversity, additional terminology appeared to describe subsets of M1/M2 states (M2a, M2b) [27-29]. Another widely-studied group of macrophages is Tumor Associated Macrophages (TAM). They are characterized by a low level of inflammation and have a specific M2-like state [24].

Macrophages differentiate to M1 state during bacterial infection and display a high expression of numerous pro-inflammatory signaling molecules: cytokines and chemokines, as well as high levels of oxygen and nitrogen radicals and superoxide anion production to increase their microbicidal activity. M1 macrophages are induced by IFNγ and TNF, produced in the organism by Natural Killer (NK) and T helper 1 (Th1) cells which

initially respond to infection. The M1 phenotype can also be induced by LPS or other pathogen-associated molecular patterns through toll-like receptor (TLR) recognition and signaling. TLR ligand activates MyD88 and TRIF-dependent signaling pathways, inducing the expression of TNF and IFNβ. This mechanism replaces signals produced by NK and Th1 cells in the stimulation of M1 polarization [30]. The key regulatory mechanism in M1 macrophages includes activation through transcription factors NFkB and AP-1, JAK-STAT signaling pathways, where STAT1 protein plays a particularly important role [24, 30, 31]. M1 cells are typically characterised by high expression of MHC class II molecules, IL12, IL1, IL23, IL6, NOS2, IRF3 and IRF5. [32].

Alternative activation of macrophages is induced by IL4 and IL13 molecules, produced mainly by Th2 cells, mast cell, eosinophils and basophils [25, 26]. IL4 and IL13 have highly overlapping functions and have been associated with host defence from parasitic infections, allergic reactions and asthma [33, 34]. IL4 is rapidly expressed during tissue injury by basophils and mast cells, promoting wound healing activity of M2 macrophages [35, 36]. It can be also expressed as a response to chitin and other components of fungi and parasites [37]. IL4-activated macrophages feature high arginase activity associated with the production of an extracellular matrix, as well as high-mannose receptor activity (associated with increased endocytosis) and upregulated MHC class II production (associated with antigen presentation activity). IL13 has specific functions in mucus secretion and tissue eosinophilia [26]. Both IL4 and IL13 molecules are recognized by the IL4-Rα receptor, and act through STAT6 and IRS2 pathways. Although IL10 was previously thought to induce the same macrophage state as IL4 and IL13, it was later shown that it has distinct effects, including more efficient deactivation of inflammatory cytokine production and antigen presenting activity [25].

With the advancement of single-cell technologies, macrophage studies will soon achieve unprecedented accuracy and sensitivity, allowing the identification of rare cell subpopulations and the pervasive molecular characterization of macrophage states. However, it is common that newly described macrophage phenotypes, along with their nomenclature and underlying experimental approaches, are not systematic nor standardized. It is widely accepted in the scientific community that clear nomenclature and the experimental guidelines that are being developed are essential to the advancement of macrophage-related fields [31].

1.2.4 Macrophage polarization in obesity

Adipose tissue is one of the main tissues that contributes to the development of insulin resistance. The chronic inflammation characteristic for obese adipose tissue is caused by highly increased macrophage infiltration and activation. In lean state, adipose tissue

resident macrophages have an M2-like phenotype and can be distinguished as CD11c negative. They produce anti-inflammatory molecules such as IL10 and IL1RA and are associated with metabolic homeostasis [25, 26].

In obesity, newly recruited macrophages acquire a pro-inflammatory M1 phenotype that can be distinguished by the expression of CD11c [38]. A number of studies have shown that there is a direct correlation between the ratio of M1/M2 macrophages and insulin resistance. It has been demonstrated that shifting the ratio back to the prevalence of M2 macrophages in obesity decreases inflammation in adipose tissue and improves insulin sensitivity [39].
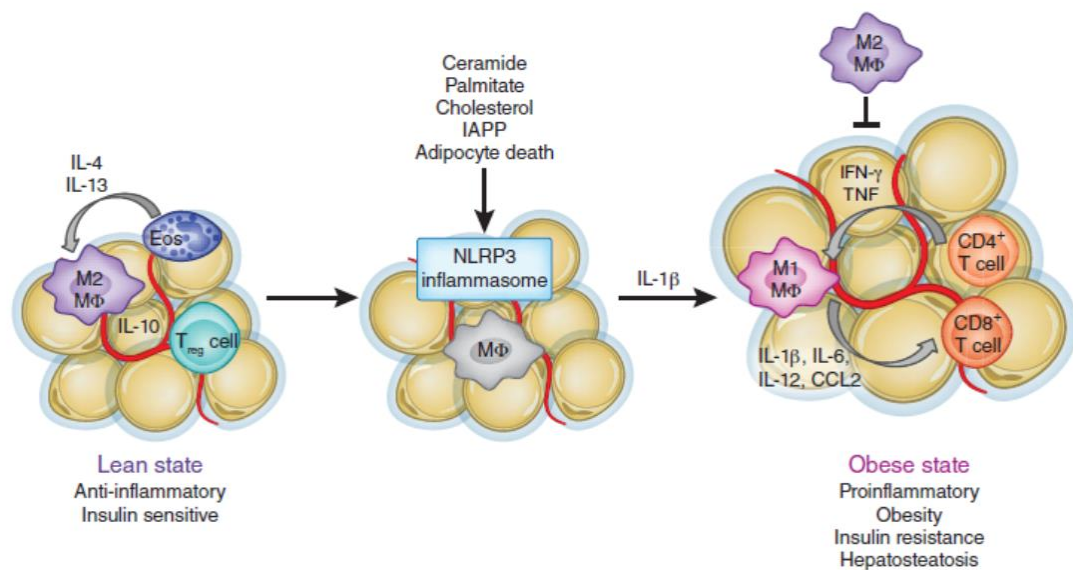
Figure 1-3 Obesity-induced inflammasome activation and macrophage polarization in adipose tissue.
Figure source: Kanneganti, T.D. and V.D. Dixit, Immunological complications of obesity. Nat Immunol, 2012. 13(8): p. 707-12.

Recent studies on the molecular basis of M1 macrophage activation in obesity demonstrate the significant role of inflammasomes. Inflammasomes recognise pathogen-derived molecules with an NLR or AIM2 sensor and stimulate the production of pro-inflammatory cytokines through ASC and caspase-9 pathways. Apart from the major role of inflammasomes in pathogen-induced innate immunity, the pro-inflammatory activation can be also caused by elevated levels of other compounds present in the blood of obese patients, such as free fatty acids, cholesterol, islet amyloid polypeptides (IAPP) and apoptotic adipocytes [40]. Mice who are deficient in key inflammasome molecules such

as caspase-1, ASC, NLRP3 and IL1β showed improved insulin sensitivity and glucose tolerance when in high- fat diet conditions [41].

Inflammasome-activated IL1β induces recruitment of macrophages that further induce pro-inflammatory signaling by secreting IL1β, IL6, IL12, CCL2 and other chemokines and cytokines [40, 42, 43]. These processes contribute to the attraction of other immune cells such as CD4+ and CD8+ T-cells. Activated T-cells further increase inflammation with secretion of IFNγ and TNF (Figure 1-3) [40].

1.2.5 Inflammation induced by elevated free fatty acids

It has been well established that an elevated concentration of free fatty acids (FFAs) or nonesterified fatty acids (NEFAs) in blood plasma are associated with obesity and insulin resistance [42, 43]. Consumed dietary fatty acids circulate in blood plasma as free fatty acids or can be deposited in adipocytes. Adipose tissue fat can be released from adipocytes by lipolysis. The increase of white adipose tissue (WAT) mass in obesity consequently leads to an increase of plasma FFAs. Particularly in obese adipose tissue surroundings, ATMs and other immune cells are constantly exposed to a high concentration of FFAs released by neighbouring adipocytes.

Although the increase of FFA levels between obese and lean conditions is evident, it has been systematically reviewed that the increase of WAT often does not lead to a proportional increase of FFAs concentration, as there are mechanisms inhibiting further increase of FFAs. It has been demonstrated that lipolysis per kilogram of WAT is reduced in obese conditions, leading to a controversial relationship between WAT mass and concentration of FFAs. It has also been reported that key enzymes controlling fat mobilization, such as hormone-sensitive lipase and adipose triglyceride lipase, are downregulated in obese individuals [44, 45]. These findings indicate that further research is necessary to understand the complexity of FFA metabolism in obesity.

Circulating FFAs are known to induce inflammatory pathways in various cell types such as adipocytes, macrophages, hepatocytes etc. via toll-like receptor associated signaling. The exact mechanism of interaction between toll-like receptors and circulating FFAs was unknown before it was discovered in 2012 that fetuin A (FetA) acts as an adaptor protein between FFAs and TLR4 (Figure 1-4) [46]. In this study Pal et al. showed that the concentration of FetA, a liver-secreted protein, is increased in obese humans and mice. HFD-fed FetA knockout mice featured improved glucose homeostasis and did not develop adipose tissue inflammation. Overall, the discovery of FetA provided new opportunities for potentially targeting obesity-related inflammation without effecting crucial functions of the innate immune system [47].
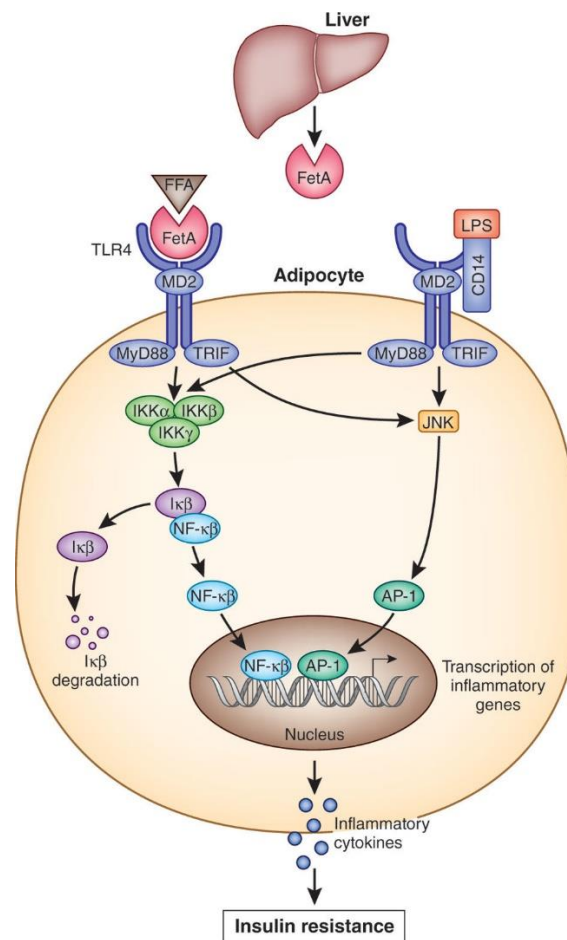
Figure 1-4 Role of fetuin A in free fatty acid induced chronic inflammation and insulin resistance.
Liver-produced glycoprotein fetuin A acts as an adaptor between FFAs and toll-like receptor 4 to activate pro-inflammatory cytokine expression in adipocyte.
Figure source: Heinrichsdorff, J. and J.M. Olefsky, Fetuin-A: the missing link in lipid-induced inflammation. Nat Med, 2012. 18(8): p. 1182-3.

This discovery was followed by a systematic study of 347 healthy individuals with a high risk of the development of type 2 diabetes or cardiovascular disease (CVD) [46]. In this study subjects were divided into four groups depending on the level of blood concentration (high/low) of FFAs and FetA, and insulin sensitivity was determined for these individuals. There was a decline of insulin sensitivity with the increase of FFA and FetA concentration, but only in groups where both FFAs and FetA were highly abundant. This result indicates the importance of both FFA and FetA concentration to define the optimal therapeutic strategy.

1.2.6 Role of saturated and unsaturated fatty acids

The dietary fatty acids consumed with food can be divided into two major groups according to their chemical structure: saturated and unsaturated fatty acids. In saturated fatty acids all carbon atoms are linked by single bonds, whereas in unsaturated fatty acids one or more double bonds are present (monounsaturated and polyunsaturated fatty acids). Obesity-induced pathological processes including low grade inflammation triggered by activation of inflammasome and toll-like receptor signaling are mainly associated with saturated fatty acids (palmitic acid, stearic acid, myristic acid etc.) [46, 47]. Saturated fats are mainly present in meat and dairy products such as butter and cheese [48]. In high-fat western diet, associated with obesity, the balance between fat types is shifted towards high content of saturated fatty acids, and this misbalance is linked to high risks of cardiovascular disease, metabolic syndrome and obesity-induced T2D.

In contrast, unsaturated fatty acids, in particular omega-3 fatty acids such as docosahexanoic (DHA) and eicosapentanoic (EPA) acids decrease risks of metabolic-related disorders. Unsaturated fatty acids are mainly present in fish, plant oils (olive oil, canola oil etc.) and nuts. Beneficial effects of mediterranean diet is largely attributed to the high content of unsaturated fatty acids contained in olive oil. A number of studies in animal models and human individuals have demonstrated beneficial effects of diet with increased ratio of unsaturated/saturated fatty acids in various diseases including type 2 diabetes, cardiovascular disease, Alzheimer disease and cancer [49-53]. Exact mechanisms of action in diverse physiological conditions are not completely established, however significant progress was made in recent years.

It has been shown that fatty acids can interact with G-protein coupled receptors (GPR40 (FFA1), GPR41 (FFA3), GPR43 (FFA2), GPR120 (FFA4) and GPR84) [54, 55]. In 2010 D. Y. Oh et al. discovered a key role of G-protein-coupled receptor 120 (GPR120) in insulin-sensitizing effects of omega-3 fatty acids [56]. Omega-3 acids (DHA, EPA and palmitoleate) were shown to interact with GRP120 and activate anti-inflammatory mechanisms. These authors demonstrated that impaired glucose homeostasis caused by HFD enriched with saturated fatty acids in mice were reduced by the addition of omega-3 fatty acids. This effect was achieved through GRP120 activation and was eliminated in GRP120 deficient mice. Furthermore, these authors observed that β-arrestin 2 protein is essential for anti-inflammatory effects of GRP120-dependent action of omega-3 fatty acids.

GRP120 and its pharmaceutical agonists have attracted a lot of attention in recent years for their potential in treatment of type 2 diabetes and other metabolic and inflammatory diseases. In 2014, in another study D. Y. Oh et al. demonstrated that small molecule spdA acts as a selective agonist of GPR120 *in vitro* and in obese mice *in vivo* [57]. Orally taken

spdA improved insulin sensitivity, glucose tolerance and decreased hepatic steatosis in obese mice. This finding demonstrates that GPR120 receptor agonists can potentially be used for T2D treatment.

1.2.7 Molecular pathways linking chronic inflammation and insulin resistance

Diverse pathological processes such as endoplasmatic reticulum and oxidative stress, glucotoxicity, lipotoxicity and chronic inflammation contribute to the development of insulin resistance and type 2 diabetes in obesity. Many of these processes are involved in the activation of pro-inflammatory signaling through several pathways [58] (Figure 1-5)

One of the major mechanisms causing pro-inflammatory activation in macrophages and other cells is through toll-like receptor (TLR) signaling. As was described in the previous paragraphs, circulating FFAs in plasma activate TLR2 and TLR4 receptors through adaptor protein fetuin A (Figure 1-4). TLR2/4 activation induces transcription factors nuclear factor κB (NFκB) and AP-1, which leads to the expression of multiple pro-inflammatory cytokines including TNFα and IL1β. Activation of TNFα and IL1β signaling results in insulin resistance in insulin sensitive tissues through an activation of IkB kinase (IKK) and c-Jun N-terminal kinase (JNK). These kinases inhibit insulin signaling by serine phosphorylation of insulin receptor substrate 1 (IRS1).

In addition to detrimental effects of elevated circulating FFAs, ectopic lipid storage inside tissues can also lead to insulin resistance [59]. Ectopic lipid accumulation is largely regulated by lipid transport proteins such as lipoprotein lipase (LpL), CD36 and fatty acid transport proteins (FATPs). Deletion of LdL, CD36 and FATPs in mice decreases lipid accumulation in muscles and liver and improved insulin sensitivity in high fat diet [60-62].

Lipids are accumulated in the tissues mainly in a form of intracellular diacylglycerols (DAG) or ceramides. Lipids accumulating in muscle cells and liver in non-alcoholic fatty liver disease (NAFLD) were shown to cause muscle and hepatic insulin resistance [63, 64] through the activation of specific isoforms of novel protein kinase C. Protein kinase C θ (nPKC θ) plays a role particularly in skeletal muscles [65-67], whereas PKCε and PKCδ are associated with the development of hepatic steatosis, glucose intolerance and insulin resistance in liver [68, 69].

There is growing evidence that ceramides are associated with obesity and the development of type 2 diabetes by interacting with various pathways [70]. Ceramides are produced with cells from FFAs such as palmitic acid. The underlying pathway is upregulated by TLR4 activation, mitochondrial and ER stress. Ceramides influence insulin sensitivity by directly interacting with nPKCζ that phosphorylates and inhibits the translocation of Akt/PKB. Ceramides can also activate protein phosphatase 2A (PP2A)

responsible for dephosphorylating Akt/PKB. W. L. Holland and colleagues demonstrated *in vitro* and *in vivo* that ceramides are also essential in a TLR4-regulated mechanism of insulin resistance [71]. They showed that ceramide production is induced by TLR4 signaling via the activation of IKKβ kinase and ceramide accumulation was required for the development of TLR4-dependent insulin resistance, although ceramides did not influence pro-inflammatory cytokine production.
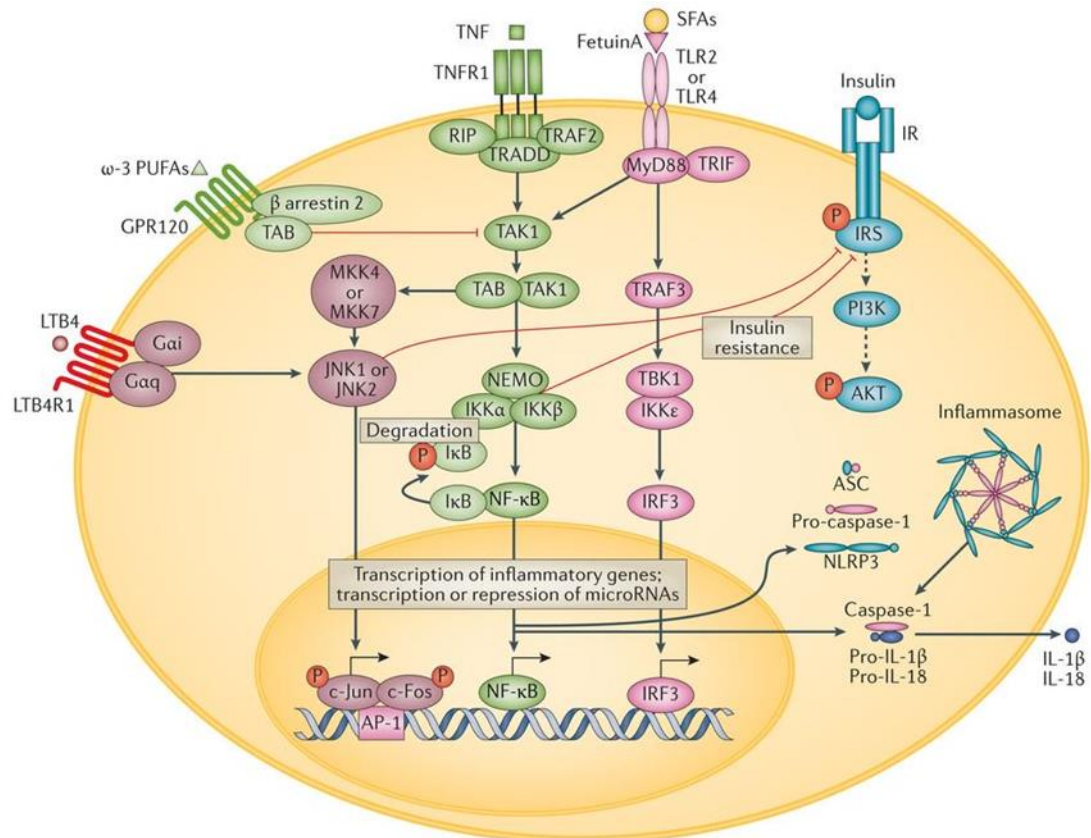
Figure 1-5 Signaling pathways involved in the development of obesity-induced chronic inflammation and insulin resistance.
Figure source: Lackey, D.E. and J.M. Olefsky, Regulation of metabolism by the innate immune system. Nat Rev Endocrinol, 2016. 12(1): p. 15-28.

Another important mechanism contributing to insulin resistance is regulated by inflammasome activation causing M1 macrophage polarization as was described in paragraph 1.2.4. The role of nucleosomal protein NLRP3 and other NLRs has been extensively studied in the context of various autoimmune disorders including arthritis, neuroinflammatory diseases and type 2 diabetes [40]. In obesity NLRP3 inflammasomes are involved in recognition of FFAs, products of lipid metabolism and products of damaged

cells - damage-associated molecular patterns (DAMPs). Inflammasome activation by these components leads to the activation of caspase-1, cleavage of pro-IL1β and pro-IL18 to their mature forms and an increased production of IL1β and IL18 [40, 70, 71].

Wen et al. demonstrated *in vivo* that HFD fed mice promoted insulin resistance via NLRP3-PYCARD activation [70]. Inflammasome activation was associated with other signaling cascades such as reactive oxygen species production, AMP-activated protein kinase and ULK1 autophagy signaling pathways. Supporting the previous knowledge, they demonstrated that only saturated fatty acid (palmitate), but not unsaturated fatty acid (oleate) induced inflammasome activation. IL1β has been shown to play a key role in inflammasome-associated development of insulin resistance acting in TNFα-dependent and independent manner. IL1β deficient mice in contrast to WT did not develop insulin resistance after 2 weeks of feeding with HFD.

B. Vandanmagsar et al. confirmed previous NLRP3-related findings from *in vitro* and *in vivo* models in type-2-diabetic patients examined before and after healthy diet and exercise-induced weight loss [71]. T2D patients exhibited significant reduction of IL1β and NLRP3 expression and improved insulin sensitivity after weight loss. B. Vandanmagsar et al. also demonstrated the NLRP3-dependent activation of mouse adipose tissue macrophages by ceramides and their role in promoting M1/M2 misbalance.

Endoplasmatic reticulum (ER) stress and unfolded protein response (UPR) are also shown to significantly contribute to metabolic dysfunctions including chronic inflammation [72]. The connection between ER stress and inflammation is regulated by several mechanisms. These involve ATF6 pathway, IRE1α and TRAF2 regulated activation of JNK and IkB kinase (IKK) and PERK-mediated signalling. All these pathways contribute to the expression of pro-inflammatory molecules such as NFκB, IL6, TNFα [73]. In obese mice fed with HFD, PERK and IRE1a phosphorylation as well as JNK activity are significantly higher than in lean state [74]. The role of ER stress in the development of insulin resistance was demonstrated in model cells and mice, deficient in XBP1 and ORP150. These proteins play a significant role in the response and regulation of ER stress. Deficiency of each of these proteins resulted in increased levels of ER stress [75] leading to glucose intolerance and insulin resistance [74, 76].

Another important mechanism connecting ER stress and inflammation in adipose tissue is associated with C/EBP homologous protein (CHOP). CHOP is a well-known transcription factor regulating cell response to various stresses including ER stress, where it plays essential roles in the activation of apoptosis. The association between CHOP expression and regulation of macrophage polarization was previously studied in different models and treatment conditions where CHOP was shown to regulate different macrophage

phenotypes leading to some controversy [77, 78]. In a recent study Suzuki et al. analysed the role of CHOP in the regulation of macrophage polarization during HFD-induced obesity in mice [79]. CHOP-deficient mice exhibited normal M1/M2 balance of macrophage states and maintained insulin sensitivity during HFD, whereas WT mice featured increased M1 polarization of macrophages and developed insulin resistance.

Another pathway linking inflammation and insulin resistance is regulated by pro-inflammatory eicosanoid leukotriene B4 (LTB4) through its specific receptor LTB4R. Several studies demonstrated its role in atherosclerosis, arthritis and insulin resistance [10, 80, 81]. In 2015 J.M Olefsky's group showed that genetic and pharmacologic depletion of LTB4 in HFD-fed mice improved glucose homeostasis and insulin sensitivity, although it did not influence the development of obesity [75].

Overall, the described studies demonstrate the complexity of the molecular basis of insulin resistance in obesity and type 2 diabetes. Nevertheless, there is evidence of the crucial role of inflammatory signalling in the development of insulin reistance. Discovery of the key regulators and missing links in molecular signalling represents an important field for future studies in obesity-induced insulin resistance and type 2 diabetes.

1.2.8 Pathways counter playing chronic inflammation and insulin resistance in obesity

As was discussed in the previous paragraphs, the ratio between classically and alternatively activated macrophages in metabolic target tissues plays a crucial role in the development of insulin resistance. Alternative macrophage activation, associated with lean state and improved insulin sensitivity, is triggered by a cumulative stimulation of other immune cells including eosinophils, regulatory T cells (Treg) and ILC2 cells. ILC2 cells induce eosinophils maturation and recruitment by producing interleukins IL5 and IL13. Eosinophils and Treg cells induce alternative M2 macrophage state through IL4 and IL10 signaling.

One of the most widely studied genes improving the pathological processes in obesity and regulating M2 macrophage activation is PPARγ. PPARγ ligands demonstrated significant insulin sensitizing effects and lowering serum glucose. In 2007 Odegaard et al. showed that PPARγ expression is required for alternative macrophage activation and maintains insulin sensitivity in obese HFD-fed mice [82]. The beneficial effects of PPARγ are not induced by the gene itself, but through its target genes [83]. The exact mechanisms of insulin sensitizing characteristics of PPARγ are not completely understood and more systematic studies are necessary to fully understand this regulatory mechanism.

Another important anti-inflammatory mechanism regulated by omega-3 fatty acids through GRP120 was described in paragraph 1.2.5. GRP120 acts through the activation of β-arrestin2/TAB1 and blocks TLR4 signaling by the isolation of Tak1 that is necessary for TLR4 signal transduction.

Transcription factor ATF3 represents another interesting anti-inflammatory regulator. D. De Nardo et al. demonstrated in 2014 a significant role of ATF3 in anti-inflammatory reprogramming of macrophages via high density lipoprotein (HDL) stimulation [84]. HDL has protective properties in atherosclerosis regulating reverse cholesterol transport by exerting anti-inflammatory effects. The authors validated the essential role of anti-inflammatory characteristics of HDL in ATF3-deficient macrophages and mice. Thus, this mechanism is also potentially interesting in the context of chronic inflammation in obesity and other metabolic complications.

1.2.9 Treatment strategies of obesity-induced type 2 diabetes

Current anti-diabetic therapies involve insulin therapy, metformin, thiazolidinediones, sulphonylureas, meglitinides, α-glucosidase inhibitors, incretin hormone-based therapy, sodium-dependent glucose co-transporter inhibitors and insulin therapy. Anti-inflammatory treatment of type 2 diabetes is an emerging approach, in particular to prevent insulin resistance [85].

Metformin is the most widely used medication of type 2 diabetes. It has a highly efficient glucose-lowering effect and relatively low and rare side effects compared to other treatments [86]. It is a first-line drug recommended by American Diabetes Association/European Association for the Study of Diabetes, both, for monotherapy and combination therapy. Despite the vital importance and efficiency of metformin as an anti-diabetic drug, it mainly effects the liver glucose production. Metformin effects on insulin sensitization and chronic inflammation have also been reported, however they are not so well described and validated systematically [83, 86-89].

Thiazolidinediones (TZD) such as rosiglitazone and pioglitazone act through the activation of PPAR receptors with particularly high affinity to PPARγ. PPARγ ligands demonstrate well-known insulin sensitizing effect. The beneficial effects of PPARγ activation are thought to be in part associated with its anti-inflammatory properties. However, several side effects were described for TZDs including weight gain, increase of low-density lipoprotein cholesterol, cardiovascular complication and others [1, 90].

Natural compounds including extracts from plants were shown to induce potential anti-inflammatory and insulin sensitizing effects [91]. In particular PPARγ agonists including

amorfrutins, found in the roots of licorice, or other plant compounds have shown potential antidiabetic effects *in vitro* and in obese mice [91, 92].

Anti-inflammatory therapies are considered to support treatment of metabolic diseases, however the advances in their application are limited so far [83]. TNFα antagonists can be potentially efficient due to the significant role of TNFα in the development of chronic inflammation. Several studies demonstrated positive effects on insulin sensitivity and glycaemia in obese non-diabetic subjects and patients with rheumatoid arthritis, psoriasis and Crohn's disease [93-96]. However, the full-scale studies on diabetic patients are still necessary to provide statistically significant effects of such treatments.

A group of studies used IL1 antagonists in T2D patients based on widely described roles of IL1β in context of obesity-related insulin resistance and diabetes. These treatments involved anakinra (an IL receptor agonist), canakinumab (human monoclonal anti-IL1 antibody) and I1β specific antibody LY2189102 [93-96]. All these treatments had moderate positive effects decreasing glycated haemoglobin, reducing inflammation and improving insulin sensitivity. These initial clinical studies demonstrated a potential of IL1 antagonists in the treatment of insulin resistance and T2D without obvious side effects.

Salsalate is another potential anti-diabetic supplement that acts through the inhibition of NFκB pathway. It was tested in several human studies including diabetic and non-diabetic patients and proved its efficiency in Phase III clinical trials [85, 97, 98]. Although salsalate treatment increased the level of LDL cholesterol in blood and urinary albumin, the patients demonstrated significant decrease in the glycated haemoglobin and overall it proved its efficiency.

Taken together, these findings demonstrate the high potential of their usage in the field of anti-inflammatory treatment in obesity and type 2 diabetes. However, it is important to develop treatments that would not affect the vital immune functions, but would precisely and more efficiently inhibit obesity-induced chronic inflammation and prevent insulin resistance.

1.3 Single-cell transcriptome analysis

1.3.1 Single-cell RNA sequencing technology

Throughout the last decade, the advancement of the Next Generation Sequencing (NGS) technology has significantly improved the sensitivity and efficiency of a variety of DNA-sequencing based methods and broadened the range of applications. Many single-cell genomics procedures were introduced and dramatically evolved over the recent years. These include methods for RNA sequencing, whole genome sequencing and analysis of

epigenetic states of individual cells. Whole transcriptome sequencing of single cells represents an engaging technology. Currently, single-cell RNA sequencing methods are based on the individual cell separation and library preparation using cell sorting, emulsion and microfluidics based methods. Here, the selected methods for single-cell RNA sequencing are briefly described. The information can be found in various reviews [99-102]

SMART (Switching Mechanism at 5' end of RNA Template) template switching technology is widely used in single-cell RNA sequencing. It was originally applied for manual single-cell RNA library preparation in multiwell plates and later was adopted for emulsion and microfluidics based methods [102-104]. In these protocols, cell lysis is directly followed by reverse transcription of polyadenylated RNA using oligo-dT primers. When reverse transcriptase reaches the 5' end of the transcript, it adds a non-template tag to the end of the first strand cDNA. In the presence of adaptor oligonucleotides hybridizing to the added tag, the reverse transcriptase switches the template and transcribes the adaptor sequence at the end of first strand cDNA, which allows the adaptor sequence incorporation into both RNA template and first strand cDNA.

SMART technology allows for cell lysis, reverse transcription and pre-amplification in one reaction without an intermediate purification and adaptor ligation step. This method allows full-length transcript coverage without a significant 3'/5' end bias. These characteristics permit it to become one of the most widely used approaches in single-cell RNA library preparation.

Commercial Fluidigm C1 system utilizes the SMART template switching protocol in microfluidics. The overview of the standard workflow is depicted in Figure 1-6 B. Individual cells are captured in microwells of the integrated fluidic circuits (IFCs) allowing the processing of the cells in a broad range of sizes (5-25 µm). Captured cells in microwells can be visualized using a light microscope. Following cell lysis, polyadenylated RNA is reverse-transcribed using cell-specific barcodes, and pre-amplified for further library preparation following harvesting from the IFC.
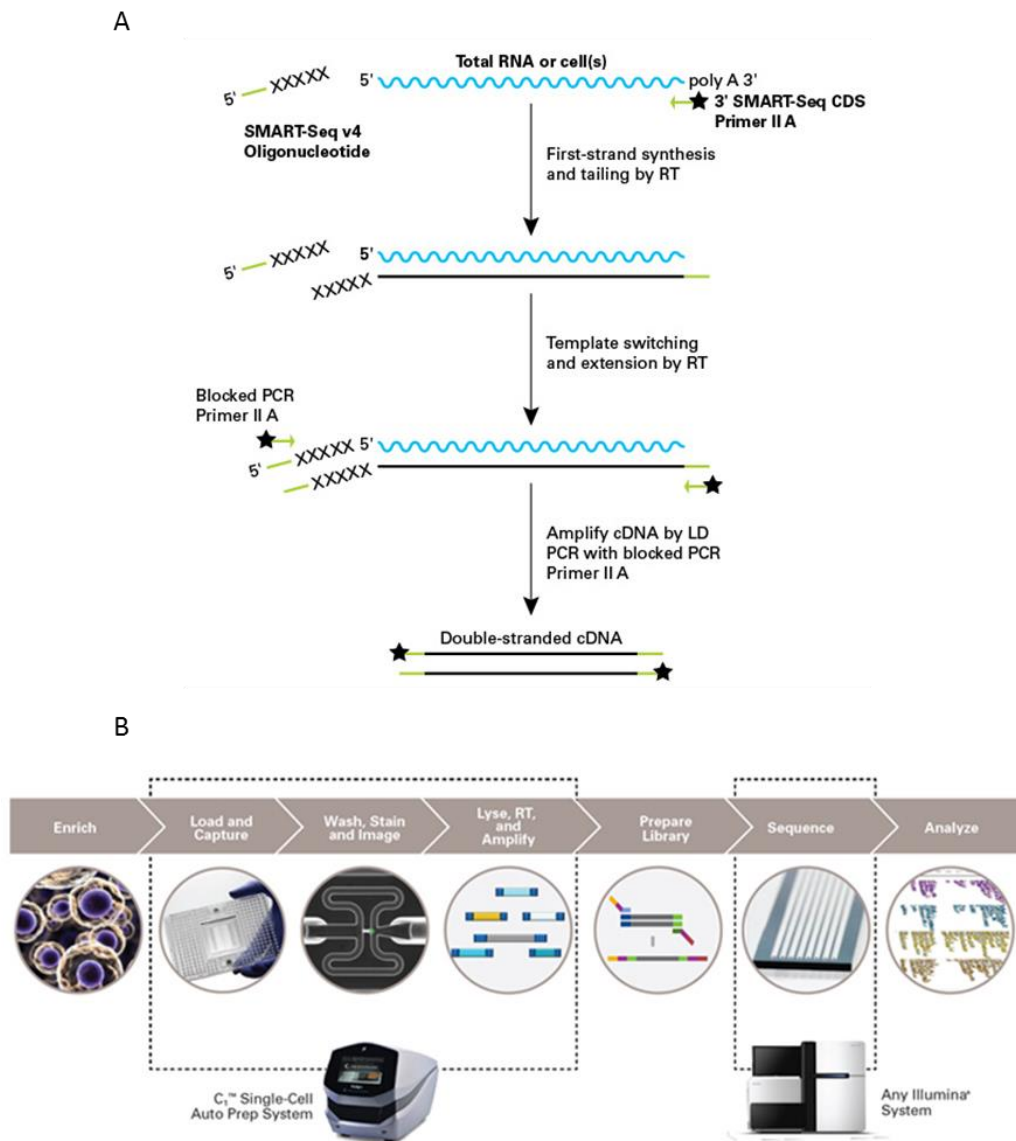
Figure 1-6 SMART method for single-cell RNA library preparation.
A An overview of SMART method implemented in SMARTer kit (Clontech). Figure source: http://www.clontech.com/US/Products/cDNA_Synthesis_and_Library_Construction/NGS_Learning_Resources/Technical_Notes/
B A workflow of C1 Single-cell Auto Prep System (Fluidigm) utilizing SMARTer chemistry in microfluidics. Figure source: http://www.well.ox.ac.uk/ogc/single-cell-resources

In 2015 E. Z. Macosko et al. introduced Drop-seq - a technology utilizing template switch mechnism in emulsion microdroplets [104]. Drop-seq is based on the separation of individual cells in aqueous droplets formed in an oil solution in a microfluidics system. Individual cells from a cell suspension are captured in nanoliter droplets along with uniquely barcoded microbeads (Figure 1-7). Each bead is covered with primers consisting

of 3 parts: a common sequence for further PCR amplification, bead-specific barcode for the encoding of individual cell and unique molecular identifier (UMI), which allows a digital count of unique transcripts and PCR bias correction.
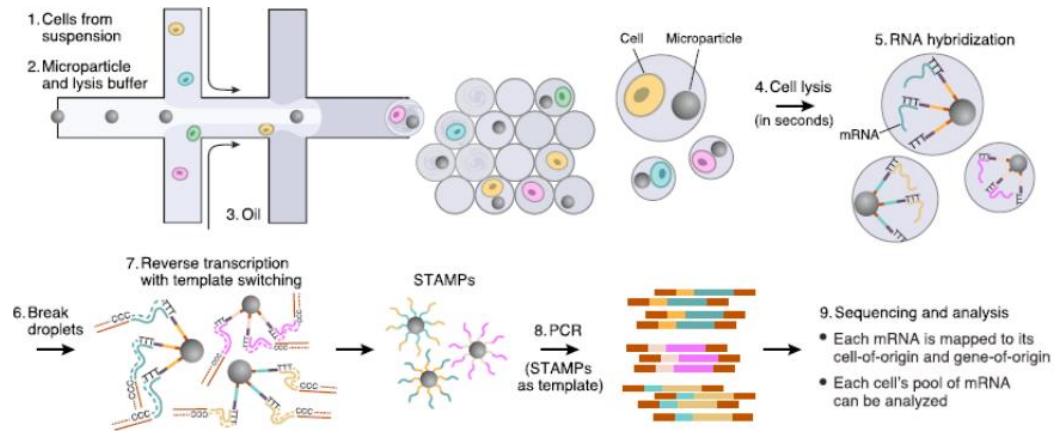
Figure 1-7 Drop-seq workflow for single-cell library preparation.
Figure source: Macosko, E.Z., et al., Highly Parallel Genome-wide Expression Profiling of Individual Cells Using Nanoliter Droplets. Cell, 2015. 161(5): p. 1202-14.

Using microfluidics, thousands of aqueous droplets are formed per minute with some of them containing individual cells and some containing microbeads. When a cell and microbead are captured in the same droplet, following cell lysis, the RNA from the cell is hybridized to the bead and combined with the other beads. The mRNA from thousands of cells is then reverse transcribed using the template switch mechanism and the cDNA is amplified and sequenced.

The ability to prepare thousands of single cell libraries in a short amount of time, as well as the simplicity of the protocol, distinguishes Drop-seq from alternative methods. However, unlike in the microfluidic chip systems, such as Fluidigm C1, the cell doublets captured in a single reaction can not be monitored microscopically. The estimated percentage of cell doublets accounts for up to 11 % depending on the cell concentration, however it potentially varies depending on cell type.

CEL-Seq (Cell Expression by Linear amplification) protocol and its updated version CEL-Seq2 were introduced by T. Hashimshony et al. in 2012 and 2016, respectively. This method utilizes in vitro transcription (IVT) instead of the template switch step applied in SMART-based approaches. CEL-Seq2 enables the incorporation of the UMI similarly to Drop-Seq to identify single transcripts. The cell-specific barcode in this method is introduced during the reverse transcription reaction, followed by the second strand synthesis. Single-cell cDNA is further pooled and amplified using linear IVT. This method

was originally developed for library preparation in tubes or microwell plates, but later, similarly to SMART seq, it was efficiently incorporated in Fluidigm C1 workflow. Both methods demonstrated considerable efficiency and reproducibility however require further optimisation.

1.3.2 Analytical approaches in single-cell RNA-sequencing

In many aspects, the experimental design and analysis of single-cell transcriptomes is similar to standard RNA sequencing. However, there are a number of unique features that distinguish single-cell RNA data and requires optimisation of the existing analytical approaches and the development of new tools. The key steps involve experimental design, the control of sequencing quality and filtering of cells, reads mapping, quantification and normalisation and methods for analysis of cell populations and underlying gene regulatory mechanisms.

An optimal design of a single-cell experiment requires, similar to conventional RNA-seq, the minimization of experimental differences between conditions, such as various technicians and the usage of different equipment and kits. Potential sources of systematic bias, including variance between robotic channels or well positions in microfluidic chips, must be extensively evaluated. For multiple conditions the cell subsets from different experimental conditions should be processed in the same batches and sequencing pools should contain cells from all conditions split in different sequencing flow cells or lanes, as it is recommended for conventional sequencing procedures [99, 101]. The addition of external RNA molecules, such as External RNA Controls Consortium (ERCC) RNA spike allows for better control of bias induced during library preparation, sequencing and data analysis.

The newest methods allow low-cost RNA library preparation from thousands of individual cells, but the costs of sequencing remain a limiting factor. Most single-cell studies published indicate that sequencing depth of ~1-1.5M reads per cell is sufficient to capture more than 95 % of the genes present in the library [105]. Nevertheless, the balance between cell number and depth of sequencing should be defined based on the specific research tasks and considering the used cell type and method of library preparation.

Quality control of sequencing reads before and after mapping can be performed using standard tools, such as FastQC, RSeQC and SAMTools [106-108]. Although estimation of the full list of standard parameters for all cells can be time consuming, some key features, such as total number of reads, percentage of mapped reads, duplication rate and base quality should be controlled. These parameters, together with microscopic data of captured cells if available, can be used to filter out inferior quality cells from further analysis.

Introduction

Read quantification and normalization represents one of the major steps in single-cell sequencing reads processing that influences analysis outcome. Standard approaches developed for bulk sequencing, such as HTSeq, RSEM and Cufflinks are widely used [109-111]. However, these methods assume low variance of the sequencing depth and total RNA input from different samples, which cannot be fully achieved in single-cell approaches due to large numbers of samples and biological differences between individual cells. Additionally, standard normalization approaches do not consider large fraction of zeros typical for single-cell data. Although these limitations may influence further analysis, many studies demonstrated that size factor normalization used in HTSeq or normalization to total number of sequencing reads and gene length producing TPM and FPKM values (RSEM, Cufflinks) can be efficiently applied [112-115].

The limitation of the standard normalization approaches is that they cannot account for the differences of RNA input. This problem can be solved by the usage of an external RNA spike, such as ERCC RNA spike, for read counts normalization [116, 117]. As the spike is added to the reaction at a known equal concentration, it allows normalization to the sequencing depth and estimation of absolute number of input RNA molecules.

The majority of single-cell studies aim to identify novel cell types or cell transcriptional states within a population. Supervised or unsupervised clustering methods are typically used to separate cells into subgroups. Widely used unsupervised methods, such as PCA, ICA, tSNE and hierarchical clustering can be applied to the whole transcriptome, highly expressed genes, differentially expressed genes between conditions or highly variable genes [99-101, 118]. Several unsupervised clustering methods have been developed specifically for the analysis of cell subpopulations. These include ZIFA, optimized for high fraction of zero values, SNN-cliq and Race-ID targeted at rare cell type identification [119-121]. Supervised clustering methods can be used when expression of certain marker genes as well as when temporal or spatial location of cells is predefined [99, 122, 123].

The estimation of cell-to-cell heterogeneity and the results of cell clustering can be affected by different superfluous biological factors and technical noise. Apart from potential systematic biases and batch effects, certain levels of steady technical variability are introduced during library preparation and sequencing due to efficiency differences of cell lysis, reverse transcription, PCR and other experimental procedures.

P. Brennecke et al. introduced a statistical model to assess the total variability for each expressed gene compared to the technical noise estimated based on ERCC spike expression [124]. In this study, the level of technical noise was estimated for the manual and microfluidics-based single-cell library preparation protocol utilizing SMART technology. Technical variability measured for each gene across all single cells

demonstrated dependency on the expression level (CV2 ~ 1/gene expression + const). The proposed statistical model allows for the identification of genes featuring biological variability significantly exceeding technical noise and is widely used to discriminate highly variable genes. An additional simple method proposed by B. Ding et al. allows technical noise reduction from gene expression values based on ERCC spike expression data [117].

Overall, the usage of ERCC spike and other external RNA molecules in single-cell protocols provides a wide range of additional information about the quality of single-cell data and can be used for expression normalization, as well as estimation and correction of technical noise. However, several limitations exist preventing its universal usage. Firstly, if not optimized, a substantial proportion of spike molecules may significantly increase sequencing costs. Secondly, ERCC spike molecules are shorter than average human mRNA molecules (ERCC spikes length is 500-2000nt, whereas the average human mRNA length is ~2100nt) and have a shorter polyA tail [99]. Additionally, it has been shown that ERCC spike demonstrate a lower level of PCR bias compared to endogenous transcripts [118].

Interfering biological factors such as cell cycling may also cause considerable problems in the analysis of cell populations masking other regulatory mechanisms. Buettner et al. developed a computational approach (scLVM) to account for hidden confounding factors in single-cell data and eliminate them from the analysis of cell heterogeneity [113]. This method demonstrated its efficiency on single-cell data of T cell differentiation where the elimination of cell cycle-related genes allowed to identify otherwise hidden biologically relevant cell subpopulations [113].

An additional intriguing application of single-cell data is an inference of gene co-expression networks. In such networks, genes represented as nodes are connected by edges representing co-expression values, such as Pearson or Spearman's correlations, their derivatives or other metrics. Weighted gene co-expression networks analysis (WGCNA) is an approach that was originally developed for conventional RNA sequencing and then proved its efficiency for single-cell data [125-127]. It allows comprehensive analysis of gene modules that potentially represent functional relations and coregulation, as well as analysis of gene connectivity, allowing identification of important hub genes. The derived networks can be used as a powerful resource for further functional experiments.

Overall, the field of bioinformatical methods for single-cell RNA-seq is rapidly expanding allowing better quality results to be obtained in a shorter time period. However, the proper experimental validation of the obtained results remains crucial to avoid potentially biased interpretation.

1.4 Aims of the thesis

Obesity is one of the major causes of the type 2 diabetes epidemic worldwide. Insulin resistance underlying the development of diabetes is largely related to a chronic low-grade inflammation characteristic in obese patients. Macrophages accumulating in the obese adipose tissue and other metabolic tissues represent one of the key cell types causing chronic inflammation through the activation of the TLR signaling pathway and other regulatory mechanisms.

Several distinct macrophage polarization states widely described in the literature demonstrate macrophage natural plasticity and heterogeneity. However, the full range of macrophage molecular phenotypes in different physiological conditions and underlying gene regulatory mechanisms are not fully described. In this study, we aimed to characterize metabolically stressed macrophages on a single-cell level to investigate the diversity of macrophage phenotypes and decipher key genes regulating macrophage polarization.

First, we aimed to establish a physiologically relevant cell model typical for adipose tissue macrophages in obesity. For the unbiased characterization of a cell response to mild metabolic stress it was particularly important to control for unwanted biological factors, such as different metabolic background of the analysed cells, cell cycle and others.

Second, we aimed to perform single-cell transcriptome sequencing and to develop and apply a comprehensive analytical workflow optimized for the characterization of mild changes in gene expression relevant for our cell model. This involves an extensive analysis of sequencing quality, unbiased cell filtering and the evaluation of technical noise introduced by the applied experimental procedures. Novel computational approaches should be evaluated and applied for the identification of cell subpopulations and analysis of the underlying gene regulatory networks.

Finally, the observed key regulatory mechanisms and pathways expressed in cell subpopulations require validation using additional experimental approaches including microscopy-based techniques devoid of bias by PCR amplification.

This study would provide a novel view on the macrophage biology in the context of obesity and type 2 diabetes. The derived gene regulatory networks and validated molecular mechanisms underlying cell state polarization would make a valuable resource for future studies.

2 Materials and Methods

2.1 Cell culture

2.1.1 THP-1 cells

We used THP-1 monocytes differentiated to macrophages using phorbol 12-myristate 13-acetate (PMA, Sigma-Aldrich) for further palmitate stimulation. The THP-1 cell line was established in 1980 from an acute monocytic leukemia patient and is widely used as a model for monocyte and macrophage regulation in vascular diseases, diabetes and atherosclerosis [128-131].

THP-1 cells (ATCC) were cultured in a RPMI 1640 growth medium (Sigma-Aldrich) supplemented with 10 % fetal bovine serum (FBS, Biochrom) at 37 °C under 5 % CO_2 in a CO_2 incubator. Subculturing was performed every 2-3 days to achieve the cell density of 2.5×10^5 cells/ml.

The total number of 1×10^6 cells in 4 ml volume were plated into each well of a 6-well plate (Corning) for differentiation. Then, a PMA concentration of 10nM was chosen, as it was previously shown to be optimal for weak stimulation of macrophages [132]. After approximately 24 hours of PMA-based differentiation, cells became adherent and acquired macrophage morphology. After 48 hours of PMA treatment cells were used for a subsequent 24 hours of treatment with palmitate or left unstimulated.

2.1.2 Primary human macrophages

First, peripheral blood mononuclear cells (PBMC) were isolated from human buffy coats, donated by 3 healthy individuals (provided by Deutsches Rotes Kreuz). Cells were isolated using density centrifugation with Ficoll-Paque (GE Healthcare) for 40 min at 400 g and washed with Dulbecco's Phosphate Buffered Saline (PBS, Sigma-Aldrich) supplemented with 0.5 % Bovine Serum Albumin (BSA, Sigma-Aldrich) and 2mM EDTA (Sigma-Aldrich).

Next, monocyte enrichment from PBMC was performed using the MACS Monocyte Isolation Kit II (Miltenyi Biotec) and MACS LS columns (Miltenyi Biotec).

Purified monocytes were subsequently seeded in 6-well cell culture plates (Corning) at a density of 5×10^5 cells/ml, in a total volume of 4 ml per well. Cells were differentiated for 7 days in RPMI 1640 growth medium (Sigma-Aldrich) supplemented with 10 % human AB serum (First Link UK LTD) and 1 % Penicillin/Streptomycin (Biochrom). After differentiation, primary human macrophages were used for palmitate stimulation or left unstimulated.

2.2 Macrophage stimulation with palmitate

A cell medium with 250 μM palmitate was prepared using the following previously validated procedure [133-135]:

1. Sodium palmitate solution (62.5 mM) was prepared by dissolving Sodium palmitate powder (Sigma-Aldrich) in 0.1M NaOH (Sigma-Aldrich) at 70°C for 30 %.
2. Fatty Acid Free BSA (Sigma-Aldrich) was dissolved in PBS (1:3 mass ratio) (Sigma-Aldrich) and pre-heated at 37 °C.
3. The palmitate solution was mixed with dissolved pre-warmed (37 °C) BSA at a 1:5 volume ratio and incubated at 37 °C for 30 min to form palmitate: BSA complex (molar ratio of palmitate: BSA was 7.5:1).
4. For THP-1 cells stimulation, the palmitate-BSA complex was diluted in a prewarmed (37°C) RPKM 1640 medium (Sigma-Aldrich) supplemented with 10 % fetal bovine serum (Biochrom) and 10 nM PMA (Sigma-Aldrich) to achieve a palmitate concentration of approximately 400-500 μM.
5. For primary human macrophages the palmitate-BSA complex was diluted in a prewarmed (37°C) RPKM 1640 medium (Sigma-Aldrich), supplemented with 10 % human AB serum (First Link UK LTD) and 1 % Penicillin/Streptomycin (Biochrom) to achieve the palmitate concentration of approximately 400-500 μM.
6. The medium with palmitate was filter sterilized using a 0.22 μm Stericup Filter Unit (Merck Millipore) and the Stericup Receiver Flask (Merck Millipore).
7. The palmitate concentration in medium was measured using a Free Fatty Acid Quantification Kit (BioVision) and adjusted to 250 μM.
8. In parallel to palmitate preparation, a control medium was made by combining 0.1 M NaOH (Sigma-Aldrich) with dissolved BSA instead of step 2, followed by a process identical to the palmitate medium preparation procedure, described in steps 3-7.
9. For palmitate stimulation of macrophages, THP-1 cells, previously differentiated in 6-well culture plates, were incubated with palmitate/ control medium for 24 hours.
10. After 24 hours of stimulation, cells were washed with 37 C warm PBS (Sigma-Aldrich), dissociated for 13 min using TrypLE (GIBCO) in CO_2 incubator at 37 °C and resuspended in PBS with 2 % BSA (Sigma-Aldrich).

2.3 RNA isolation and quality control

The RNeasy mini kit (Qiagen) was used according to standard manufacturer's protocol for total RNA isolation. We included 30 min on-column DNase digestion, using the RNase-Free

DNase Set (Qiagen). RNA quantification and quality control was performed using the Qubit 3.0 fluorometer (Thermo Fisher Scientific) with the Qubit RNA HS Assay Kit (Thermo Fisher Scientific) and Bioanalyzer 2100 (Agilent Technologies) with the RNA 6000 nano kit (Agilent Technologies) in addition to an agarose gel electrophoresis-based quality check.

2.4 Quantitative real-time PCR

To perform gene expression quantification, we used Sybr Green I-based quantitative real-time PCR. HPLC-purified custom primers were obtained from Sigma-Aldrich. Primer sequences (Table 2-9) were designed using Primer-BLAST software [136]. Additionally, we used a Toll-Like Receptor Signaling Pathway PCR Array (Qiagen) for gene expression analysis in bulk and single-cell validating experiments.

2.4.1 Bulk quantitative real-time PCR

Reverse transcription for bulk qPCR experiments was performed using the qScript cDNA SuperMix (Quantabio). Reverse transcription reaction was prepared in a total volume of 10 µl and incubated in a PCR thermal cycler using the program, summarized in Table 2-1:

Table 2-1 Reverse Transcription thermal cycler program

Temperature	Time
25 °C	5 min
42 °C	30 min
85 °C	5 min
4 °C	hold

We used PerfeCTa SYBR Green SuperMix (Quantabio) to prepare the qPCR reaction mix as follows (Table 2-2):

Table 2-2 Quantitative PCR reaction

Component	Final concentration	Volume (µl)
PerfeCTa SYBR Green SuperMix (2x)	1x	5
Primer pair	0.2 µM	2
cDNA	0.5 ng/µl	1-3
Nuclease-free H2O		variable
Total		10

Biological and technical triplicates were prepared for all qPCR experiments with custom designed primers. For bulk qPCR with a Toll-like Receptor Signaling Pathway PCR array we used biological duplicates.

Using the following program (Table 2-3), qPCR reactions were run in Light Cycler 480 384-well plates (Roche) on a LightCycler 480 II System (Roche):

Table 2-3 Quantitative PCR LightCycler 480 II program

Step	Temperature	Time
Pre-incubation	95 °C	3 min
Amplification - 45 cycles (60 cycles for single-cell qPCR)	95 °C	10 s
	60 °C	35 s
Melting curve analysis	95 °C	5 s
	65 °C	1 min
	up to 97 °C	0.03 °C /s

2.4.2 Single-cell quantitative real-time PCR

The following previously validated [137-139] procedure was carried out for single-cell gene expression analysis using quantitative real-time PCR:

2.4.2.1 Cell sorting into 96-well plates

1. 5 µl of nuclease-free water (Thermo Fischer Scientific) were pipetted into each of the A1-B12 wells in 96-well plates (Biozym) for single-cell sorting, and stored on ice.
2. After treatment, cells were harvested in ice-cold PBS (Sigma-Aldrich) with 2 % BSA (Biochrom) (approximate cell density was 1M cells/ml).
3. 5 µl of 7-Aminoactinomycin D (7-AAD) cell viability staining solution were added per 1 ml of cell suspension 10 min before cell sorting, and cell suspension was filtered through a 40 µm cell strainer.
4. Individual intact living cells were sorted into 96-well plates using the BD FACSAria II system with the following layout: wells A1-H11 contained a single cell per well (88 wells in total), wells A12 and B12 contained 40 cells per well, and the remaining 6 wells were left empty for "No Template Control" and "Interplate Calibrator Control".
5. Plates with cells were sealed with aluminum foil, snap frozen on dry ice and stored at -80°C.

2.4.2.2 Reverse transcription

Plates with cells were thawed at room temperature for 10 min and spun down. After thawing, all the pipetting steps were carried out on ice and centrifugation was done at +4°C. Both, THP-1 cells and primary human macrophages, were efficiently lysed after being frozen in nuclease-free water, and the reverse transcription reaction was prepared by adding the reverse transcription mix directly to cell lysates in the 96-well plate as follows:

1. qScript cDNA SuperMix (Quantabio) was diluted to 1:1 with nuclease-free water (Thermo Fischer Scientific) and stored on ice.
2. 1 µl of diluted qScript cDNA SuperMix was added to all wells with 1/40 cells, and the plate was sealed with aluminium foil (VWR). The plate was spun down, briefly vortexed and spun down again.
3. Reverse transcription reaction was performed in a thermal cycler as described in Table 2-1.
4. We used an "Interplate Calibrator" (IPC, TATAA Biocenter AB) to account for plate-to-plate bias. An IPC mix was prepared by combining 0.6 µl of IPC template, 1.5 µl of IPC primer and 2.9 µl of nuclease-free water (Thermo Fischer Scientific) (the total volume of 5 µl IPC mix required for a one qPCR reaction in 384-well plate).
5. When reverse transcription was finished, 35µl of nuclease-free water was added to wells with cDNA; 45 µl of IPC mix was added to the wells C12, D12, E12, and 45 µl of nuclease-free water was added to the wells F12, G12, H12 for No Template Control. The plate was briefly vortexed and centrifuged.
6. Diluted cDNA and controls material was transferred from 96- into Light Cycler 480 384-well plates (Roche) using the Biomek NX Liquid Handling Automation workstation (Beckman Coulter). 2x20 µl was aspirated from each well of the 96-well plate using AP96 P20 Tips (Beckman Coulter) and 5 µl was dispensed into 4 wells of each of the 384-well plates (A1 (96-well plate)->A1, A2, B1, B2 etc.).

2.4.2.3 Quantitative single-cell PCR

Directly after cDNA splitting, qPCR reaction mixes were prepared and dispensed into 384-well plates as follows:

1. PCR primer pairs were mixed with PerfeCTa SYBR Green SuperMix (Quantabio) to obtain a primer concentration of 0.4 µM. For IPC controls, nuclease-free water was added instead of primer solution.
2. 5 µl of PerfeCTa SYBR Green SuperMix with primers were dispensed into corresponding wells of the 384-well plates containing 5 µl of diluted cDNA. Plates with qPCR reaction mixes were sealed with aluminium foil (VWR), snap frozen and stored at -20°C until the qPCR run.

3. For the qPCR run, plates were thawed for 10min in room temperature, briefly centrifuged, ate which the aluminium foil was replaced with LightCycler 480 clear sealing foil (Roche).

4. For single-cell qPCR, we ran the same program as for bulk qPCR analysis (Table 2-2) using LightCycler 480 II System (Roche), but with a higher number (60) of amplification cycles.

2.4.3 Quantitative PCR data analysis

For the first part of qPCR analysis, we used LightCycler 480 software (Roche). To obtain the Quantification cycle (Cq value), we applied the "Abs Quant/2nd Derivative Max" method, implemented in the software. Melt Curve Analysis was performed by applying the "Tm calling" method. Melt curves were visually inspected to identify potential technical outliers and unspecific primer pairs with more than one melt peak, which were excluded from further analysis.

The next analytical steps with Cq values were executed using R statistical software. For bulk qPCR analysis, we applied the $2^{-\Delta\Delta Ct}$ method [140] (Equation 2-1,Equation 2-2,Equation 2-3) to quantify gene expression fold change relative to unstimulated control samples. For all bulk qPCR experiments, we used GAPDH as a reference gene.

Equation 2-1

$$\Delta Ct = Ct\ (Target\ gene) - Ct\ (GAPDH)$$

Equation 2-2

$$\Delta\Delta Ct = \Delta Ct\ (Stimulated\ sample) - \Delta Ct\ (Control\ sample)$$

Equation 2-3

$$R = 2^{-\Delta\Delta Ct}$$

Unpaired two-tailed Student's t-test was applied to Cq values in order to test for statistical significance of the observed differences. For multiple comparisons, we used one-way ANOVA followed by Dunnett's or Tukey's HSD test .

2.5 RNA sequencing

2.5.1 Cells preparation for bulk and single-cell RNA sequencing

For RNA sequencing, palmitate-stimulated and unstimulated cells were prepared in biological triplicates. After cell harvesting, ⅓ of the cell suspension volume from each triplicate was taken and combined for a further single-cell RNA-seq procedure. The remaining cells were processed in triplicates for validating bulk RNA-seq and qPCR experiments.

For the single-cell RNA-seq, we stained cells with a 7-Amino-Actinomycin D staining solution (BD Pharmingen) (5 µl per 1 ml cell suspension) and sorted approximately 60000 living cells into PBS (Sigma-Aldrich) with 2 % BSA, using BD FACSAria II (BD Biosciences). After sorting, the cell concentration was adjusted to the range of 66,000-333,000 cells/ml, and 5 µl of the cell suspension (~1000 cells) were loaded into the corresponding inlet of the Integrated Fluidic Circuit (IFC, Fluidigm) for medium cell size (10-17 µm).

2.5.2 Bulk RNA sequencing

RNA concentration measurement and quality control was carried out using the Qubit 3.0 Fluorometer (Thermo Fisher Scientific) and the Agilent 2100 Bioanalyzer (Agilent Technologies) with the RNA 6000 Nano Kit (Agilent Technologies). Sequencing libraries were prepared using the Illumina TruSeq RNA Library Prep Kit v2 (Illumina), and paired-end sequencing 2x100bp was performed using a HiSeq 2500 system(Illumina).

2.5.3 Single-cell RNA sequencing

We used the C1 Single-Cell Auto Prep System (Fluidigm) for cell lysis, reverse transcription and preamplification according to protocol provided by the manufcturer. One 96-cells Integrated Fluidic Circuit (IFC, Fluidigm) was used per treatment condition (palmitate-stimulated or unstimulated).

Reverse transcription and pre-amplification reactions were carried out using SMARTer chemistry. This method utilizes SMART-RACE technology, allowing full length processing of polyadenylated transcripts. Sequencing libraries were prepared using a Nextera XT transposase-based approach. 96 barcoded single-cell libraries were pooled and sequenced in parallel with the corresponding bulk controls. Information on single-cell library quality control is provided in Supplementary Figure 6.

In short, the workflow consisted of the following steps:

1. A medium size C1 IFC was primed and loaded with THP-1 macrophages.
2. Cells captured in chip micro wells were imaged using a light microscope.
3. Cells were lysed, RNA was reverse transcribed and cDNA was pre-amplified in the C1 system, using the SMARTer Ultra Low Input RNA Kit (Clontech) for Illumina Sequencing.
4. Pre-amplified cDNA products were harvested from IFC inlets; a cDNA concentration of C1 harvest amplicons was measured using the POLARstar Omega Plate Reader Spectrophotometer (BMG LABTECH) using a Quant-IT PicoGreen dsDNA Assay Kit (Thermo Fisher Scientific).
5. Additionally, selected C1 harvest products were run on an Agilent 2100 Bioanalyzer High Sensitivity DNA chip (Agilent Technologies).

6. All 96 harvest amplicons were used for Illumina library preparation with the Nextera XT DNA sample preparation kit (Illumina).
7. 96 single-cell sequencing libraries were pooled together, and the library pool was analysed on an Agilent Bioanalizer (Agilent Technologies), using the Agilent High Sensitivity DNA chip (Agilent Technologies). The average library size for an unstimulated sample was 719bp and 653bp for palmitate-stimulated. Obtained library concentrations were 325 and 270pg/µl correspondingly.
8. The single-cell library pools were sequenced using a Illumina HiSeq 2500 system to obtain 2x100bp paired-end reads.

2.6 Sequencing data analysis

2.6.1 Primary data analysis and quality control

BCL Illumina files were demultiplexed and converted to a FASTQ file format using bcl2fastq Conversion Software v1.8.4 (Illumina) with default parameters. For all bulk samples and selected single cells, the FASTQ file quality was controlled using FastQC software (Supplementary Figure 7) [106].

Adapter sequences and low-quality bases were cut from FASTQ files using Trimmomatic version 0.30 [141] with the following parameters:

- Remove adapter sequences (default settings)
- Remove leading/trailing low quality bases (below quality 3)
- Scan reads with a 4-base wide window, and cut when the average quality per base drops below 15

Trimmed FASTQ files were mapped to the human reference genome hg19 (Genecode 19 annotation [142]) using a STAR v. 2.4.0 RNA-seq aligner [143] with default parameters.

Reads quantification and FPKM normalization was performed using an HTseq-count script from the HTseq-0.6.1 python package [109] or the Cufflinks (v. 2.2.1) software [111] with default parameters.

2.6.2 Secondary data analysis of bulk RNA sequencing

Differential Expression (DE) analysis of bulk RNA-seq was executed using the DESeq2 package in R [144] according to a standard workflow described in the manual. We considered genes to be differentially expressed when the absolute expression fold change was higher than 2, and P-Value was less than 0.001.

We performed gene functional annotation enrichment analysis of detected DE genes using DAVID Bioinformatics Resources [145, 146].

2.6.3 Independent Component Analysis of single-cell RNA sequencing data

Single cells were filtered based on IFC capture sites image analysis. 74 palmitate-stimulated and 72 unstimulated cells were used for further analysis. For the Independent Component Analysis (ICA) of single cells, we used DE genes, defined for bulk RNA samples and expressed with a minimum mean expression level of 5 read counts in single-cell data for palmitate treatment. We also excluded genes that did not belong to defined gene co-expression clusters in WGCNA analysis. Altogether, 266 genes were selected. For ICA analysis, single-cell gene expression values were log-transformed (ln(read count+1)). ICA analysis was performed by using the *sc_DimensionalityReductionObj* function from the "sincell" statistical package in R [147]. Cell subpopulatons were defined based on density distribution of cells in 2-dimensional IC-space.

2.6.4 Weighted gene co-expression network analysis of single-cell RNA sequencing data

We constructed and analysed gene co-expression networks based on single-cell gene expression data using a WGCNA package in R [125, 148, 149]. The following workflow was implemented:

1. Optimal "soft threshold" power (β) was defined for further network construction using the *pickSoftThreshold* function, based on the scale free topology property of the gene network.
2. An adjacency matrix was calculated based on single-cell expression matrix for palmitate-stimulated cells using the *adjacency* function. Pearson's correlation was used to calculate gene co-expression similarity. We used the "signed" type of network to preserve information about the sign of Pearson's correlation coefficient.
3. A Topological Overlap Matrix (TOM) was calculated based on the adjacency matrix using the *TOMsimilarity* function. (TOM dissmilarity=1-*TOMsimilarity*).
4. Hierarchical clustering was performed based on TOM dissimilarity with the cluster method "average" using the *flashClust* function.
5. Gene modules were defined from the dendrogram, generated in the previous step, using the Dynamic Tree Cut method.
6. Module membership and intramodular connectivity were calculated for all genes to identify "hub" genes in different gene co-expression modules.

2.6.5 Variance estimation in single-cell RNA sequencing

To estimate variability levels between single cells in a population, we used a previously described approach by A.A Kolodziejczyk et al. [114]. This method aims to compute a variance metric that is not dependent on the mean expression of a particular gene. First,

we plotted mean expression values versus squared coefficients of variation (CV^2) for each gene. Then, we used the local polynomial regression fitting function (*loess* function from stats package in R) with a formula y~1/x. Finally, for each gene we calculated a distance between the squared CV and local regression fit. This distance we used as a variance metric to compare the variability between individual cells of genes and gene modules.

2.7 Immunofluorescence double staining

Immunofluorescence double-staining protocols allow for the simultaneous detection of 2 different antigens in the same sample using primary antibodies derived from different species. For our experiments, we used combinations of mouse and rabbit primary antibodies with the corresponding secondary antibodies conjugated with Alexa 488 and Alexa 594 fluorescent dyes.

2.7.1 Specimen preparation

THP-1 cells or primary monocytes were seeded on Poly-L-Lysin (Sigma-Aldrich) coated glass slides in 24-well cell culturing plates (Corning). Cells were further differentiated to macrophages and stimulated with palmitate as described in sections 2.1 and 2.2.

After treatment cells were fixed and permeabilized using the Transcription Factor Buffer Set (BD Pharmingen) and blocked with normal goat serum. Immunofluorescent double-labelling for different antibodies pairs was prepared as follows:

1. The primary antibodies mix (200 µl) was added into each well, and plates were incubated at +4°C overnight. The primary antibodies mix (per well) was prepared by combining 200 µl of the Perm/Wash buffer and a pair of primary antibodies (mouse and rabbit) to obtain a working concentration of 1.5 µg/ml for each antibody.
2. After incubation with primary antibodies, glass slides with attached cells were washed twice with 200 µl of the Perm/Wash buffer and 100 µl of the secondary antibodies mix was added to each well, followed by a 1 hour incubation in the dark, at +4 °C. The secondary antibodies mix was prepared by combining (per well) 100µl of the Perm/Wash buffer with a pair of Goat anti-Mouse and Goat anti Rabbit fluorescently labelled secondary antibodies to obtain a final concentration of 4mg/ml of each antibody.
3. The glass slides with the cells were washed twice with 200 µl of ice-cold Perm/Wash buffer and mounted on microscopic slides using ProLong Gold Antifade Reagent with DAPI (Thermo Fisher Scientific).
4. Specimens were dried in room temperature overnight and stored at +4 °C in the dark for up to 1 week, after which the imaging was performed.

The full list of primary and secondary antibodies used for immunofluorescence analysis is provided in Table 2-10 and Table 2-11. In parallel the specimens treated with only secondary antibodies were prepared and analyzed to account for unspecific binding.

2.7.2 Image acquisition and analysis

Immunofluorescence images were obtained using AxioObserver Z1 Inverted Microscope (Zeiss). For each specimen, we acquired a 100 tiled-image (10x10) using Z-stacking (4 Z-layers) and 3x3 binning. We used 3 channels corresponding to Alexa 488 and Alexa 594 fluorescent dyes for antibodies detection and DAPI for nuclei staining. Detailed information on microscopy settings and image acquisition parameters is provided in Table 2-4:

Table 2-4 Microscopy settings and acquisition parameters for Immunofluorescence

Image dimensions	
Channels	3
Scaling per Pixel	0.330 µm x 0.330 µm
Image Size (Pixel)	666 x 545
Image Size (Scaled)	219.88 µm x 179.94 µm
Bit Depth	14 Bit
Acquisition information	
Objective	Plan-Apochromat 40x/1.4 Oil DIC (UV) VIS-IR M27

	Channel 1	Channel 2	Channel 3
Reflector	50 Cy 5	38 HE Green Fluorescent Protein	49 DAPI
Beam Splitter	660	495	395
Filter Ex. Wavelength	625-655	450-490	335-383
Filter Em. Wavelength	665-715	500-550	420-470
Contrast Method	Fluorescence	Fluorescence	Fluorescence
Light Source	HXP120 V	HXP120 V	HXP120 V
Channel Name	Alexa Fluor 594	Alexa Fluor 488	DAPI
Excitation Wavelength	280	493	353
Emission Wavelength	618	517	465
Imaging Device	Axiocam 506	Axiocam 506	Axiocam 506

Image analysis was performed in 2 major steps:

First, we used the following tools from ZEN 2 blue edition software for primary image processing:

1. Extended depth focus was applied to generate a 1-layered optimally focused image with 100 tiles from 4 Z-layers.
2. Stitching with fuse tiles and shading correction was used to obtain a single image from 100 tiles, and to correct background fluorescence between different tiles.
3. Manual black/ white background correction was finally used for each combination of antibodies to subtract background fluorescence.
4. Pre-processed images were exported in TIFF file format for further analysis.

The following analytical steps were performed using the EBImage package in R [150]. Our workflow generally followed the recommended procedure for cell and nuclei segmentation and signal quantification (provided with the package at Bioconductor). We used *thresh*, *fillHull* and *bwlabel* functions for nuclei segmentation. As a next step, we performed Voronoi-based cell segmentation, using the *propagate* function and taking previously defined nuclei as seeds. Signal intensity for each antibody or DAPI nuclei staining was quantified using the *computeFeatures* function.

Images of IF specimens were acquired using an inverted microscope with 3 active channels corresponding to two antibodies and nuclei stain DAPI. We acquired 4 Z-stacks for all images and applied a focus stacking method, integrated in ZEN 2 software, to obtain a single Extended Depth of Focus image with optimal focus for all cells varying in the Z-coordinate (Supplementary Figure 15).

The obtained images had a full size of 2.5 × 2.0 mm and consisted of 100 tiles (10 × 10). Tiles were stitched, and shading between tiles was automatically corrected using ZEN 2 software (Supplementary Figure 16, Supplementary Figure 17).

Cell segmentation and signal quantification was performed using the EBImage package in R (Supplementary Figure 18).

In our first step of EBImage-based analysis, we optimized the parameters of nuclei detection and watershed transformation-based separation of closely located nuclei.

Secondly, cell detection was performed based on a raw combined signal from all 3 channels. Cells overlapping with image borders were subsequently removed, and cell segmentation was performed, using previously identified nuclei as the seed. Finally, the total fluorescent signal for both antibodies was quantified for each cell.

2.8 Reagents and consumables

Table 2-5 Kits

Kit	Cat.number	Manufacturer
Agencourt AMPure XP	A63880	Beckman Coulter
Agilent High Sensitivity DNA Kit	5067-4626	Agilent Technologies
Agilent RNA 6000 Nano kit	5067-1511	Agilent Technologies
C1 Single-Cell Auto Prep Array for mRNA Seq (10-17um)	100-5760	Fluidigm
C1 Single-Cell Auto Prep Reagent Kit for mRNA Seq	100-6201	Fluidigm
ERCC RNA Spike-In Mix	4456740	Thermo Fisher Scientific
Free Fatty Acid Quantification Kit	K612-100	BioVision
Nextera XT DNA Sample Preparation Index Kit	FC-131-1002	Illumina
Nextera XT DNA Sample Preparation Kit	FC-131-1096	Illumina
PerfeCTa SYBR Green SuperMix	95054	Quantabio
qScript cDNA SuperMix	95048	Quantabio
Quant-iT™ PicoGreen® dsDNA Assay Kit	P11496	Thermo Fisher Scientific
Qubit RNA BR Assay Kit	Q10210	Thermo Fisher Scientific
Qubit RNA HS assay Kit	Q32852	Thermo Fisher Scientific
RNase-Free DNase Set	79254	Qiagen
RNeasy mini kit	74104	Qiagen
RT² Profiler PCR Array Human Toll-Like Receptor Signalng Pathway	PAHS-018ZG-1	Qiagen
SMARTer Ultra Low Input RNA Kit for Illumina Sequencing	634828	Clontech
TATAA Interplate Calibrator	IPC250S	TATAA Biocenter AB

TruSeq PE Cluster Kit v3 - cBot - HS	PE-401-3001	Illumina
TruSeq RNA Library Prep Kit v2	RS-122-2001	Illumina
TruSeq SBS Kit v3 - HS (200-cycles)	FC-401-3001	Illumina

Table 2-6 Reagents

Reagent/Chemical	Cat.number	Manufacturer
2-Mercaptoethanol	805740	Merck Millipore
2-Propanol EMSURE	109634	Merck Millipore
7-Amino-Actinomycin D (7-AAD) staining solution	559925	BD Pharmingen
Ethanol EMSURE	100983	Merck Millipore
Ethylenediaminetetraacetic acid (EDTA)	E6635	Sigma-Aldrich
Nuclease-free water	AM9937	Thermo Fisher Scientific
Poly-L-Lysine Hydrobromide	P7890	Sigma-Aldrich
ProLong Gold Antifade Reagent with DAPI	P36931	Thermo Fisher Scientific
Sodium hydroxide solution (NaOH)	72068	Sigma-Aldrich
Sodium palmitate	P9767	Sigma-Aldrich

Table 2-7 Cell culture

Product	Cat.number	Manufacturer
Bovine Serum Albumin (BSA)	A7030	Sigma-Aldrich
C-Chip Neubauer	PK36.1	Carl Roth
Dulbecco's Phosphate Buffered Saline (PBS)	D8537	Sigma-Aldrich
Fetal Bovine Serum (FBS) Superior	S 0615	Biochrom
Ficoll-Paque	E6635	GE Healthcare
Human AB serum		First Link UK LTD
MACS LS columns	130-042-401	Miltenyi Biotec
MACS Monocyte Isolation Kit II, human	130-091-153	Miltenyi Biotec
Penicillin/ Streptomycin, liquid	A 2213	Biochrom

Product	Cat.number	Manufacturer
Phorbol 12-myristate 13-acetate (PMA)	P8139	Sigma-Aldrich
RPMI 1640 medium with 2.0 g/l NaHCO$_3$,with stable glutamine	FG 1215	Biochrom
THP-1 cell line	TIB-202	ATCC
Transcription Factor Buffer Set	562725	BD Pharmingen
TrypLE Express	12604021	GIBCO

Table 2-8 Consumables

Product	Cat. Number	Manufacturer
150 cm² flask	90151	TPP
25 cm² flask	90026	TPP
75 cm² flask	90076	TPP
Aluminium Sealing Foil for 96-well plates	391-1282	VWR
AP96 Tips, P20 Sterile Barrier	717256	Beckman Coulter
Costar 12-well Cell Culture Plate	3737	Corning
Costar 24-well Cell Culture Plate	3738	Corning
Costar 6-well Cell Culture Plate	3736	Corning
Hard-Shell 96 Well Plate	621601	Biozym
LightCycler 480 Multiwell Plate 384, white	04729749001	Roche
LightCycler® 480 Sealing Foil	4729757001	Roche
Stericup Filter Unit, 0.22 μm	SCGPT02RE	Merck Millipore
Stericup Receiver Flask, 500 ml, radio-sterilized	SC00B05RE	Merck Millipore

2.9 Quantitative real-time PCR primers and antibodies

Table 2-9 Quantitative PCR primer sequences

Gene symbol	Gene full name	Forward Primer	Reverse Primer
ACTB	Beta Cytoskeletal Actin	GAGCACAGAGCCTC GCCTTT	ATCATCATCCATGGT GAGCTGG
ATF3	Activating Transcription Factor 3	TGGATGGGATCAGA TGGGAAGA	GCATCATTTTGATTTT GGGGCA
CRELD2	Cysteine-Rich With EGF-Like Domains 2	CAGAGGCTGAAGCC ACAGAA	GTCCGGCACATTACA GGTCT
DDIT3	DNA-Damage-Inducible Transcript 3	GGAACCTGAGGAGA GAGTGTTC	AGCTGGTCTGATGCC TGTTT
DPP4	Dipeptidyl-Peptidase 4	ACGATGAAGACACC GTGGAA	TTGTTCAGCAGAACC ACGGG
GAPDH	Glyceraldehyde-3-Phosphate Dehydrogenas	CTCCTCCTGTTCGAC AGTCA	CGACCAAATCCGTTG ACTCC
IL1B	Interleukin 1, beta	GGACAGGATATGGA GCAACAAG	AACACGCAGGACAG GTACAG
IL8	Interleukin 8	CTGATTTCTGCAGCT CTGTG	GGGTGGAAAGGTTT GGAGTATG
MYD88	Myeloid Differentiation Primary Response 88	CTCTCTCCAGGTGCC CATCA	GGTTGGTGTAGTCG CAGACA
NFkB	Nuclear factor kappa-light-chain-enhancer of activated B cells	TGAGTCCTGCTCCTT CCA	GCTTCGGTGTAGCCC ATT
NFkBIA	Nuclear factor of kappa light polypeptide gene enhancer in B-cells inhibitor, alpha	CTTCGAGTGACTGAC CCCAG	TCACCCCACATCACT GAACG
TICAM 1	Toll-Like Receptor Adaptor Molecule 1	GTCCGGGAGCCCTTC ATTTA	TCCAGTTCTGACCAC CCTGA
TNF	Tumor Necrosis Factor	AGGGACCTCTCTCTA ATCAGC	CTCAGCTTGAGGGTT TGCTAC

Table 2-10 Primary antibodies

Antibody	Cat. Number	Host	Manufacturer
ATF3 (6G11)	SAB1412010-100UG	Mouse	Sigma-Aldrich
ATF3 (C-19)	sc-188	Rabbit	Santa Cruz Biotechnology
IL1B	mAb 12703	Rabbit	Cell Signaling Technology
IL1B (11E5)	sc-52012	Mouse	Santa Cruz Biotechnology
PPARG (52B83)	sc-7196	Rabbit	Santa Cruz Biotechnology
PPARG (8D1H8H4)	sc-81152	Mouse	Santa Cruz Biotechnology

Table 2-11 Secondary antibodies

Antibody	Conjugate	Cat. Number	Manufacturer
Goat anti-Mouse IgG (H+L)	Alexa Fluor 488	A28175	Thermo Fisher Scientific
Novex Goat anti-Mouse IgG (H+L)	Alexa Fluor 594	A11032	Thermo Fisher Scientific
Novex Goat anti-Rabbit IgG (H+L)	Alexa Fluor 488	A11034	Thermo Fisher Scientific
Novex Goat anti-Rabbit IgG (H+L)	Alexa Fluor 594	A11012	Thermo Fisher Scientific

2.10 Laboratory equipment

Table 2-12 Equipment

Instrument	Manufacturer
AxioObserver Z1 Inverted Microscope	Zeiss
BD FACSAria II	BD Biosciences
Bioanalyzer 2100	Agilent Technologies
Biomek NX Liquid Handling Automation workstation	Beckman Coulter
C1 Single-Cell Auto Prep System	Fluidigm
HiSeq 2500	Illumina
LightCycler 480 Instrument II	Roche
POLARstar Omega Plate Reader Spectrophotometer	BMG LABTECH
Qubit 3.0 Fluorometer	Thermo Fisher Scientific

2.11 Software

Table 2-13 Software

Software	Provider
bcl2fastq Conversion Software v1.8.4	Illumina
DAVID Bioinformatics Resources	National Institute of Allergy and Infectious Diseases (NIAID), NIH; https://david.ncifcrf.gov/home.jsp
DESeq2	Michael Love, Simon Anders, Wolfgang Huber; https://bioconductor.org/packages/release/bioc/html/DESeq2.html
ZEN 2 blue edition	Zeiss
EBImage	Andrzej Oleś, Gregoire Pau, Mike Smith, Oleg Sklyar, Wolfgang Huber, with contributions from Joseph Barry and Philip Marais; https://bioconductor.org/packages/release/bioc/html/EBImage.html
HTseq-0.6.1	Simon Anders; EMBL Heidelberg, Genome Biology Unit; http://www-huber.embl.de/HTSeq/doc/overview.html
Primer-BLAST	Ye J, Coulouris G, Zaretskaya I, Cutcutache I, Rozen S, Madden T , NCBI; https://www.ncbi.nlm.nih.gov/tools/primer-blast/
sincell	Miguel Julia, Amalio Telenti, Antonio Rausell; https://bioconductor.org/packages/release/bioc/html/sincell.html
STAR v. 2.4.0 RNA-seq aligner	Alexander Dobin; https://github.com/alexdobin/STAR
STRING database	Szklarczyk D, Franceschini A, Wyder S, Forslund K, Heller D, Huerta-Cepas J, Simonovic M, Roth A, Santos A, Tsafou KP, Kuhn M, Bork P, Jensen LJ, von Mering C.; http://string-db.org/

Trimmomatic version 0.30	AG Usadel; RWTH Aachen University, Institute for Biology I
UCSC Genome Browser	UC Santa Cruz, UCSC Genome Bioinformatics Group
WGCNA	Peter Langfelder, Steve Horvath; Dept. of Human Genetics, UC Los Angeles, Dept. of Biostatistics, UC Los Angeles; https://labs.genetics.ucla.edu/horvath/CoexpressionNetwork/Rpackages/WGCNA/

3 Results

3.1 Establishing an *in vitro* model for metabolic disease

3.1.1 Palmitate-stimulated THP-1 macrophages model

An elevated level of plasma free fatty acids (FFAs) is a characteristic feature in obese and atherosclerotic patients [151, 152]. Plasma FFAs were shown to play a critical role in the stimulation of immune cells underlying chronic inflammation [46, 59, 153]. Increased dietary consumption of saturated FFAs is associated with insulin resistance and type 2 diabetes [47, 154]. Common saturated fatty acids consumed in food involve stearic, palmitic, oleic, linoleic and other acids [155, 156].

In our study, we applied elevated concentrations of palmitate to *in vitro* cultured THP-1 macrophages. Palmitate is one of the most abundant fatty acids in human blood plasma and has been widely studied in obesity and type 2 diabetes research [157-159]. For most of our experiments, we used 250 µM palmitate, which corresponds to physiological ranges [133, 160-162].

The application of isogenic THP-1 cell line enabled us to eliminate potential hidden biases that can introduced by a metabolic status of a primary cell donor or other effects. Another important feature of THP-1 macrophages is that they are cell cycle arrested, which allows to maximize the level of homogeneity in the system before the metabolic stress is applied [163].
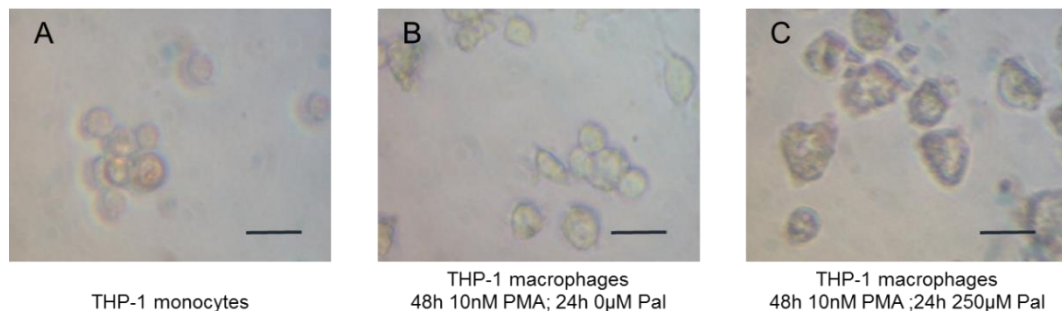
Figure 3-1 Light microscopy picture of cultured THP-1 cells (scale – 25 µM).
A THP-1 monocytes.
B THP1 macrophages after 48 hours of 10 nM PMA stimulation.
C THP-1 macrophages after PMA-induced differentiation and 24 hours of 250 µM palmitate treatment.

During PMA stimulated differentiation, THP-1 monocytes adhered to the culture plate and acquired flat shape (Figure 3-1 A, B). After differentiation, THP-1 macrophages were activated with palmitate and acquired a "foam cell" phenotype (Figure 3-1 C).

We measured the cytotoxicity level for THP-1 macrophages treated with different palmitate concentrations in the range of 0-625 μM (Supplementary Figure 1). The subsequently applied 250 μM concentration had a relatively low cytotoxic effect (15 %).

3.1.2 Gene expression analysis of inflammatory markers

To observe the effects of palmitate stimulation, we firstly analysed the expression of important marker genes, which are regulated by toll-like receptor signaling pathway, using quantitative real-time PCR (Figure 3-2).
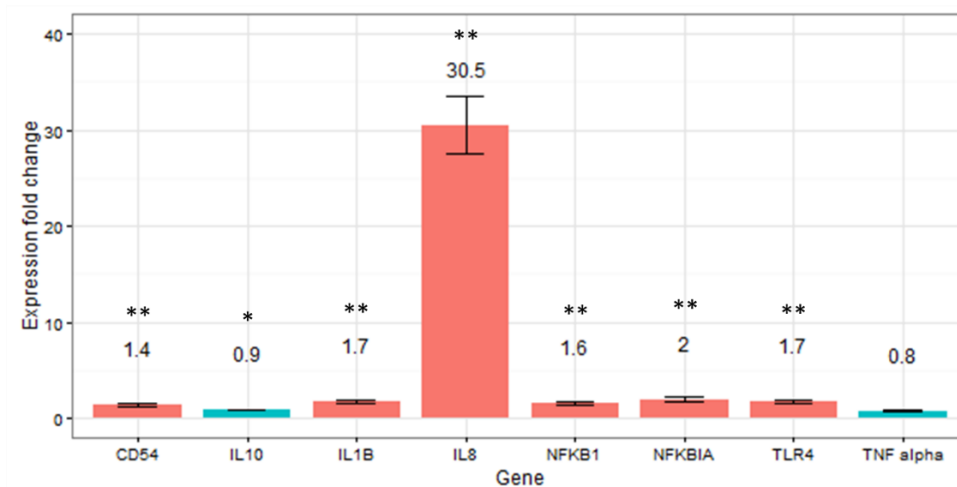
Figure 3-2 Quantitative real-time PCR analysis of marker genes, involved in toll-like receptor 4 signaling.
Expression fold change was measured between palmitate-stimulated (250 μM, 24 hours) and unstimulated THP-1 macrophages. Results are expressed as mean expression fold change ± SEM. * P-Value < 0.05; ** P-Value < 0.01; *** P-Value < 0.001

Interleukin 1 Beta (IL1β), Interleukin 8 (IL8), Tumour Necrosis Factor-Alpha (TNFα) as well as Cluster of Differentiation 54 (CD54/ ICAM1) and Nuclear Factor Kappa B Subunit 1 (NFKB1) genes are involved in innate immune response upon toll-like receptor 4 (TLR4) stimulation and promote inflammation [164, 165]. These genes are characteristic for M1 polarized macrophages [23, 24]. Interleukin 10 (IL10) and NFκB Inhibitor Alpha, on the contrary, are involved in immune modulation. IL10 plays a major role in enhancing the M2 macrophage phenotype [166, 167].

For most of the tested pro-inflammatory genes, we observed a statistically significant upregulation of expression. Although, for all these genes except IL8, the expression fold change did not exceed 2. This corresponds to low-grade inflammatory processes described in macrophage stress response to FFAs.

3.2 Technical noise estimation in single-cell RNA sequencing

To evaluate the level of technical variability between different wells of the C1 Integrated Fluidic Circuits (IFC), we performed an additional experiment using bulk RNA from the unstimulated THP-1 macrophages and ERCC spikes. The External RNA Control Consortium (ERCC) spike represents a set of 92 synthetic transcripts with the length of 250-2000nt spanning 106-fold concentration range to mimic eukaryotic mRNA [196]. The addition of the ERCC mix, with defined concentrations for each synthetic transcript to wells containing single cells, allows for the estimation of technical bias introduced by sample preparation workflow. This strategy has been routinely used in the C1 Fluidigm-based protocol, as well as in other methods of single-cell RNA-seq [112, 197].

In our experiment, the mixture of ERCC spikes and bulk RNA from the unstimulated cells was added into a cell-loading inlet of a medium size C1 IFC. We repeated the procedure that was used for single-cell library preparation by utilizing technical duplicates with a bulk RNA/ERCC mix. The obtained libraries were sequenced using the Illumina paired-end 2x75bp workflow, and produced 680M sequencing reads for both IFCs. Using this approach, we aimed to reveal potential systematic biases between different IFCs, estimate the differences in well sizes and to understand how representative the ERCC spike is for the total single-cell transcriptome analysed by the C1-based approach.

After sequencing and read mapping, we obtained in total 315 and 365 million reads for two IFCs. 97 % of the reads were mapped to transcriptome and 2 % were mapped to ERCC spike sequences for both IFCs. The correspondence of expression levels between IFCs for detected genes and spike molecules is shown in Figure 3-3. Technical replicates exhibited a very high correlation for the whole expression range: Pearson's correlation coefficient for mRNA was 0.992, and for ERCC spike 0.958.

To estimate potential systematic biases in particular wells and sections of the IFC, we looked at the read numbers produced from all 96 wells in both replicates and compared these to the previously obtained results for the single-cell mRNA-seq of unstimulated macrophages (Supplementary Figure 2). Read numbers were normalized to the mean value and visualized according to the 96-well plate layout, obtained from the C1 RNA-seq protocol.

We did not observe any patterns for over- or under-sequenced wells. We also looked at density distribution of the normalized read numbers across the 96-wells, and we observed that in bulkRNA/ERCC the distribution was more narrow when compared to single-cell RNA sequencing.
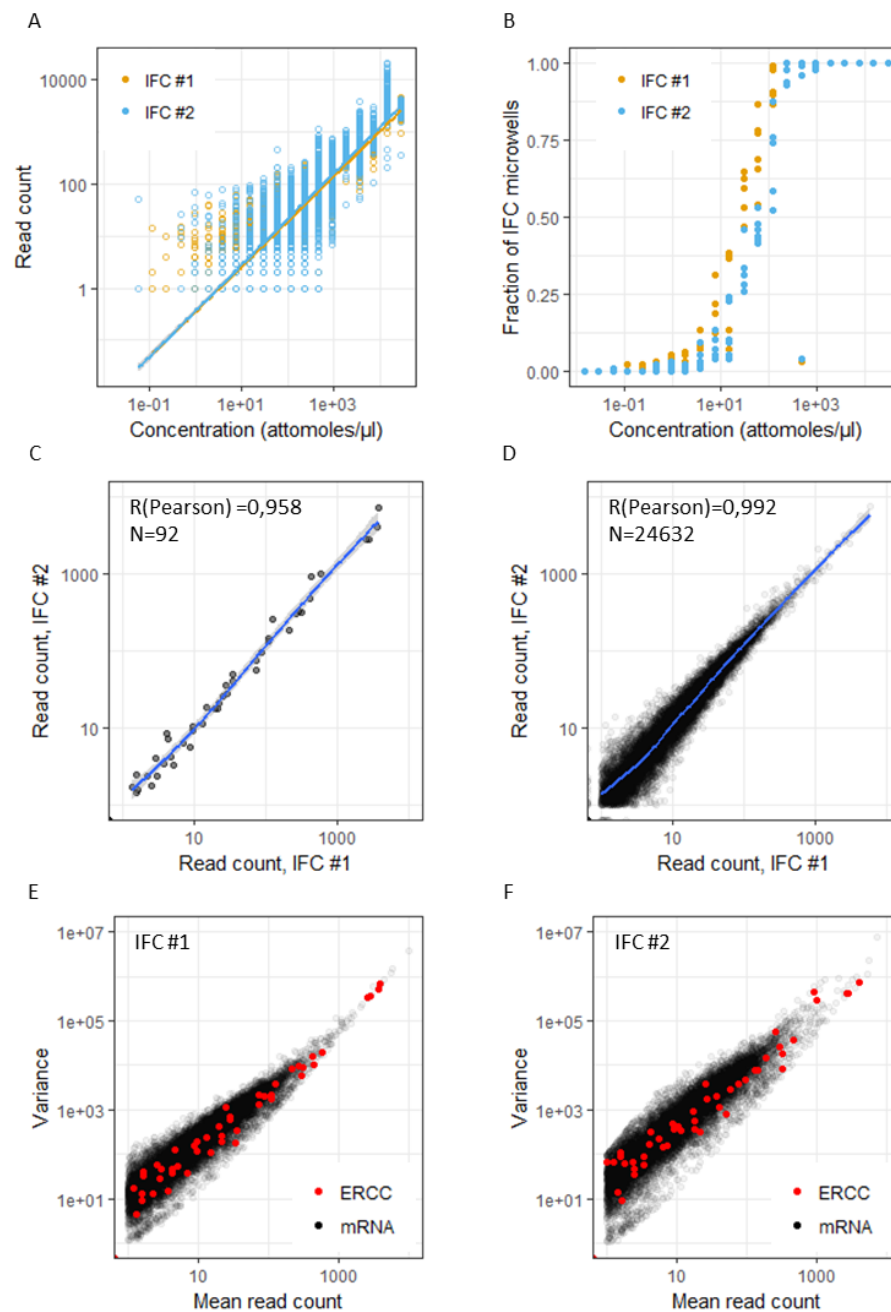
Figure 3-3 Estimation of technical noise introduced by Fluidigm C1-based single-cell RNA sequencing workflow.
A-C Analysis of ERCC spike. **A, B** Correspondence between known input concentration of each spike and observed expression (A) and fraction of wells (out of 96) where the molecule was detected (at least 1 read count) (B). **C** Correlation between two microfluidic IFCs.
D Correlation between two IFCs based on bulk mRNA analysis.
E-F Variance estimation for ERCC spike and bulk mRNA genes for two IFCs.

This difference can be explained by the biological variability between different cells (including cell size and total RNA content). The technical reason for this lies in the efficiency of cell lysis, which can vary between wells, although for the bulk analysis of THP-1 macrophages, we observed a very high efficiency of cell lysis when using simple RNAse free water as a buffer.

We also estimated the dependency of expression variance across 96 IFC wells on a mean expression level for all detected transcripts (Figure 3-3). Linear correlation was observed for both mRNA and ERCC spike molecules. Variance, observed in ERCC spikes, was similar to the variance observed in bulk RNA. A generalized linear regression for ERCC and bulk transcriptome showed a perfect overlap, in particular for transcripts with an expression level higher than 100 read counts (Supplementary Figure 5).

Next, we compared the gene expression variance observed in single-cell transcriptome analysis of unstimulated macrophages with the variance quantified for bulk RNA and ERCC spikes (Figure 3-4). We observed, that for low-expressed transcripts with a read count of up to 10, quantified technical variance was comparable to the total variance of single-cell data. For the expression range from 10 to 100, a significant fraction of genes had a total variance higher than technical. The genes with an expression higher than 100 read counts could be clearly separated from the estimated technical noise. Thus, we have shown that the single-cell protocol used in our experiments allows for robust quantification of biological variability in highly expressed genes.
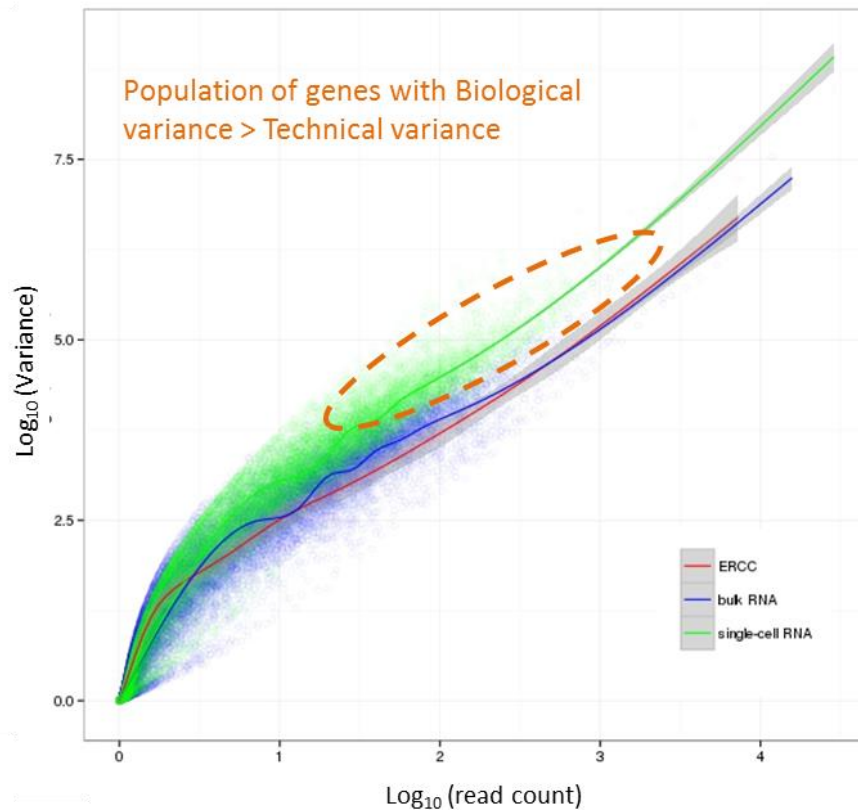
Figure 3-4 Technical and biological variance estimation across IFC 96 wells.
Biological variance is computed based on single-cell RNA data from unstimulated THP-1 cells. Technical variance is estimated based on bulk RNA and ERCC spike data (IFC #2).

3.3 Single-cell RNA sequencing of palmitate-stressed macrophages

3.3.1 Single-cell RNA library preparation and quality control

For single-cell transcriptome analysis of palmitate-activated THP-1 macrophages, we used a microfluidics-based C1 system from Fluidigm [102]. In the C1-based single-cell mRNA preparation workflow, 96 cells were captured in an integrated fluidic circuit (IFC), lysed, single-cell RNA was reverse transcribed and generated cDNA was pre-amplified.

In our experiment we prepared two IFCs: for palmitate-activated and unstimulated cells. Microfluidic wells with captured macrophages were inspected using light microscopy to annotate empty wells and wells with cell doublets (Figure 3-5). From all capture wells 3 %/7 % of the wells contained cell doublets and 13 %/7 % of the wells were empty for palmitate-activated and unstimulated cells, respectively.
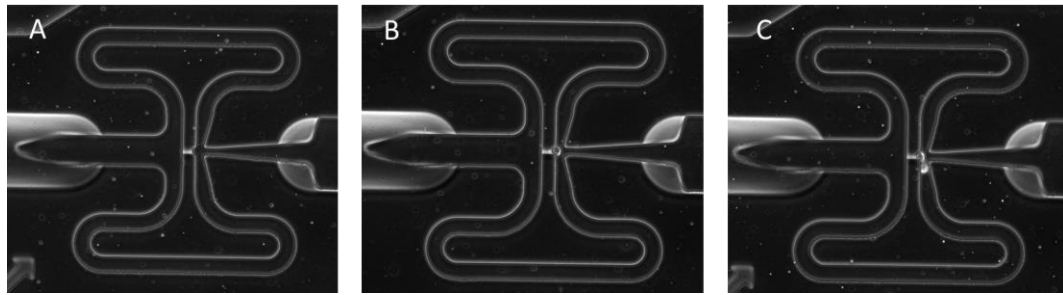
Figure 3-5 Fluidigm C1 Integrated Fluidic Circuit (IFC) with captured THP-1 macrophages.
A Empty capture cite.
B Captured single cell.
C Captured cell doublet**.**

3.3.2 Primary sequencing data analysis

Sequencing was performed for two 96 single-cell library pools (palmitate-stimulated (PAL) and unstimulated (UN)) and for bulk samples from the same cell samples prepared simultaneously in biological triplicates. For single-cell libraries, we obtained 3.7×10^8 and 3.3×10^8 sequencing paired-end reads for palmitate-stimulated and unstimulated cells respectively. The total read number per cell was $(3.9 \pm 0.34) \times 10^6$ and $(3.7 \pm 0.32) \times 10^6$ for PAL/ UN cells.
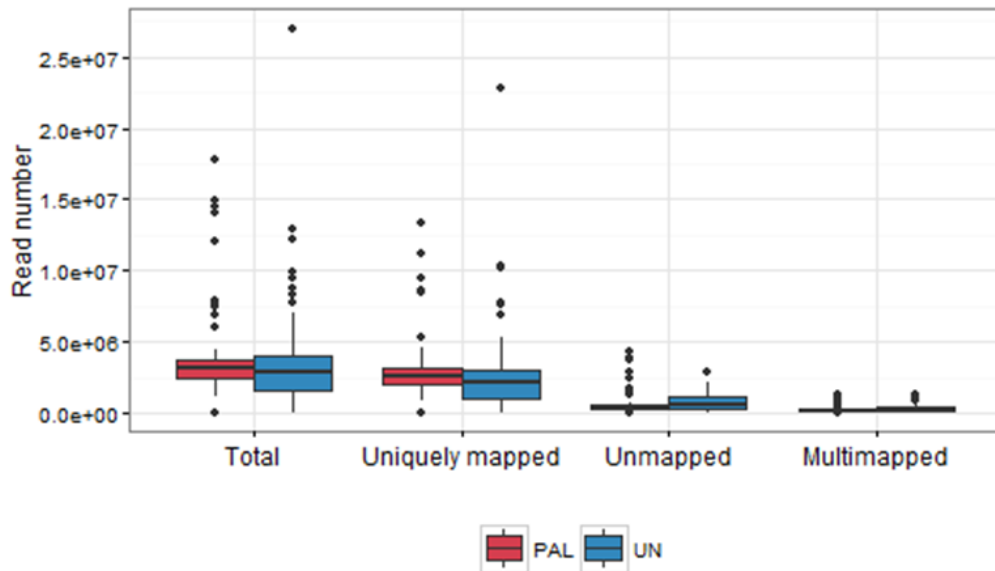
Figure 3-6 Read mapping statistics for single-cell RNA sequencing libraries of palmitate-stimulated (PAL) and unstimulated (UN) cells.

Previously published single-cell studies have shown that a sequencing depth of around 1 million reads per cell and, for specific cases even as low as 50000 reads per cell, is sufficient for representing the complexity of single-cell transcriptomes [102, 105].

For bulk samples, we performed sequencing with high depth to ensure sufficient detection sensitivity for rare transcripts. We obtained $(41.6 \pm 2.6) \times 10^6$ and $(44.2 \pm 3.7) \times 10^6$ reads for PAL/UN samples accordingly.

Quality control of raw sequencing reads demonstrated good results for both single-cell and bulk sequences (Supplementary Figure 7). For most single-cell and bulk samples the mean value of the Phred quality score per base was higher than 28 for all bases in the sequencing reads.

Reads mapping statistics is shown in Figure 3-6, Figure 3-7 and Supplementary Figure 8. On average, 78.4 ± 8.2 % and 65.1 ± 17 % of single-cell sequencing reads and 92.2 ± 0.4 % and 92.2 ± 1.2 % of bulk sequencing reads were uniquely mapped to the reference genome for PAL /UN samples accordingly.
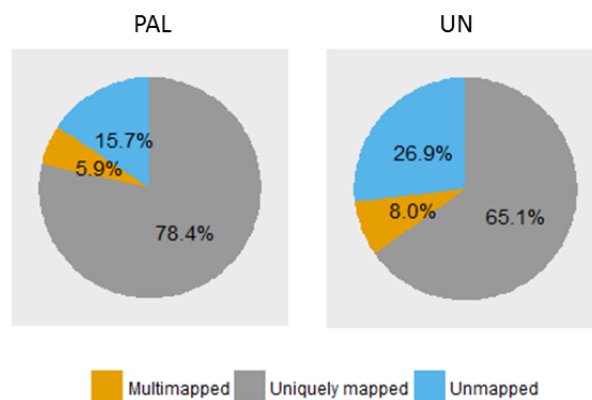
Figure 3-7 Read mapping statistics for bulk RNA samples of palmitate-stimulated (PAL) and unstimulated (UN) macrophages.

To confirm that 96 single-cell sampling is representative of bulk transcriptome from thousands of cells, we looked at the correlation between bulk RNA-seq data and *in silico* pulled single-cell data (Figure 3-8).
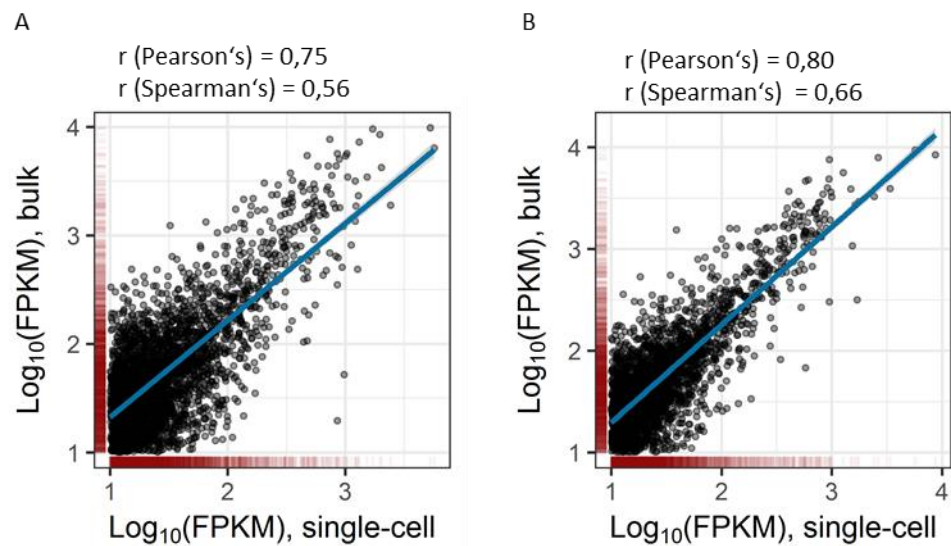
Figure 3-8 Correlation between bulk and _in silico_ pooled single-cell libraries for PAL stimulation (A) and unstimulated (UN) cells (B).
Each dot represents a mean expression value of a single gene.

In both experimental conditions, we observed a high correlation of gene expression: Spearman's r was 0.56 / 0.66 and Pearson's r was 0.75 and 0.80 for PAL/UN respectively. Additionally, we prepared in silico pools of different sample sizes from randomly sampled single cells and measured their correlation with bulk data (Figure 3-9). We observed that both Pearson's and Spearman's correlation coefficients saturated for approximate sample size of 40-60 cells, suggesting that small cell numbers are sufficient to represent bulk transcriptome in our experimental model.
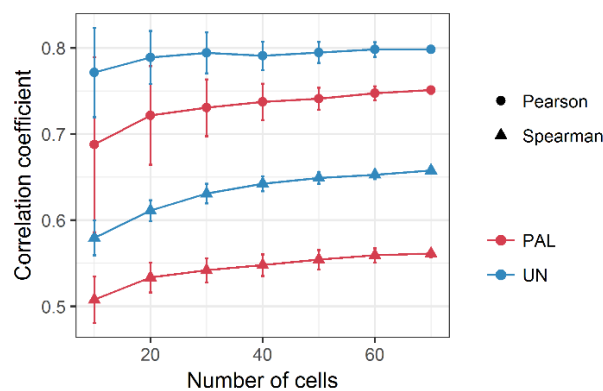
Figure 3-9 Correlation between bulk and single-cell gene expression for random subsets of individual cells. Single-cell average and SD was calculated for 10 random samplings of cells for each data point.

3.4 Differential gene expression analysis of palmitate-stressed macrophages

As a first step in secondary sequencing data analysis, we looked at up- and down-regulated genes in palmitate-stimulated cells compared to unstimulated using bulk RNA-seq data. Overall, we found 453 up-regulated and 242 down-regulated genes with an absolute expression fold change higher than 2 and P-Values lower than 0.001.

We performed gene functional annotation analysis using DAVID software for both groups of genes. For palmitate-induced genes we obtained the highest enrichment for the following pathways, annotated in the KEGG database: cytokine-cytokine receptor interaction, MAPK signaling, TNF signaling, chemokine signaling, NFκB signaling, rheumatoid arthritis and toll-like receptor signaling (Supplementary Table 1). Gene expression fold changes for key induced pathways are shown in Figure 3-11. For down-regulated genes, we did not obtain significant enrichment for any pathways.

As toll-like receptor (TLR) signaling pathway plays an important role in our experimental model, we performed qPCR validation of sequencing data for 84 genes involved in TLR signaling. We observed a high correlation between RNA-seq and qPCR results: Pearson's correlation was 0.66, and Spearman's r was 0.54 (Figure 3-10). All genes that were significantly upregulated based on RNA-seq data and had a fold change higher than 2, were successfully validated using qPCR.
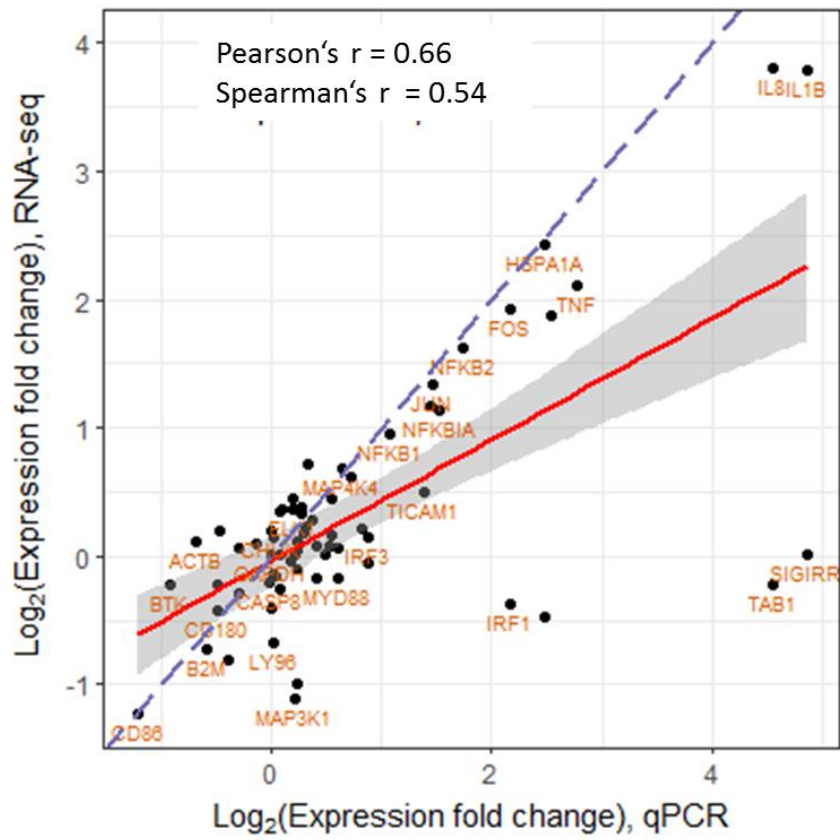
Figure 3-10 Correlation between bulk RNA sequencing and quantitative real-time PCR results for genes, related to the toll-like receptor signaling pathway.

Figure 3-11 Gene expression data for pathways induced by palmitate activation of macrophages.
Shown pathways had the highest significance and gene number in gene functional annotation analysis, based on bulk RNA sequencing data.

3.5 Analysis of macrophage transcriptional states

To analyse cell-to-cell gene expression differences in the palmitate-stressed macrophage population, we applied Independent Component Analysis (ICA). For dimension reduction we used expression data for differentially expressed genes, upregulated in palmitate-stimulated cells. Single-cell expression data was reduced to 2-dimentional independent component space (Figure 3-12). The majority of palmitate-induced cells separated from the unstimulated cell population with independent component 1 (IC 1). IC 2 describes another variability source and shows a broad distribution range for both palmitate-activated and unstimulated cell populations. Strikingly, the IC 2 separated a distinct group consisting of 7 palmitate-stimulated and 2 unstimulated cells.
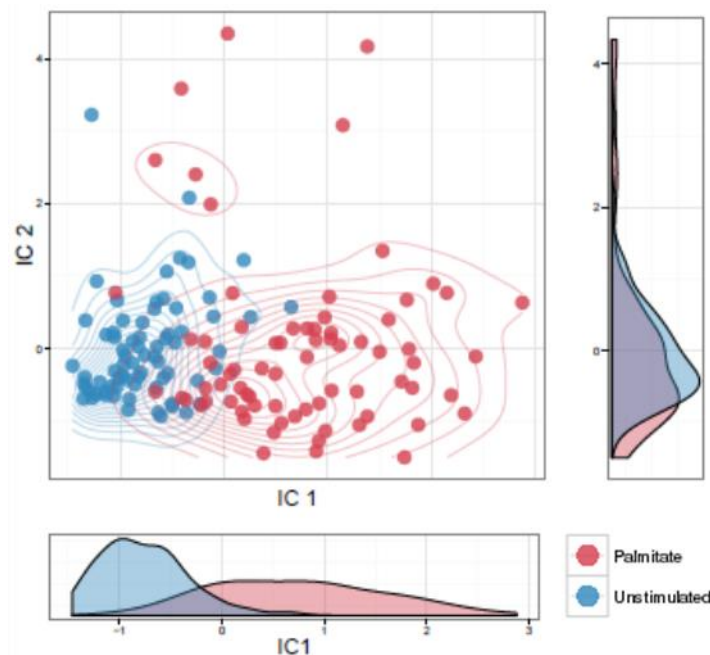
Figure 3-12 Independent Component Analysis (ICA) of single-cell RNA sequencing data.
Each dot represents an individual palmitate-stimulated or unstimulated cell. Side and bottom plots represent cell density distribution along independent components.

We divided palmitate-stimulated cells into 3 states (P1, P2 and P3) based on density distribution along IC 2 (Figure 3-13 A). Three local minimums of density distribution were used to determine limits for separation of the groups. Defined P1, P2 and P3 states contained 51 %, 39 % and 10 % of the cells respectively.

To understand the level of response to applied stress for individual cells, we visualized an average expression values of differentially expressed genes used in ICA (Figure 3-13 B).

We observed that expression of defined genes grows with the increase of IC 1 and IC 2 coordinates. The lowest expression levels we observed in the bottom left corner predominantly for unstimulated cells, as was expected.
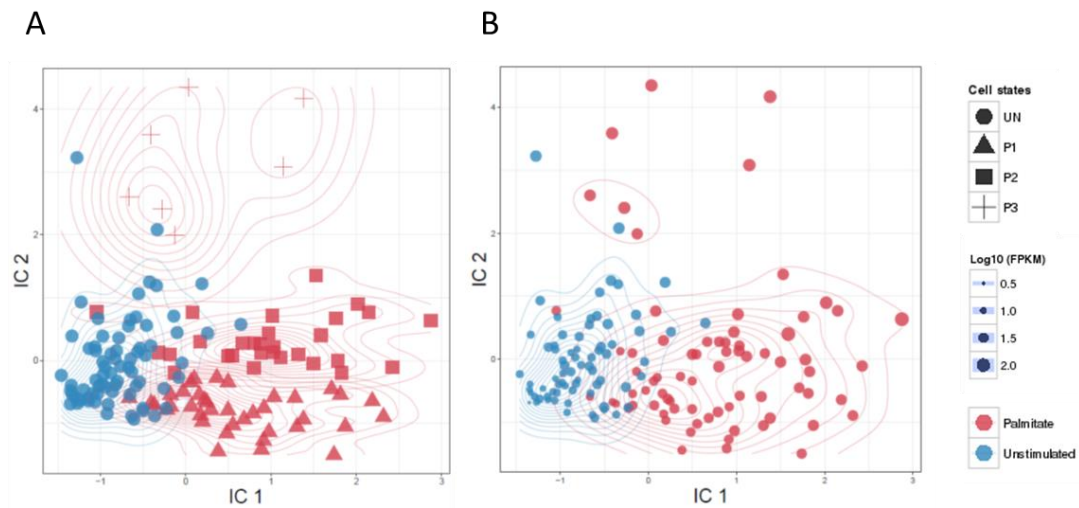

Figure 3-13 Independent Component Analysis of single cells.
A Separation of cell states in 2-dimesional independent component space. Palmitate-stimulated cells were divided into 3 groups (P1, P2 and P3) based on peaks of density distribution along IC 2. **B** Representation of expression levels of differentially expressed genes in individual cells. Log-transformed mean expression of 266 genes, induced by palmitate stimulation in each cell is proportional to dot size.

Additionally, we performed quantitative analysis of the stress response level in each cell group (Figure 3-14). The average expression level for all used DE genes in cell states was 6.4 ± 0.6 FPKM (UN), 10.7 ± 0.9 FPKM (P1), 32 ± 7.4 FPKM (P2) and 46.3 ± 5.9 FPKM (P3). Our cell states annotation clearly represents an overall response level to palmitate-induced stress. Palmitate state P1 representing approximately half of the cells showed a relatively low difference to control cells. States P2 and P3, however, display significantly up-regulated gene expression and represented distinct groups based on ICA and gene expression analysis.
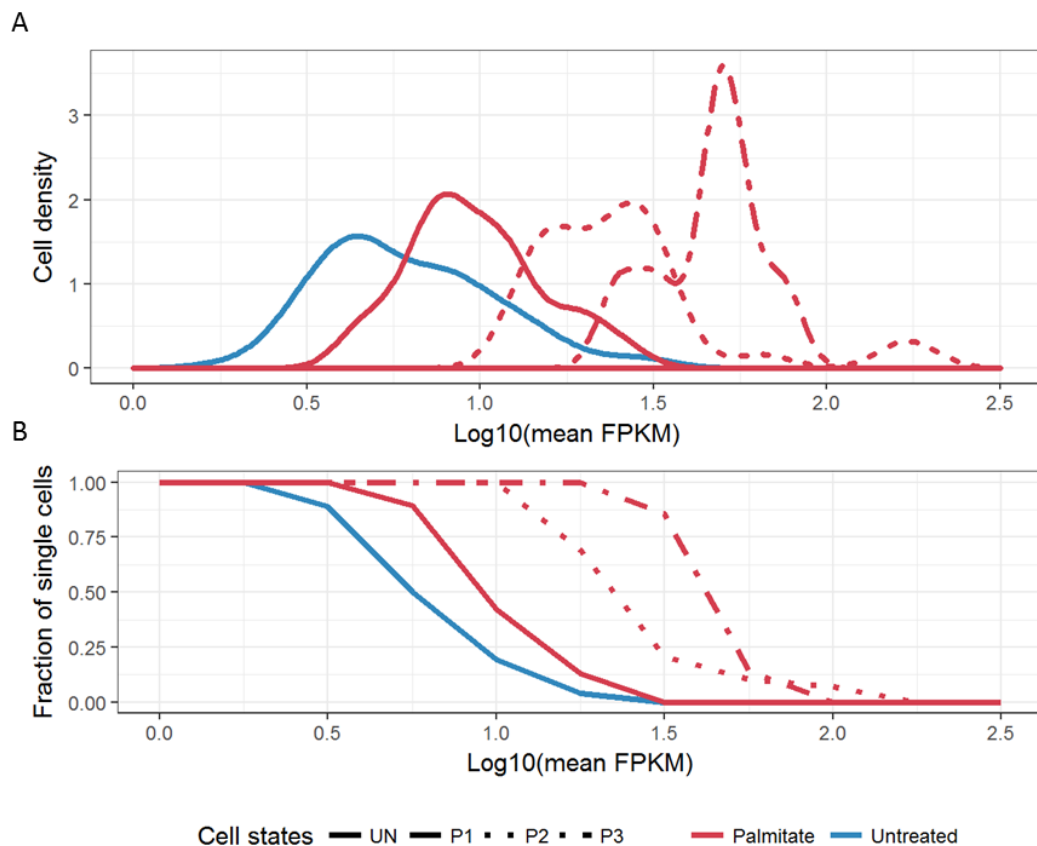
A

B

Figure 3-14 Expression level of palmitate-induced genes in defined cell states.
For each cell, the mean expression of 266 palmitate-induced genes was calculated.
A Cell density shows expression of palmitate-induced genes in cells corresponding to different states.
B The fraction of cells with expression of the defined genes lower than the corresponding level defined on X axis is shown.

To understand how signaling pathways, upregulated in palmitate-activated cells were expressed in individual cells, we visualized an average expression level for each cell in 2-dimensional ICA-space (Figure 3-15 A-C). In addition, we quantified single-cell expression for these genes in each defined cell state (Figure 3-15 D). We observed that palmitate-induced states P1 and P2 showed, on average, similar expression of all 3 pathways (MAPK signaling, TNF signaling and toll-like receptor signaling), but population P2 contained more outliers. Cell state P3 featured the highest expression level for all 3 pathways, in particular for the MAPK signaling pathway and had a very distinct synchronized profile for all cells.
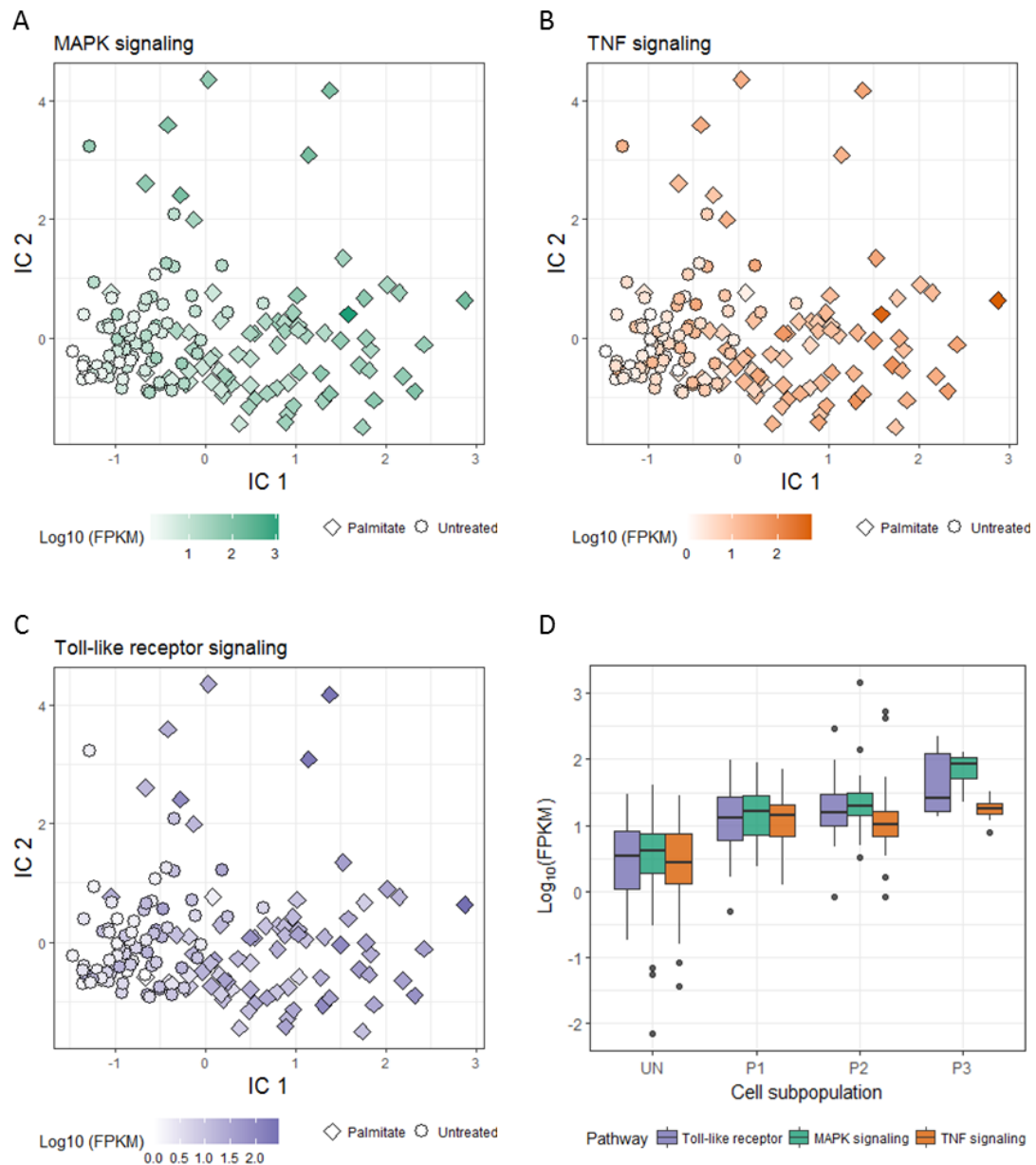
Figure 3-15 Expression of palmitate-induced signaling pathways in individual cells and cell states.
A, B, C Color intensity of each dot in independent component space represents the log-transformed mean expression of the corresponding pathway in an individual cell. D Log-transformed mean expression level for corresponding pathways in previously defined cells states. Each dot represents an individual cell.

Our next step in the analysis of gene regulatory pathways underlying the distinct formation of cell states, was to build gene co-expression networks based on single-cell expression data.

3.6 Weighted gene co-expression network analysis (WGCNA) of palmitate-induced genes

Weighted gene co-expression networks analysis (WGCNA) is a widely used systems biology approach [168-170]. It was originally applied for conventional bulk microarray and RNA-seq data, but several studies recently showed its usefulness for the analysis of single-cell transcriptome data [127, 171, 172]. The WGCNA method is used in our study to describe gene correlation patterns across a cell populations, decipher gene regulatory modules specific for different cell groups, characterize relationships between gene modules and to find important regulatory "hub" genes.

For network construction we used 266 DE genes induced by palmitate stimulation. The same gene set was applied for Independent Component Analysis. First, we used single-cell data for palmitate stimulation to calculate Pearson's correlation coefficient for all DE genes across all single cells.

Next, we applied the soft thresholding approach implemented in the WGCNA package in order to adjust our co-expression network to a scale-free topology network. To determine optimal soft threshold value, we estimated the degree of correlation between our network and the scale free topology model (Figure 3-16 A). Additionally, we calculated the mean gene connectivity within our network (Figure 3-16 B). We selected the soft threshold value $\beta = 10$ as it corresponded to the curve saturation level for both plots.
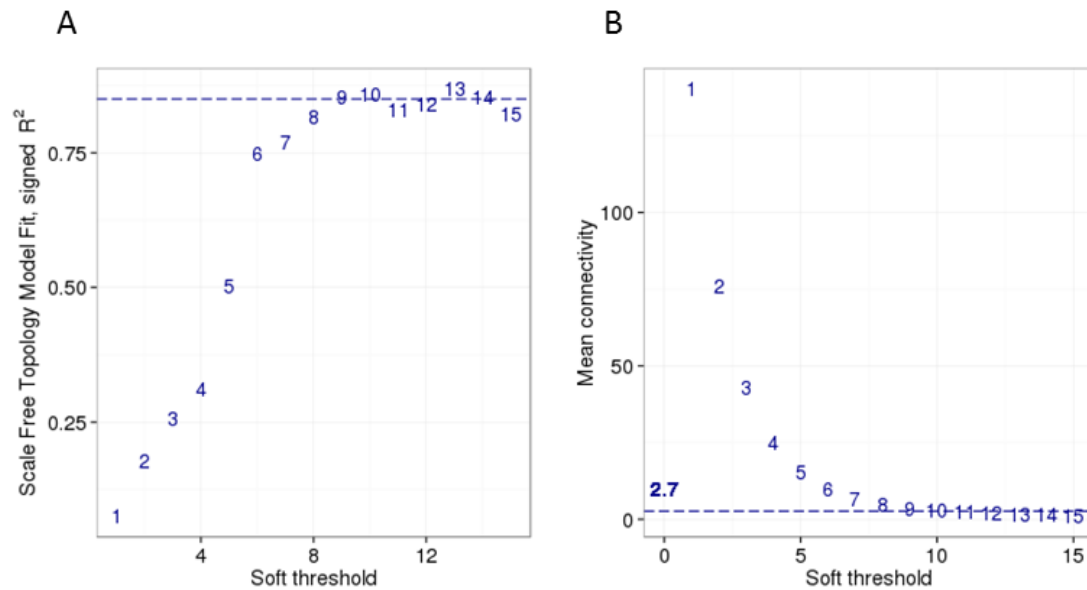
Figure 3-16 Defining optimal soft threshold value for weighted gene co-expression network construction.
A Correlation of constructed network with the scale free topology Model.
B Mean gene connectivity in the constructed network.

As a next step, we calculated the adjacency matrix as follows:

Equation 3-1

$$A i, j = (0.5 * (1 + r_{i,j}(Pearson's)^{\beta}$$

Described transformation is required to obtain positive values as adjacency coefficients. This method of calculating the adjacency matrix is used for "signed" gene networks as it preserves information about the sign of the correlation coefficient. With this method, negative correlation is transformed into small positive values, whereas positive correlation coefficients correspond to higher values in the interval from 0 to 1. For our network with β = 10, adjacency values lower than 9.7×10^{-4} corresponded to negative values of the original Pearson's correlation coefficient.

Based on the adjacency matrix, we calculated a Topological Overlap Matrix (TOM). The heatmap representing obtained TOM is shown in Figure 3-17 C, where red clusters represent highly correlating gene groups. TOM dissimilarity was further used to compute the hierarchical clustering of genes. The hierarchical clustering tree shown in Figure 3-17 A represents the clustering of all 266 genes used in our analysis. To divide clustered genes into modules, we specified the cutting height of the hierarchical tree equal to 0.99 and tested 4 different minimal module sizes (6, 9, 12 and 15). Detected modules are color-

coded and shown in Figure 3-17 B. For the final gene module definition we used annotation with the minimal module sizes of 12 genes. Color representation of selected gene modules and module numbering is shown in the upper and left-side panel of the Figure 3-17 C. Defined modules contain 16, 47, 18, 32 and 41 genes, respectively, for the modules I to V. The remaining DE genes colored in grey could not be assigned to any co-expression cluster.

Due to the low gene number in modules, it was difficult to achieve significant enrichment for annotated pathways in functional gene annotation analysis; however, we did find a number of interesting pathways specifically expressed in detected modules. The first module (green) contained genes involved in cancer transcriptional misregulation (CEBPB, DDIT3, WT1). The largest module II (turquoise) consisted of genes involved in PPAR signaling (CD36, ACSL1, PPARγ, SCD), toll-like receptor and TNF signaling (CD40, IL1β, MAP2K3, CCL20) and MAPK signaling (DUSP1, PDGFA). Modules III and IV (yellow and brown) had significant enrichment (Benjamini–Hochberg corrected P-Value=2.8E-3) for genes involved in cholesterol biosynthesis (HMGCS1 HSD17B7 MSMO1, SQLE). Module V (blue) contained genes related to cytokine-cytokine signaling (CCR, CSF1, IL23A).
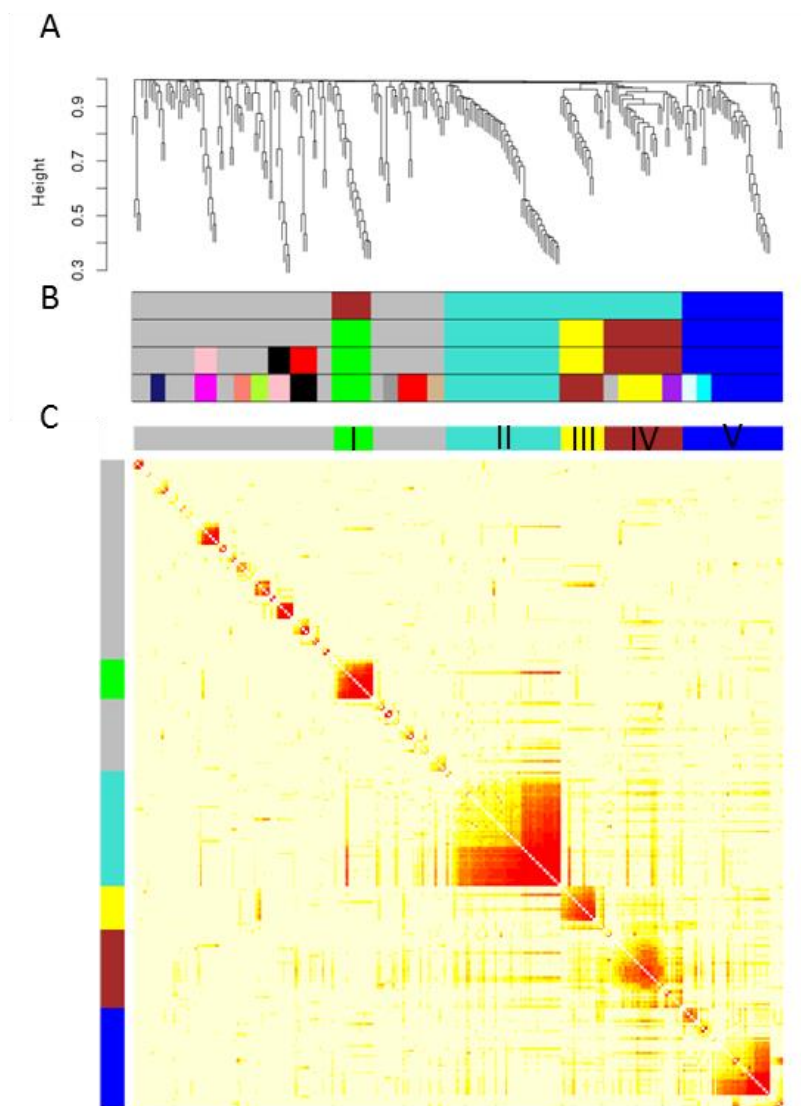
Figure 3-17 Construction of the weighted gene co-expression network.
A Hierarchical clustering of genes based on gene correlation values, represented in a topological overlap matrix.
B Different annotations of gene co-expression modules.
C Topological overlap matrix for the weighted gene network with the selected gene module annotation.

In order to understand key regulatory genes in the constructed weighted gene network, we analysed a subnetwork of transcription factors associated with the defined co-expression modules (Figure 3-18).

Many of the observed transcription factors were extensively described in the context of macrophage activation and polarization in metabolic disease. In Table 3-1 we summarize

information about the regulatory roles of these transcription factors in macrophages and other cells during metabolic stress and immune response.
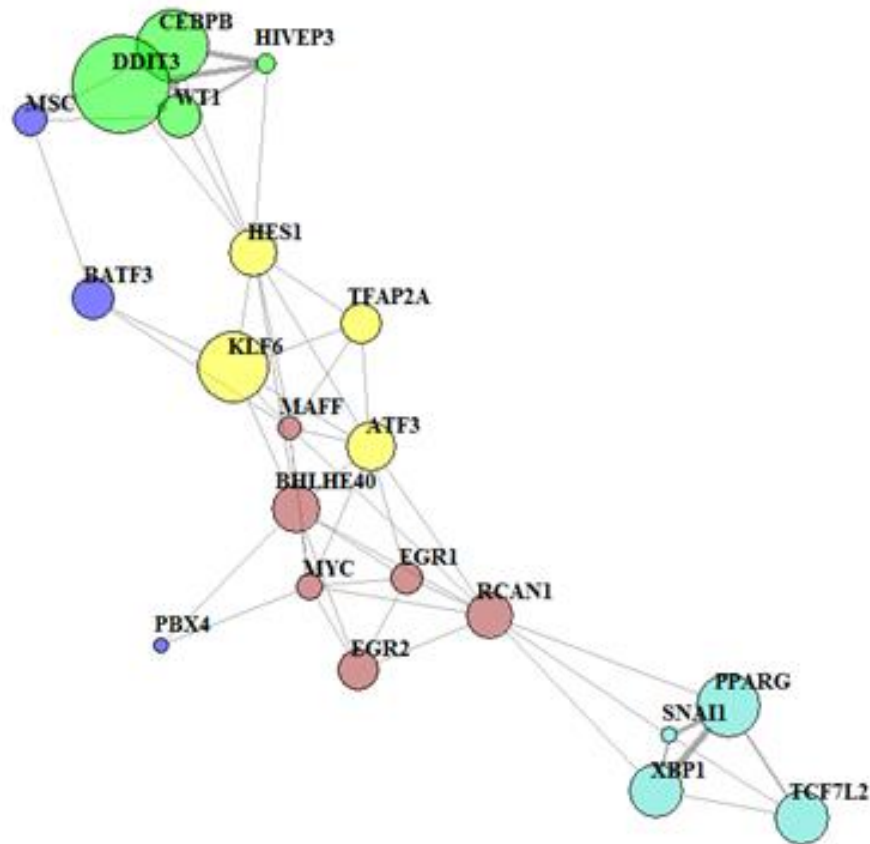
Figure 3-18 Subnetwork of palmitate-induced transcription factors.
Node colours correspond to gene modules, defined for the fully constructed correlation network. Node sizes are proportional to the log-transformed mean expression of each gene across palmitate-stimulated macrophages.

Table 3-1 Palmitate-activated transcription factors regulating identified gene co-expression modules.

Transcription factor	Gene module	Function in macrophage, immune and metabolic stress response	References
DDIT3 (CHOP) DNA Damage Inducible Transcript 3	I	Plays important role in ER stress response, ER associated apoptosis, inflammation modulation.	[173-175]

WT1 Wilms Tumor 1	I	Regulates IL10; overexpressed in acute leukemia.	[176, 177]
CEBPB CCAAT/Enhancer Binding Protein Beta	I	Controversial effects in different studies. Was shown to induce M2 macrophage phenotype, but also associated with HFD-induced inflammation in mouse macrophages.	[178-180]
HIVEP3 Human Immunodeficiency Virus Type I Enhancer Binding Protein 3	I	Negatively regulates cytokine gene expression, regulates NFκB-mediated responses to infection in human fibroblast and macrophage cell lines.	[181, 182]
PPARγ Peroxisome Proliferator Activated Receptor Gamma	II	Key regulator of alternative macrophage activation, improves insulin sensitivity.	[82, 183, 184]
XBP1 X-Box Binding Protein 1	II	Marker of ER stress and Unfolded Protein Response; activated by TLR2/4.	[185, 186]
SNAI1 Snail Family Transcriptional Repressor 1	II	Associated with macrophage migration to injury sites and wound healing.	[187]
TCF7L2 Transcription Factor 7 Like 2	II	Regulates differentiation of monocytes to macrophages.	[188]
ATF3 Activating Transcription Factor 3	III	Plays anti-inflammatory role in macrophages, negatively regulates TLR pathway.	[84, 189, 190]
KLF6 Kruppel Like Factor 6	III	Inhibits anti-inflammatory gene expression by negatively regulating PPARγ expression in macrophages.	[191]
HES1 Hes Family BHLH Transcription Factor 1	III	Inhibits cytokine production in TLR response.	[192]

TFAP2A Transcription Factor AP-2 Alpha	III	Not described in macrophage context. Regulates face and limbs development in embryogenesis, regulates tumor development.	[193, 194]
EGR1 Early Growth Response 1	IV	Regulates macrophage differentiation.	[195, 196]
EGR2 Early Growth Response 2	IV	Induced in M2 macrophages.	[181]
MYC V-Myc Avian Myelocytomatosis Viral Oncogene Homolog	IV	Induced in M2 macrophages.	[197]
RCAN1 Regulator of Calcineurin 1	IV	Promotes atherosclerosis progression, regulates CD36 expression; shown to repress inflammation.	[198-200]
BHLHE40 Basic Helix-Loop-Helix Family Member E40	IV	Promotes inflammation in T-cells.	[201]
MAFF MAF BZIP Transcription Factor F	IV	Induced in M1 macrophages.	[202]
PBX4 PBX Homeobox 4	V	Upregulated in Acute Lymphoblastic Leukaemia.	[203]
BATF3 Basic Leucine Zipper ATF-Like Transcription Factor 3	V	Controls development of thymic dendritic cells.	[204]
MSC (ABF1) Musculin	V	Downstream target of B-cell receptor signaling, induces memory B-cell formation.	[205]

The expression level of defined gene modules in macrophage states is shown in Figure 3-19. For state P1, we observed the lowest expression level for all 5 gene co-expression

modules. As we have already observed in IC space (Figure 3-12), these cells showed a molecular phenotype most similar to unstimulated cells.

Cell state P2 featured significant upregulation of gene module II and pronounced upregulation of gene module I. For gene modules III and IV this state is slightly up-regulated when compared to P1, and for gene module V cells from P1 and P2 showed very similar expression levels.
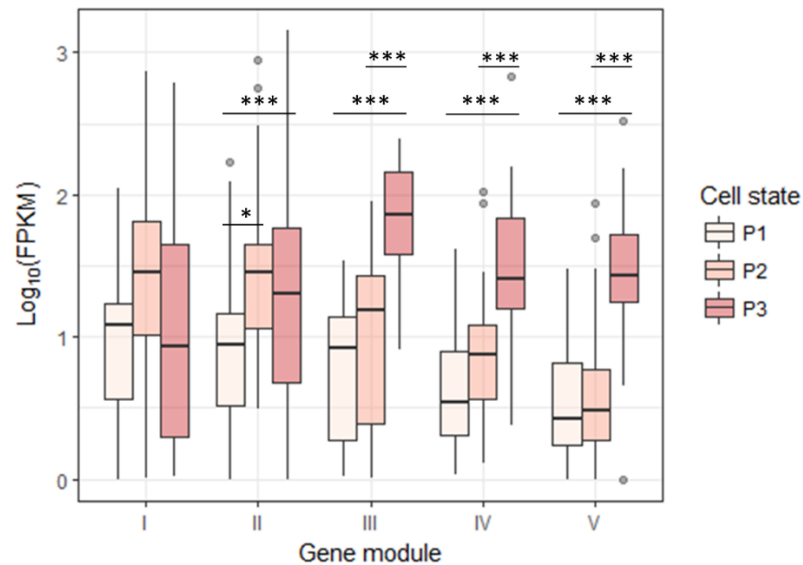

Figure 3-19 Expression of palmitate-induced genes, associated with co-expression modules in defined cell states.
Each dot represents the mean expression of a specific gene across the corresponding cell state. Significance of expression difference between cell groups was tested using ANOVA and Tukey's HSD test. * P-Value < 0.05; ** P-Value < 0.01; *** P-Value < 0.001.

Cell state P3 showed the highest expression level for gene modules III, IV and V, and a highly significant upregulation in comparison with cell state P1 and P2 for these genes. For gene module II the expression of P3 cells is also significantly upregulated compared to cells from P1; however the average expression across state P3 was lower than in P2. For gene module I P3 had on average slightly downregulated expression compared to P2 and P1, although the distribution range for individual genes was very broad.

Summarizing the results, shown in Figure 3-19, we can characterize cell state P1 as low-responsive for all described gene groups. Cell state P2 had an overall intermediate expression of DE genes and exhibited high upregulation in gene modules I and II. Cell state P3 featured significant upregulation of gene Modules III, IV and V, and overall, shows a distinct molecular phenotype as well as high response to palmitate-induced stress.

Figure 3-20 represents the expression level of transcription factors related to defined gene modules in cell states P1, P2 and P3. Overall, individual transcription factors followed the general tendency of having an average gene module expression in these states. All transcription factors from gene modules III, IV and V showed the highest expression in cell group P3. Notably, 4 genes from these modules (TFAP2A, EGR1, MAFF, BATF3) were upregulated in cell population P1 compared to P2.

Based on the analysis represented in Figure 3-18, Figure 3-19 and Figure 3-20 we found cell state P3 particularly interesting, as it showed the highest level of stress response in general. But at the same time, this state revealed a relatively low expression of pro-inflammatory genes like IL1β and IL8, which were restricted to gene co-expression module II. Although both M1- and M2-specific transcription factors belong to gene modules III, IV and V, we assume that ATF3 plays a key role in down-regulating inflammation in P3 cells.

ATF3 has been previously described to inhibit inflammation in HDL stimulated mouse macrophages [84]. In our model we found that ATF3 and IL1β showed mutually exclusive expression (Figure 3-21 A). This result indicates that mediation of inflammation does not occur homogeneously in a concentration-dependent manner in all cells but may rather be controlled by a changing ratio of certain cell phenotypes.
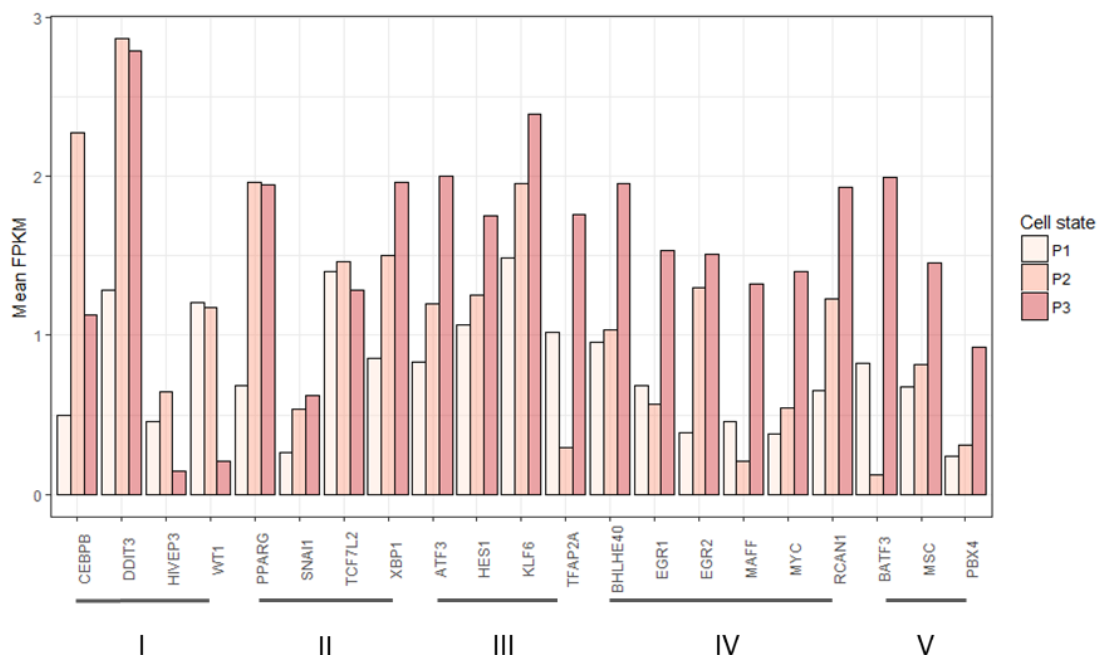
Figure 3-20 Expression of palmitate-induced transcription factors, specific for particular gene co-expression modules in defined cell transient states.
Roman numbers indicate corresponding gene co-expression modules.

3.7 Single-cell quantitative PCR validation of key regulatory genes

We used single-cell quantitative PCR to validate the mutually exclusive expression of ATF3 and IL1β genes which we detected by single-cell RNA sequencing (Figure 3-21). In addition to the previously used THP-1 macrophage model, we prepared identical palmitate stimulation of primary human macrophages, which were isolated from the buffy coats of 3 healthy volunteers.

For THP1 cells, we obtained higher numbers of both ATF3 (RNA-seq – 10.8 %, qPCR – 22.3 %) and IL1β (RNA-seq – 5.4 %, qPCR – 22.6 %) positive cells. This effect can be due to the higher sensitivity of the qPCR method. In qPCR data we also observed 7.1 % of the cells expressing both IL1β and ATF3 genes, indicating that mutual exclusiveness is not absolute, as was suggested by the sequencing data. However, there might be a technical reason for these double positive cells, as in the FACS sorting-based single-cell qPCR method that we used, we could not distinguish between single cells and cell doublets.
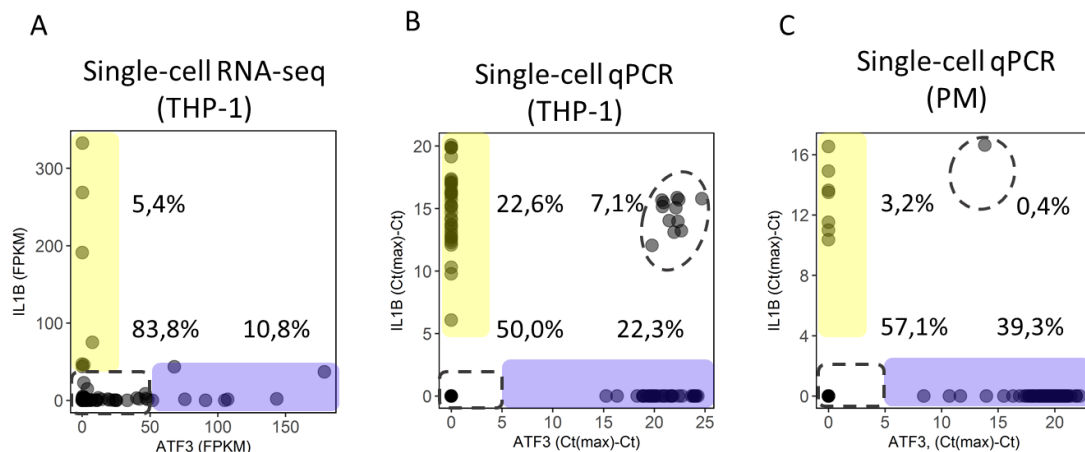
Figure 3-21 Single-cell qPCR indicated mutually exclusive expression of ATF3 and IL1β genes.
A Single-cell RNA sequencing data. Each dot represents expression values (FPKM) in an individual cell.
B, C Single-cell qPCR data for THP-1 (B) and primary human macrophages (C). Each dot represents (Ct$_{max}$-Ct) value in an individual cell.

In primary human macrophages we observed only 0.4 % of ATF3/L1B double positive cells. This is similar to the THP-1 single-cell sequencing results. However, the percentage of inflammatory IL1β positive cells was lower (3.2 %), and the percentage of ATF3 positive cells was almost twice as high(39.3 %).

Overall the single-cell qPCR experiments for both cell models validated our sequencing results for THP1 macrophages and indicated mutually exclusive relationship between ATF3 and IL1β genes.

3.8 Immunofluorescence analysis of macrophages

We further extended our analysis to the protein level by using immunofluorescence (IF) double staining. We applied the IF approach for both THP-1 and primary human macrophages, which were stimulated with palmitate to detect proteins of mutually exclusive genes (ATF3 and IL1β) and highly correlating genes (IL1β and PPARγ).

Immunofluorescence analysis for THP-1 and primary human macrophages was performed using an identical experimental and analytical workflow. After the fluorescence from cells was quantified, cells were filtered based on cell total area and total signal for all three channels in order to exclude outliers. To calculate Spearman's correlation coefficient , we used random sampling of 300 cells per treatment condition to have identical sample size.
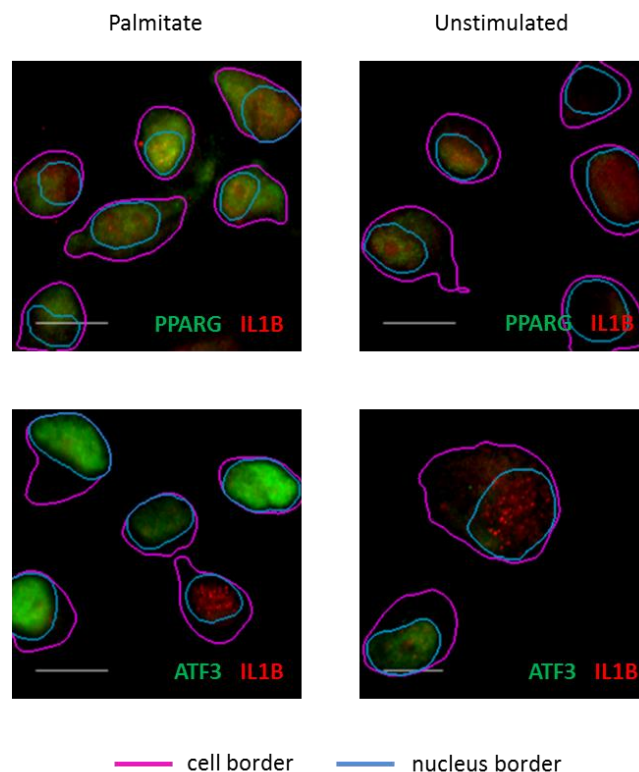
Figure 3-22 IF analysis of THP-1 macrophages.

The immunofluorescence-based Spearman's correlation in THP-1 cells was 0.37 for ATF3/ IL1β and 0.63 for PPARγ/ IL1β (Figure 3-22). The results for highly correlating genes IL1β/ PPARγ were very similar to the gene expression results previously obtained using sequencing and qPCR (0.66 and 0.67 respectively). For ATF3/ IL1β showing mutually exclusive expression, the correlation based on the IF was higher than in sequencing and qPCR data for THP-1 cells (0.011 and -0.06 respectively).

Protein analysis in primary human macrophages produced Spearman's correlation of 0.16 for ATF3/ IL1β and 0.84 for PPARγ / IL1β (Figure 3-23). This corresponds very well with single-cell qPCR results (-0.10 and 0.70 for ATF3/IL1β and PPARγ/IL1β respectively).
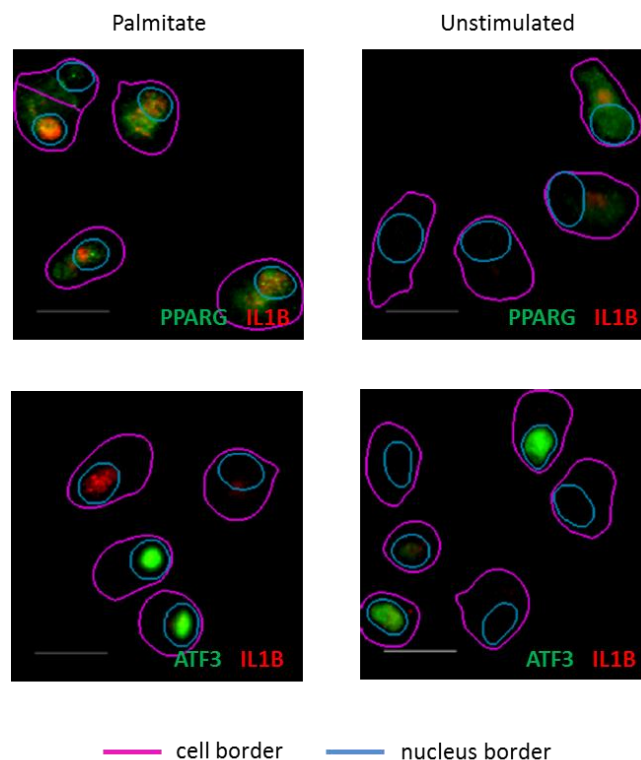
Figure 3-23 IF analysis of primary human macrophages.

The overall protein quantification in individual THP-1 and primary human cells corresponds to single-cell gene expression results and shows similar tendencies for highly correlating and non-correlating genes. For both cell models, we obtained a slightly positive correlation on the protein level for ATF3 and IL1β, which were mutually exclusive based on single-cell RNA-seq. This effect could be due to the biological nature of protein translation and degradation regulation. Additionally, we assume that technical limitations

of the IF technique may have produced a "shift" towards positive correlation as background fluorescence usually appeared in all channels.

3.9 Gene expression variance in macrophages

3.9.1 Variance estimation methods for single-cell gene expression data

Single cell RNA sequencing provides new analytical opportunities for estimation of cell-to cell variation within different cell states. Having whole transcriptome data for individual, stressed macrophages, we are able to quantitatively estimate the level of cell "synchronization" in response to palmitate stimulation for individual genes and gene regulatory pathways. If we look at the density distribution of single-cell gene expression for a specific gene, the standard way of describing dispersion of this distribution would be by utilizing the standard deviation (SD) or coefficient of variation (CV).

The coefficient of variation is commonly used for comparing distributions with different mean values, as we observed in different genes with the mean expression values distributed from 0 to 10^4 FPKM (Figure 3-24 A). However, the CV^2 measured for individual genes across the macrophage population indicated a clear dependency on the mean gene expression level (Figure 3-24 A).

To overcome this limitation, we applied two previously published variance measurements, specifically developed for single-cell variance estimation and independent on the mean gene expression level (Figure 3-24, Supplementary Figure 19).

The first approach was used by A. Kolodziejczyk et al. for variance estimation in populations of embryonic stem cells in mice [114]. In this study, the distance to the median (DM) was used as a measure of gene expression heterogeneity. DM is calculated as a distance between CV squared for a particular gene and the running median fit derived from all detected genes. It is corresponding to the mean expression level of the gene of interest.

We quantified the variance score for single-cell RNA-seq of palmitate-stressed and unstimulated THP1 cells in a similar way by calculation the distance between CV^2 and the corresponding local polynomial regression fitting (Figure 3-24 A). The defined variance score did not correlate with the mean gene expression (Pearson's correlation -0.01) (Figure 3-24 B).

Another method was applied by R. Avraham et al., to measure cell-to-cell heterogeneity in Salmonella-infected macrophages [206]. Cell-to-cell variation was quantified as a distance between expression variance and regression fit, defined for the corresponding mean gene expression level from all detected genes (Supplementary Figure 19 A).

Applying this approach to our macrophage data showed similarities to the results published by Avraham et. al. The quantified variance score was also not correlated with the mean gene expression.

Although both described methods for cell-to cell heterogeneity quantification showed good performance on our single-cell data, the first approach was subsequently used to evaluate variability within palmitate-stressed and unstimulated macrophages, as the underlying statistical model was successfully validated in different single-cell datasets [113, 114, 124].
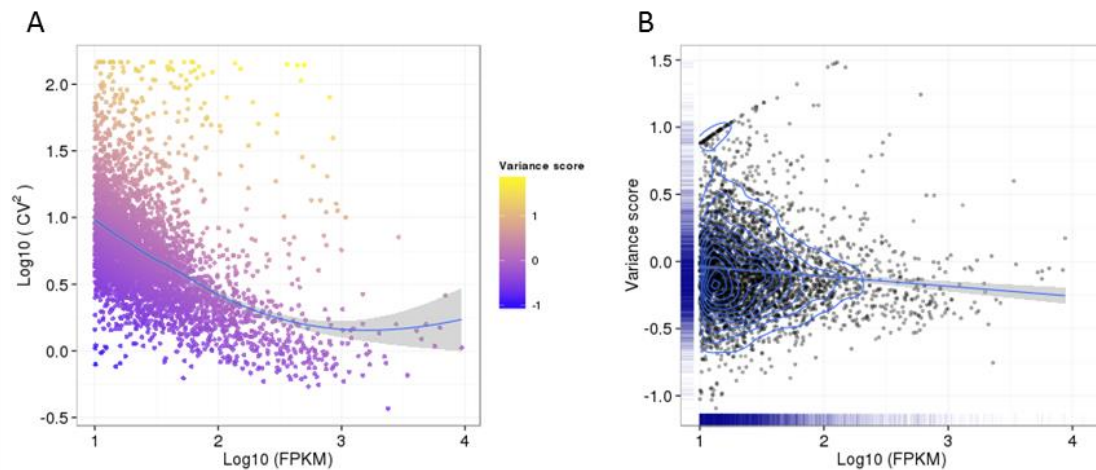
Figure 3-24 Variance score calculation.
A Each dot corresponds to a gene, mean expression level (FPKM) and coefficient of variation (CV) was calculated across all palmitate-stimulated and unstimulated cells.
B Each dot represents a gene. Scatter plot demonstrates relation between estimated variance score and average gene expression (FPKM) quantified across all palmitate-stimulated and unstimuated cells.

3.9.2 Gene expression heterogeneity in stressed macrophages

Using the described variance measurement, we compared heterogeneity of palmitate-stimulated and unstimulated cells and palmitate-induced transcriptional states (P1, P2 and P3) (Figure 3-25). We calculated variance scores for each of the 266 palmitate-induced, differentially expressed genes across corresponding cell groups. We observed that for all described cell groups, the average variance score was lower than zero. This indicates that overall, the selected DE genes have lower variability than the whole transcriptome that was used to build a regression fit.

Although palmitate-stimulated and unstimulated cells visually showed a similar level of "synchronization" (Figure 3-25 A), the difference between the estimated mean variance score was highly significant (Student's t-test P-Value 2×10^{-7}). In palmitate-induced cell states we observed highly significant differences between all three groups (Figure 3-25 B). Palmitate-induced cell state P3 had the lowest level of variability among others and contained a number of outlier genes with a variance score lower than -1. In low responsive cell state P1, the variability level was the highest.
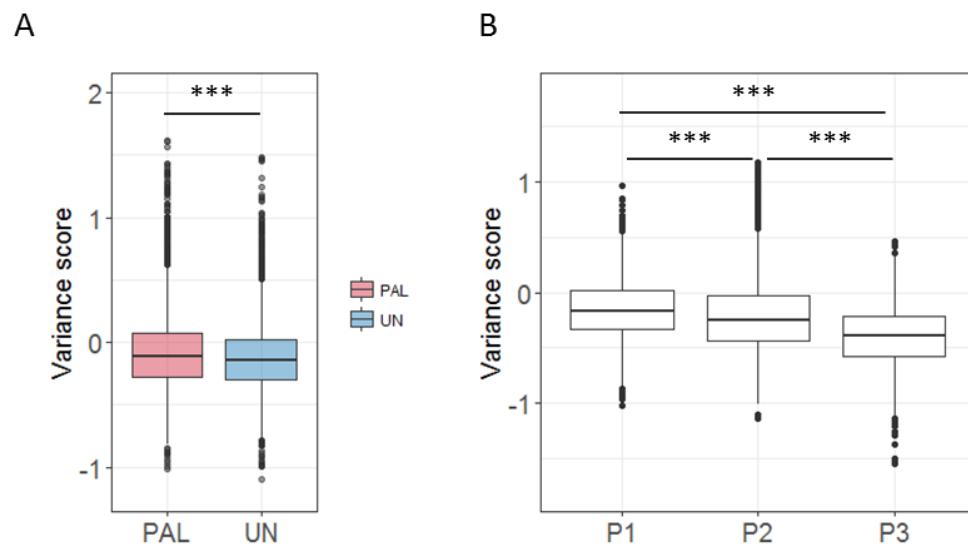
Figure 3-25 Variance estimation for palmitate-induced genes in stressed THP-1 macrophages. Each dot represents a gene. The variance score was quantified across the cells from the corresponding cell group/state.

Next, we looked at the variance in 2 signaling pathways, which were selected using DAVID gene functional annotation analysis and had a sufficient number of highly expressed genes for variance estimation (Figure 3-26). For the described pathways, we observed an analogous tendency for the lowest variance to be observed in P3 cells, whereas cell states P1 and P2 showed comparable levels of heterogeneity. However, the difference between transient states was not significant, due to the small number of observations.
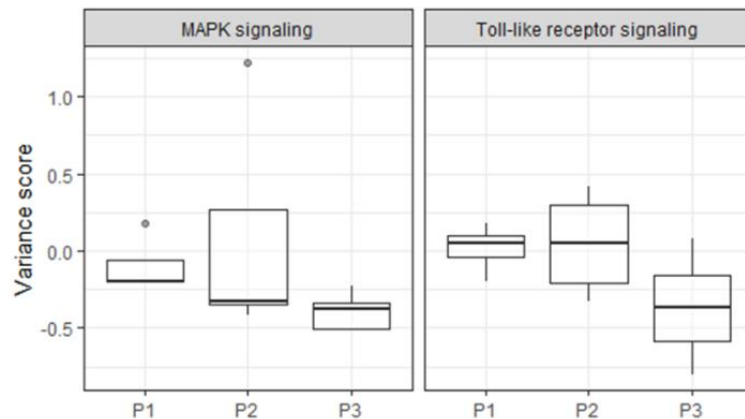
Figure 3-26 Heterogeneity in key regulator pathways.
Variance score was quantified for genes described in DAVID gene annotation analysis (paragraph 3.3) for the corresponding pathways.

Finally, we estimated the variance score in gene co-expression modules, which were identified using weighted gene co-expression analysis (Figure 3-27). We observed the highest variance level for gene modules I and II in palmitate-induced cell state P2, where there was a notably high expression of them. On the other hand, gene modules III, IV and V, highly expressed in state P3, demonstrated an average level of heterogeneity.
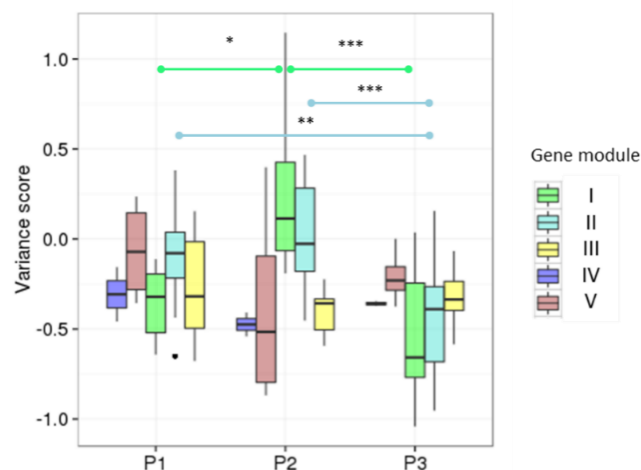
Figure 3-27 Variance estimation for gene co-expression modules identified using WGCNA workflow.

The results obtained for gene co-expression modules are consistent with the variance analysis for all palmitate-induced DE genes, as well as for highly enriched pathways. Cell state P3 demonstrated the highest level of response to stress and low levels of cell-to-cell heterogeneity for different metabolic, stress-associated genes. Cell state P2 had a high response to stress, and the cell diversity in this subgroup was high as well. P1 macrophages showed the lowest response level, similar to unstimulated cells, and had an intermediate level of heterogeneity.

4   Discussion

4.1   Novelty and significance of the research

We present a single-cell whole transcriptome analysis of THP-1 macrophages undergoing metabolic stress caused by free fatty acid stimulation (palmitate). Metabolically stressed THP-1 cells analysed in this study were previously evaluated using RNA sequencing, qPCR and other techniques [207-210]. However, standard approaches averaging gene expression from thousands of cells are unable to describe the natural diversity of macrophages and distinguish signals from distinct cell subpopulations.

The dataset obtained and analysed in this study represents the first single-cell RNA sequencing analysis of obesity-related stress in macrophages. This state of the art approach allowed us to identify distinct cell subpopulations and describe gene regulatory mechanisms defining macrophage identity. We applied a previously described analytical strategy (WGCNA) for the construction of gene co-expression networks that recently proved its efficiency for single-cell sequencing data [127, 171]. The obtained gene network was used to identify previously known overrepresented pathways, as well as novel candidates triggering macrophage phenotypes polarization towards different transcriptional states. Palmitate-induced genes were classified into distinct co-expression modules and the relationship within modules was extensively analysed. This information provides novel hypotheses about key regulatory candidates and can be used for future functional experiments.

We discovered and validated that key regulatory genes (ATF3, IL1β) demonstrate mutually exclusive expression representing distinct cell groups, which proves the concept that system homeostasis is maintained by a certain ratio between distinct types of macrophages. Our findings were confirmed using primary human macrophages both on the gene and protein expression levels.

Our findings shed new light on the regulation of macrophage response to metabolic stress underlying the development of obesity-induced insulin resistance. We described novel candidate genes and their relationship within gene regulatory networks with a special focus on potentially highly relevant transcription factors. The provided data can serve as a valuable resource for future studies.

4.2   Metabolic stress in THP-1 macrophages

THP-1 cell line, firstly established in 1980, has become universally applied in the context of metabolic and cardiovascular disease [131, 211]. Other popular monocytic and

macrophage-like human cell lines include HL-60, U-937, Mono Mac 6 and others. We performed PubMed search analysis (Table 4-1) to estimate the number of studies utilizing different human cell lines. We observed that THP-1 cell were second most popular overall after HL-60 cell and represent the most popular cell line in the context of diabetes.

Generally, the THP-1 cell model is systematically studied in the context of differentiation to macrophages, atherosclerosis, obesity and inflammation and its comparison with primary human macrophages was extensively described. There are several advantages of THP-1 macrophages when compared to other cell lines and primary human macrophages for their application in genomics analysis of metabolic stress.

Table 4-1 Number of studies utilizing different monocytic/ macrophage-like human cell lines according to PubMed search (06/2017).

Cell line	PubMed search term		
	Cell name	Cell name + diabetes	Cell name + inflammation
HL-60	16893	62	564
THP-1	8795	256	1914
U-937	1500	6	86
Mono Mac 6	336	4	47
AML-193	48	0	0
Kasumi-3	8	0	1

First, the isogenic background of THP-1 cells minimizes cell-to-cell bias, which cannot be controlled in primary human macrophages obtained from different donors. Second, the cell cycle of differentiated THP-1 macrophages is inhibited in G1-phase [163]. Genes associated with the cell cycle may significantly complicate the analysis of single-cell transcriptome often representing a major confounding factor defining cell subpopulations. Although several approaches were reported to overcome this limitation, the cell-cycle background cannot be fully eliminated [113, 212].

A technical advantage of THP-1 cells usage for single-cell-based methods is that the cells can be efficiently lysed in diverse types of lysis buffer, as well as in simple water. In single-cell-based approaches there is no reaction purification between cell lysis, reverse transcription and pre-amplification steps. Therefore, the usage of water, as it was implemented in our study for single-cell qPCR, or other standard lysis buffers allows minimization of the inhibitory effects in the following reactions.

Although the PMA-induced differentiation of THP-1 monocytes is well established and characterized, in our experiment we aimed to minimize the potential impact of PMA

stimulation. It was shown that low PMA concentrations, such as 10nM used in our study, are optimal for studying mild stress responses [132].

Additionally, although we demonstrated high concordance between THP-1 and primary human macrophages for our treatment, we observed some gene expression biases between different donors of primary cells, which may be indicative of diverse metabolic, inflammatory and genetic background of donors. For mild metabolic stimulations it is especially important to prevent preliminary cell stress, associated with metabolic and other functions.

4.3 Single-cell RNA sequencing

Single-cell RNA analysis using C1 Fluidigm workflow, and other methods, have now proven their power [103, 105, 123, 127, 137]. However, the efficiency of single-cell experiments may considerably vary between different methods and cell types, therefore accurate validation and estimation of the quality parameters is necessary to obtain unbiased results [101].

To estimate the level of technical noise introduced by the C1 microfluidics-based workflow we performed an independent experiment using a mixture of bulk mRNA from unstimulated THP-1 macrophages, prepared as a control for single-cell samples, and ERCC RNA spike. The mRNA/ERCC spike mix was loaded onto microfluidic IFCs identical to those used for the single-cell experiment. The usage of the ERCC spike in parallel with single-cell library preparation is widely applied. However, the mRNA/ERCC spike mix is not typically analysed [101, 102, 124]. This experiment allowed us to particularly answer the following questions:

1. How strong is the concordance between different C1 microfluidic chips and cell capture microwells within one chip?
2. What level of technical noise is introduced by the applied workflow and is this related to expression levels and other parameters of specific transcripts?
3. How representative is an ERCC spike of human mRNA in a single-cell setting?
4. Are there any systematic biases introduced by the C1 Fluidigm-based workflow?

The results illustrated in Figure 3-3 revealed a strong concordance between different IFCs and individual wells within each IFC. Importantly, this result was confirmed by ERCC spike on the whole-transcriptome level. Overall, the results obtained for ERCC spike were highly representative of the whole transcriptome data. The ratio between mRNA and ERCC molecules in the mix was optimal, with a relatively low fraction of reads mapped to the ERCC reference (approximately 2 %), and the most highly expressed ERCC transcript

exceeding the most highly expressed human mRNA genes (Figure 3-4). We also did not observe any systematic biases for specific IFC microwells.

The variance introduced by technical noise was comparative to the total variance estimated in the single-cell experiment for low read counts (<10 read counts/cell). However, for middle-range (10-100 read counts/cell) and especially for highly expressed genes (>100 read counts/cell) a significant fraction of genes demonstrated biological variance exceeding technical noise (Figure 3-4).

Overall, the applied technology features a number of advantages providing high quality data. The possibility to microscopically detect individual cells captured in microwells allows for control of potential cell doublets and identification of low quality cells, which enabled us to efficiently filter our data. The full-length transcript coverage provides increased accuracy of expression quantification and valuable information regarding transcript isoforms. This method has a high detection sensitivity compared to other single-cell methods allowing the detection of high gene numbers per cell [102].

4.4 Single-cell sequencing data analysis

The choice of optimal analytical workflows is crucial in the analysis of single-cell data to ensure robust and reproducible outcomes. In contrast to commonly analysed data sets, our single-cell data of palmitate-stressed macrophages featured mild changes in gene expression between treatment and unstimulated control as well as between individual cells for each treatment. The optimal workflow had to provide a robust result capturing the differences related to palmitate effects rather than the effects of any unrelated biological or technical factors.

The crucial steps of the workflow that have potentially the highest effect on the result include [100, 101, 118]:

- Choice of read normalization method
- Selection of a gene set for further cell clustering
- Cell clustering method

For our final analytical workflow we selected FPKM read normalization (Cufflinks) and performed cell clustering using ICA based on differentially upregulated genes (palmitate vs. unstimulated). The comparison of different methods for our data set is represented in Supplementary Figure 9-12.

Surprisingly, although the differences between sequencing depth for individual cells were considerable, the unnormalized read counts gave cell clustering results very similar to the FPKM, TPM and size factor normalized reads (Supplementary Figure 9). The normalization

methods slightly changed the distribution between P1 and P2 palmitate cell states, but did not influence the subpopulation P3.

Different gene sets were tested for cell clustering including all detected or highly variable genes (Supplementary Figure 10). Due to relatively low effects induced by metabolic stress, the usage of whole-transcriptome or other gene sets not directly related to palmitate stimulation was not efficient to separate palmitate-stimulated cells from unstimulated in low dimensional space. In our final analytical workflow we focused on stringently selected gene sets including only significantly upregulated genes based on bulk data analysis. This data set allowed us to accurately separate cells from different treatments and further focus on the functional pathways related to the induced metabolic stress response.

We compared commonly used clustering methods applied for single-cell RNA data including PCA, ICA and tSNE for the selected gene sets (Supplementary Figure 11-12) [147]. ICA, which was used for further analysis, and PCA produced similar outcome efficiently separating cells from different treatments, as well as cell states. Data visualization using tSNE revealed more than five small cell states. However, this method was unable to distinguish palmitate-stimulated and unstimulated cells. Additionally, the visualization of common marker genes, associated with M1/ M2 macrophages in tSNE-based coordinates did not reveal any expected patterns.

The final workflow was mainly determined according to the specificity of our data set. Our results demonstrate that the selected approach produces a robust outcome highlighting the effects of palmitate-induced metabolic stress rather than irrelevant factors.

4.5 Transcriptional regulation of macrophage states

Standard functional enrichment analysis of palmitate-induced genes in our data showed significant overrepresentation of the pathways related to inflammatory processes as well as the metabolic stress response, as it was expected, validating the overall applied experimental and analytical approach (Supplementary Table 1). To efficiently utilize the single-cell expression data, we have constructed gene co-expression networks based on empirically obtained correlations between genes in single-cells. This approach allows to associate genes and gene modules to the specified cell groups and decipher potentially important regulatory connections.

The detected gene modules were clearly assigned to cell states underlying the regulation of macrophage heterogeneity. Most of the genes associated with inflammation clustered into the largest module (II), expressed in M1-like cells (P2 state). Another module (I), specifically expressed in M1-like cells contained known ER-stress markers including DDIT3

and XBP1. Interestingly, in M1-like cells we found several transcription factors that have not been previously associated with M1 macrophages (PPARγ, CEBPB, HIVEP3).

PPARγ is widely studied as an important regulator of alternative macrophage activation. High fat diet-fed mice with the depletion of PPARγ in macrophages demonstrate increased insulin resistance and glucose intolerance [82]. Synthetic PPAR activators, thiazolidinediones (TZDs), represent highly efficient anti-diabetic drugs. However, the lack of knowledge of PPARγ -related transcriptional networks and their complexity is limiting further treatment improvement that would overcome TZDs-related side effects [213]. In our single-cell data we observed that PPARγ was highly expressed in M2-like cells (P3 state), but also had very high expression in a small proportion of M1-like cells (Supplementary Figure 14). We assume, that PPARγ response might be differently regulated in the context of different cell transcriptional states depending on the presence of other transcription factors, epigenetic and metabolic cell state and other factors, as it was suggested by previous studies [213].

Similarly, the expression of transcription factor CEBPB was on average the highest in M2-like cells. However, it was also highly expressed in some M1-like cells. Interestingly, CEBPB was described both in context of pro- and anti-inflammatory regulation [178-180]. Generally, its functions were shown to be dependent on post-translational modifications [214, 215] and we assume that its gene regulatory activity may be potentially influenced by cell transcriptional states.

Gene modules specific for M2-like macrophages (P3 state) contained known transcription factors inhibiting TLR response (ATF3, HES1), but also some pro-inflammatory regulators (KLF6, MAFF). Interestingly, M2-like cells were also regulated by several transcription factors related to adaptive immunity (MSC, BATF3, BHLHE40).

Activating transcription factor 3 (ATF3), specifically expressed in M2-like macrophages has been studied as an inhibitor of pro-inflammatory signaling in macrophages and other cells [190, 216, 217]. Its beneficial role has been demonstrated in the context of atherosclerosis, acute liver inflammation, pressure overload heart failure and inflammation of human fetal membranes [84, 216, 218, 219]. ATF3 has been shown to inhibit several inflammation-related genes including IL6, IL12, TNF, iNOS, IFNγ, CSCL10 and others [189, 220, 221]. In a recent study published by J.-W. Kwon et al. ATF3 expressed upon LPS stimulation in RAW 264.7 cells was demonstrated to bind the p65 subunit of NFκB in a complex with histone deacetylase 1 (HDAC1), suggesting that ATF3 assists in p65 deacetylation [222] . In our analysis, ATF3 was identified as an important regulator of anti-inflammatory signaling in M2-like cells (P2). The mutually exclusive expression between

ATF3 and IL1β demonstrates a novel view on pro- and anti-inflammatory regulation in metabolically stressed macrophages.

Another highly interesting transcription factor, appearing on the border of pro- and anti-inflammatory gene co-expression modules is RCAN1. The number of publications about this gene is very limited so far. In a recent study reported by H. Peiris et al. RCAN1, located on chromosome 21, was identified as a key regulator connecting trisomy 21 with β-cell mitochondrial dysfunction in T2D [223]. Authors observed reduced glucose-stimulated insulin secretion and β-cells mitochondrial dysfunction *in vivo* in mice overexpressing RCAN1. In another study, published by N. Mendes-Barbero et al., a dominant role of RCAN1 was described in the context of atherosclerosis [199]. They reported that Apoe(-/-) mice with genetically inactivated Rcan1 featured reduced atherosclerosis development and had higher expression of anti-inflammatory markers compared to Apoe(-/-).

The described transcription factors as well as other regulatory hub genes demonstrated interesting expression patterns in cell states and exhibited many unexpected gene connections (Figure 3-20, Supplementary Figure 14). The obtained single-cell data allows for accurate analysis of gene regulatory mechanisms in the context of different transcriptional states. We assume, that potential future functional experiments targeted on specific genes and their functions in the context of obesity-induced inflammation and insulin resistance will provide novel insights in this field.

4.6 Future perspectives

In this study we demonstrate the diversity of macrophage transcriptional states induced in an isogenic cell population by a single trigger producing mild metabolic stress. Assuming the complexity and heterogeneity of signals affecting macrophage behavior *in vivo*, the single cell approach is crucial for accurate analysis and re-evaluation of macrophage transcriptional states.

In particular in the context of metabolic stress and type 2 diabetes as well as immune response, the analysis of macrophage metabolome on single-cell level may play important role. Although the technology for single-cell metabolic profiling is new and no biological applications were obtained so far, a lot of advances were made in the field, in particular in techniques based on mass spectrometry [224].

In addition to transcriptome, genome and epigenome profiling of individual cells including simultaneous detection techniques are highly interesting [225-228]. Additionally, much progress was observed in methods development for space- and time resolved analysis of individual cells [229-232].

Generally, we assume that macrophage studies and many other fields will significantly benefit from the development of various single-cell analysis methods. The upcoming Human Cell Atlas project as well as more targeted studies utilizing single-cell methods will provide novel view on cell type and transcriptional states classification, and will serve as a valuable resource for future research [233].

5   Summary

Obesity-induced metabolic disorders and type 2 diabetes have become global burden in the last decades causing a number of deaths and significant social and economical damage. Chronic inflammation underlies obesity-induced development of insulin resistance, cardiovascular disease and metabolic syndrome. Chronic inflammation is mainly caused by increased accumulation and activation of various immune cells in obese tissues. Macrophages play a particularly important role in the development of this pathological process. Previous studies described pro-inflammatory M1 and anti-inflammatory M2 macrophage states and the role of imbalance between M1 and M2 macrophages in the development of chronic inflammation. However, growing evidence of macrophage diversity in health and disease requires more accurate analysis of macrophage molecular phenotypes.

In this study we used single-cell transcriptome analysis of macrophages, stimulated with high levels of FFAs typical for obese adipose tissue microenvironment. Analyzing full transcriptomes of individual cells, we were able to distinguish 3 macrophage transcriptional states and decipher gene regulatory pathways underlying macrophage state identity. We also quantified the level of cell-to-cell variability for different pathways and gene co-expression modules to distinguish highly robust and "noisy" molecular mechanisms. These results can be used for further gene perturbation experiments to better understand their role in macrophage response to metabolic stimulation. We show that pro-and anti-inflammatory genes and pathways act in a mutually exclusive way in distinct macrophage states. We identified ATF3 as one of the important transcription factor, suppressing fatty acids-induced inflammation, to be expressed in a mutually exclusive manner with inflammatory mediator genes such as IL1β. The results obtained for well-controlled isogenic THP-1 macrophages were validated using primary human macrophages.

Overall, our findings demonstrate that macrophages form distinct states in response to stress and the ratio between cell states seems crucial for homeostasis regulation. Our results contain valuable information of highly correlating gene modules, specifically expressed in distinct cell states as well as information about newly described genes in such context. These findings represent a valuable resource for future studies of molecular mechanisms of obesity-induced insulin resistance and type 2 diabetes.

6 Zusammenfassung

Stoffwechselstörungen und Typ-2-Diabetes infolge von Fettleibigkeit sind in den letzten Jahrzehnten zu einer globalen Belastung geworden und für eine Reihe von Todesfällen sowie soziale und wirtschaftliche Schäden verantwortlich. Chronische Entzündungen spielen bei der durch Fettleibigkeit induzierten Entwicklung von Insulinresistenz sowie bei der Entstehung der Herz-Kreislauf-Erkrankung und des metabolischen Syndroms eine entscheidende Rolle. Chronische Entzündungen werden hauptsächlich durch eine erhöhte Ansammlung und Aktivierung verschiedener Immunzellen im Fettgewebe verursacht. Makrophagen spielen bei der Entwicklung dieses pathologischen Prozesses eine besonders wichtige Rolle. In früheren Studien wurden pro-inflammatorische M1- und anti-inflammatorische M2-Makrophagen-Zustände sowie die Rolle des Missverhältnisses zwischen M1- und M2-Makrophagen im Rahmen der Entwicklung chronischer Entzündungen beschrieben. Allerdings wird im Hinblick auf die Bereiche Gesundheit und Krankheit durch die zunehmenden Hinweise auf Makrophagen-Diversität eine genauere Analyse der molekularen Phänotypen von Makrophagen erforderlich.

In dieser Studie führten wir eine „Einzelzelle-Transkriptom-Analyse" von Makrophagen durch, stimuliert mit einer hohen Menge FFAs, die für die Mikroumgebung des Fettgewebes bei fettleibigen Personen typisch sind. Durch die Analyse von kompletten Transkriptomen individueller Zellen waren wir in der Lage, drei transkriptionelle Makrophagen-Zustände zu differenzieren und Gen-regulierende Bahnen, die der Identität von Makrophagen-Zuständen zugrunde liegen, zu entschlüsseln. Außerdem ist es uns gelungen, das Maß der Zelle-zu-Zelle-Variabilität der verschiedenen Bahnen sowie die Module der Co-Expression der Gene zu quantifizieren, um besonders stabile und "laute" molekulare Mechanismen zu differenzieren. Diese Ergebnisse können für weitere Versuche zur Gen-Perturbation genutzt werden, um deren Rolle bei der Makrophagen-Reaktion auf Anregung des Stoffwechsels besser zu verstehen. Wir zeigen, dass pro- und anti-inflammatorische Gene und Bahnen in sich einander ausschließender Weise in verschiedenen Makrophagen-Zuständen wirken. Als einen der bedeutenden Transkriptionsfaktoren haben wir ATF3 identifiziert - dieser unterbindet die durch Fettsäuren induzierten Entzündungen, wobei in sich einander ausschließender Weise mit inflammatorischen Mediator-Genen wie zum Beispiel IL1β exprimiert wird. Die Ergebnisse, die im Hinblick auf gut kontrollierte, isogene THP-1-Makrophagen ermittelt worden sind, wurden mithilfe primär menschlicher Makrophagen validiert.

Insgesamt zeigen unsere Erkenntnisse, dass Makrophagen als Reaktion auf Stress unterschiedliche Zustände annehmen, während das Verhältnis zwischen den Zuständen der Zellen für die Homöostase-Regulierung von zentraler Bedeutung zu sein scheint.

Unsere Ergebnisse umfassen wertvolle Informationen zu in hohem Maße korrelierenden Gen-Modulen, die speziell in verschiedenen Zellzuständen exprimiert werden, sowie außerdem in diesem Zusammenhang Informationen zu neu beschriebenen Genen. Im Hinblick auf zukünftige Studien an molekularen Mechanismen von Insulinresistenz und Typ-2-Diabetes aufgrund von Fettleibigkeit stellen diese Erkenntnisse eine wertvolle Ressource dar.
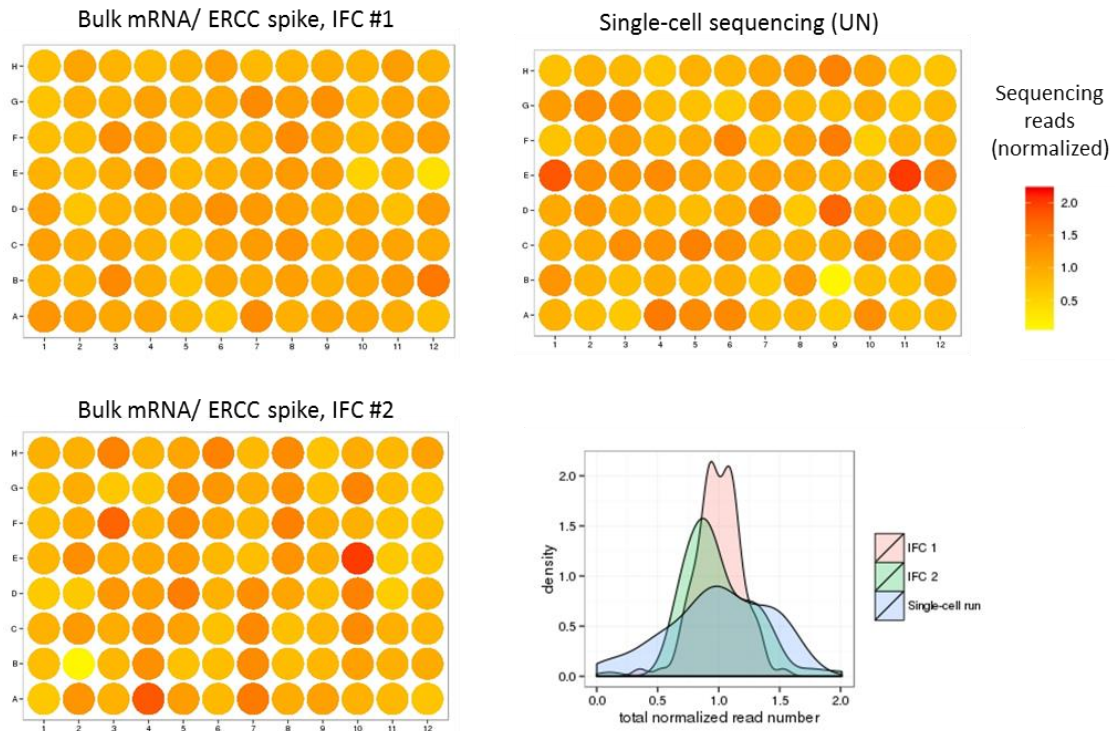
7 Supplementary Materials

7.1 Supplementary figures and tables

Supplementary Figure 1 Cell cytotoxicity detection of THP-1 macrophages treated with different palmitate concentrations.
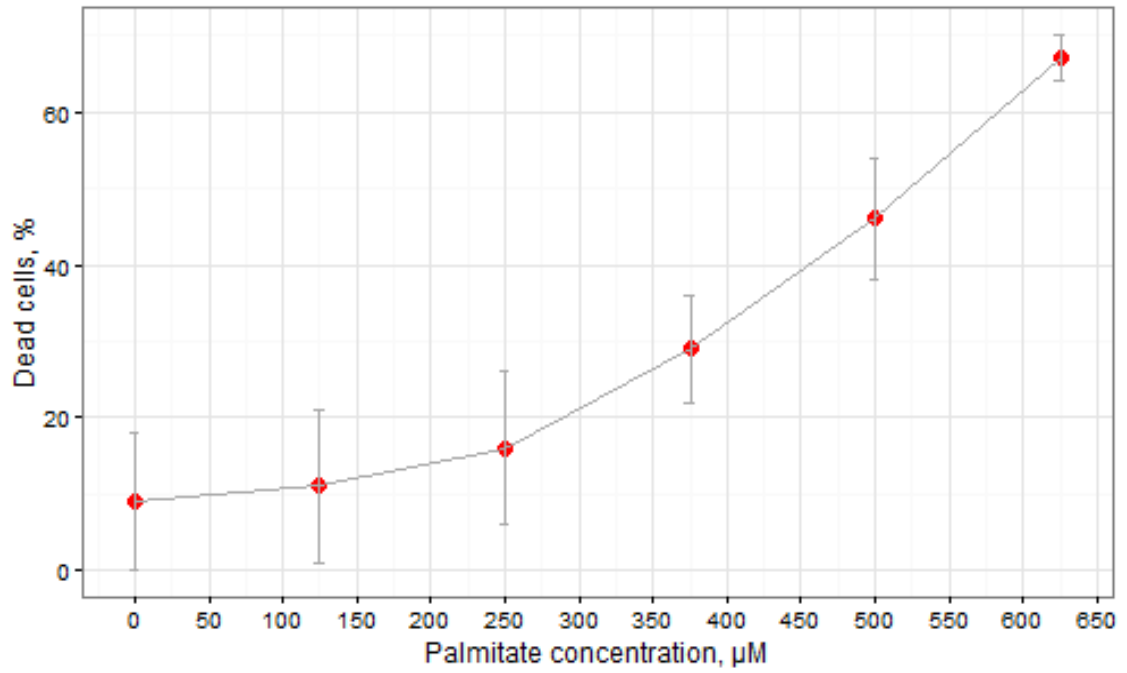
Supplementary Figure 2 Estimation of technical variability between IFC wells and well-specific technical biases.
Normalized total number of sequencing reads obtained for each well for bulk RNA combined with ERCC spike (IFC 1 and IFC 2) and single-cell sequencing (unstimulated cells) are shown in 96-plate layout. Density distribution indicates variability in read number output from 96 microfluidic wells for each IFC.

Supplementary Figure 3 Principal Component Analysis (PCA) of ERCC spike in Fluidigm C1 workflow.
Each dot represents a well from standard 96-well layout for each of the two analysed microfluidic IFCs.
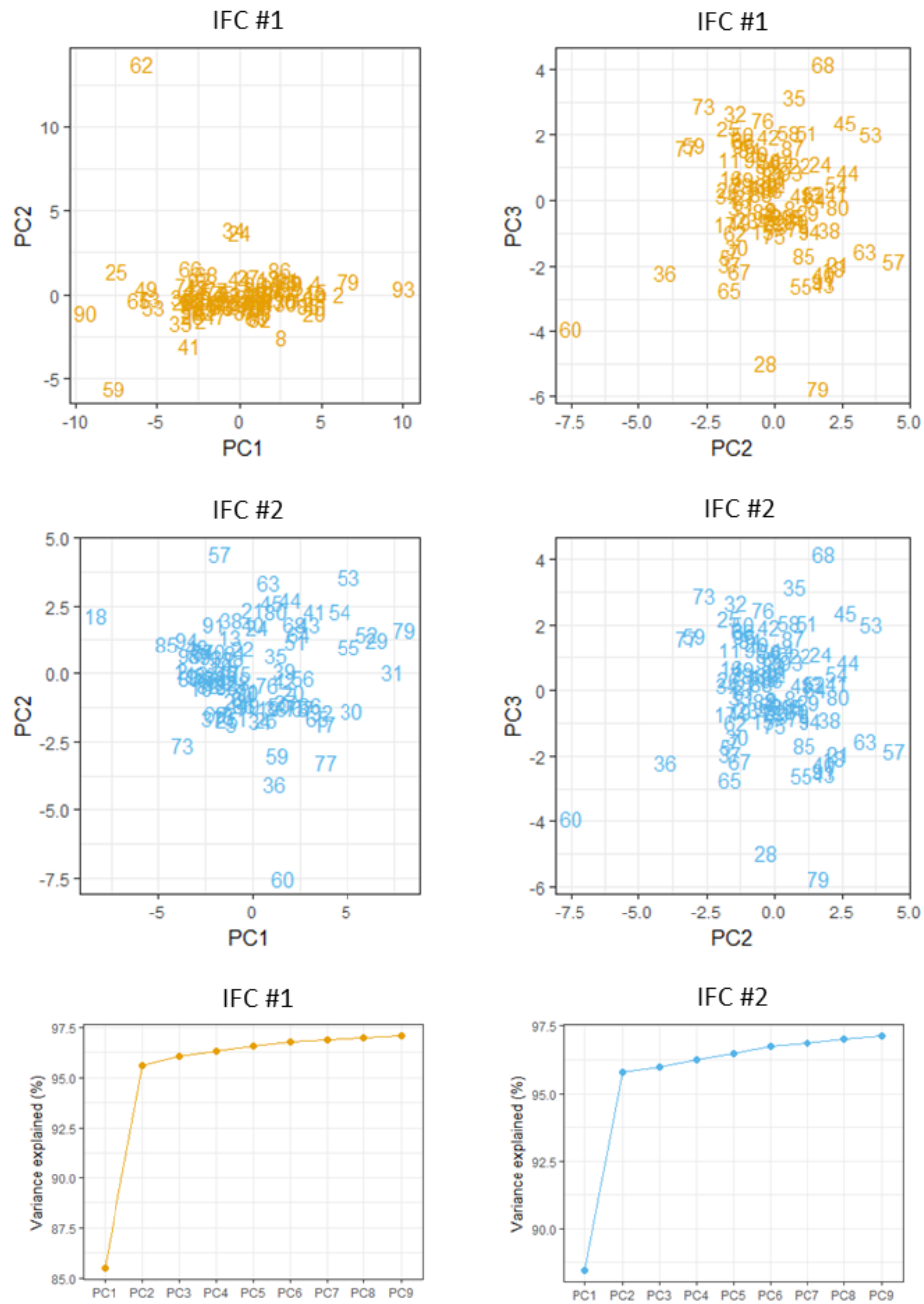
Supplementary Figure 4 Principal Component Analysis (PCA) of bulk mRNA in Fluidigm C1 workflow.

Each point represents a well from standard 96-well layout for each of the two analysed microfluidic IFCs.
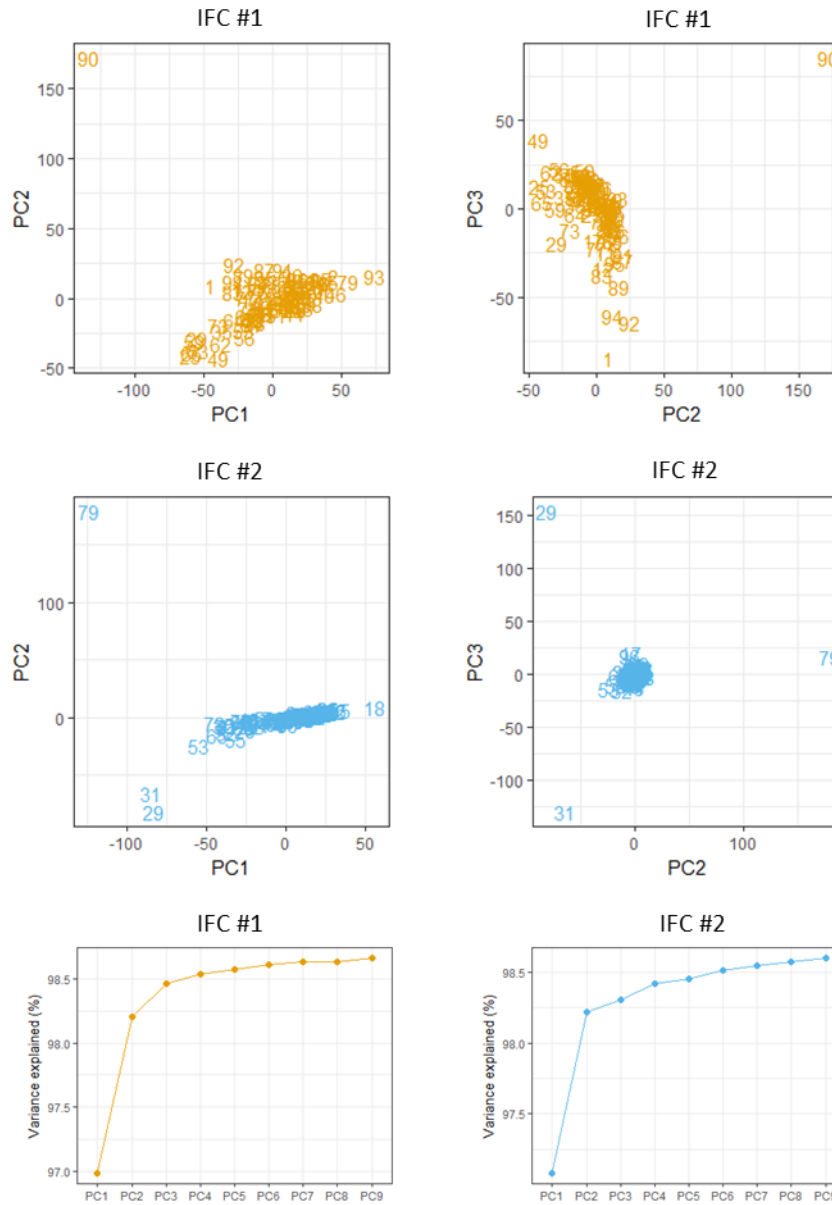
Supplementary Materials

Supplementary Figure 5 Gene variance versus expression for bulk RNA/ ERCC spikes sequencing.
Generalized linear fit, based on scatter plot represented in Figure 3.27 is shown.
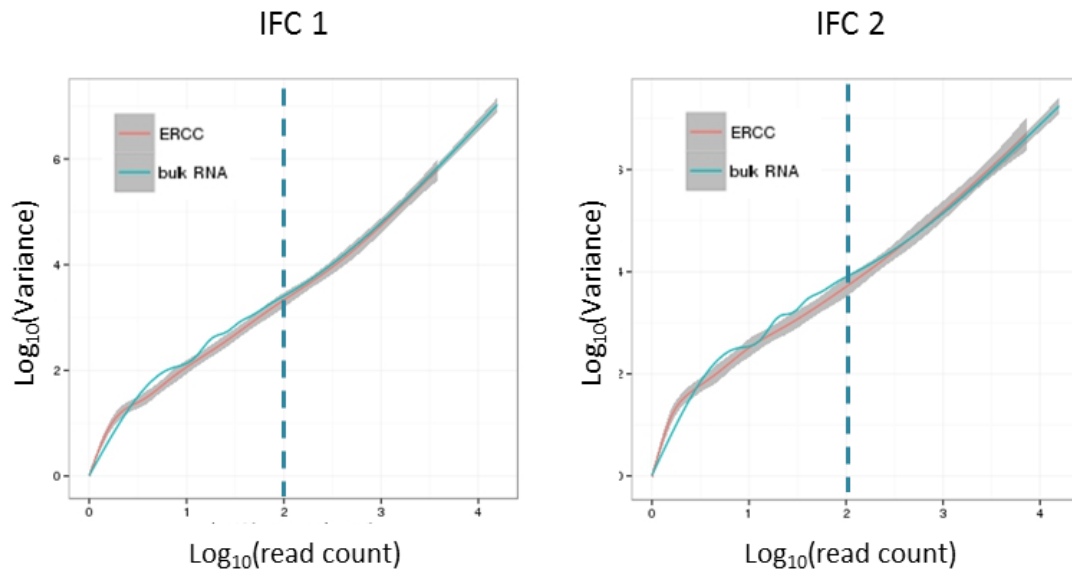
Supplementary Figure 6 Quality control of preamplified single-cell cDNA and single-cell sequencing library pools using Bioanalyzer.
A Preamplified cDNA from an individual representative cell after harvesting from C1 IFC.
B Preamplified cDNA from empty well of C1 IFC.
C, D Analysis of single-cell library pools for unstimulated (C) and palmitate-stimulated (D) macrophages.
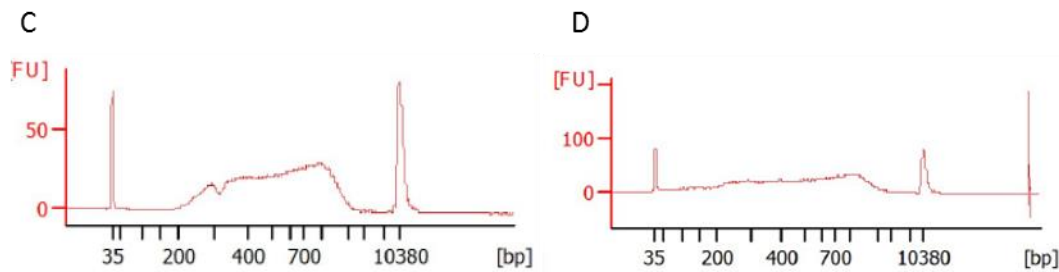
Supplementary Figure 7 Quality control of representative FASTQ files for single-cell and bulk RNA samples.
Plots represent standard output files of FastQC software.
A, C Per base sequencing quality figures for selected samples. Red line represents median and blue line represents mean Phred quality score for each base in a sequencing read. Yellow box represents inter-quartile range (25-75 %) and upper and lower whiskers indicate 10 % and 90 % of data points.
B, D Distribution of read quality for all reads corresponding to selected samples.

Single-cell RNA-seq FASTQ quality control

C

Bulk RNA-seq FASTQ quality control

Quality scores across all bases (Sanger / Illumina 1.9 encoding)

Position in read (bp)

D

Quality score distribution over all sequences

Average Quality per read

Mean Sequence Quality (Phred Score)
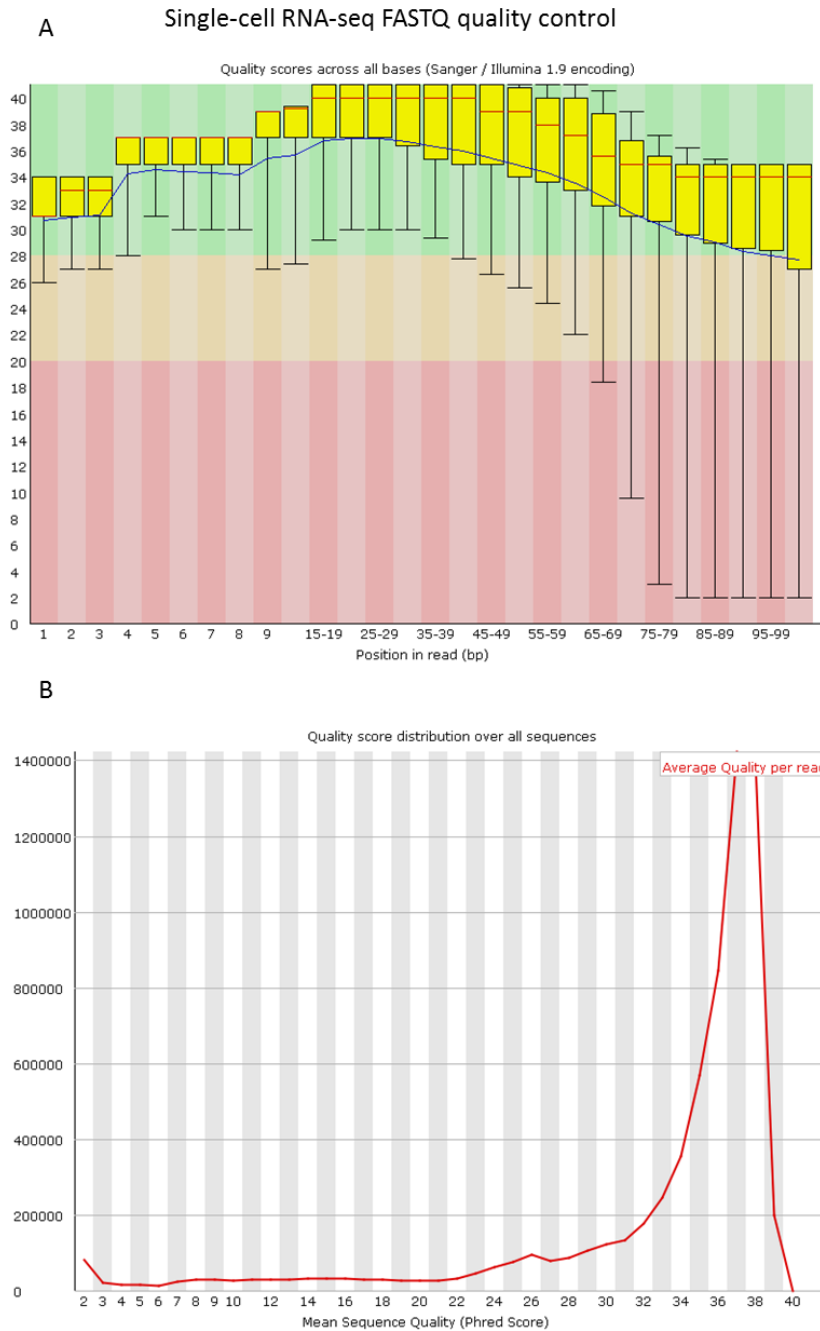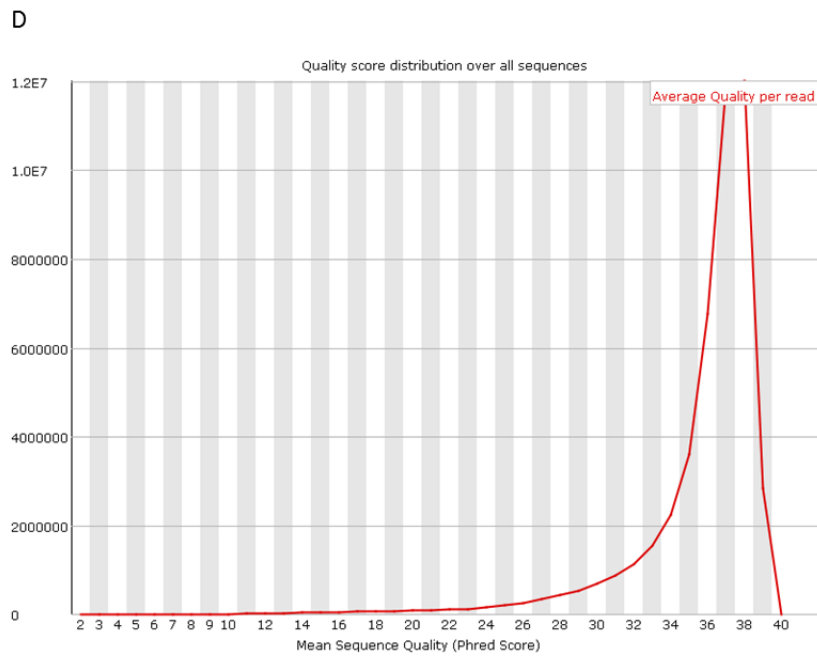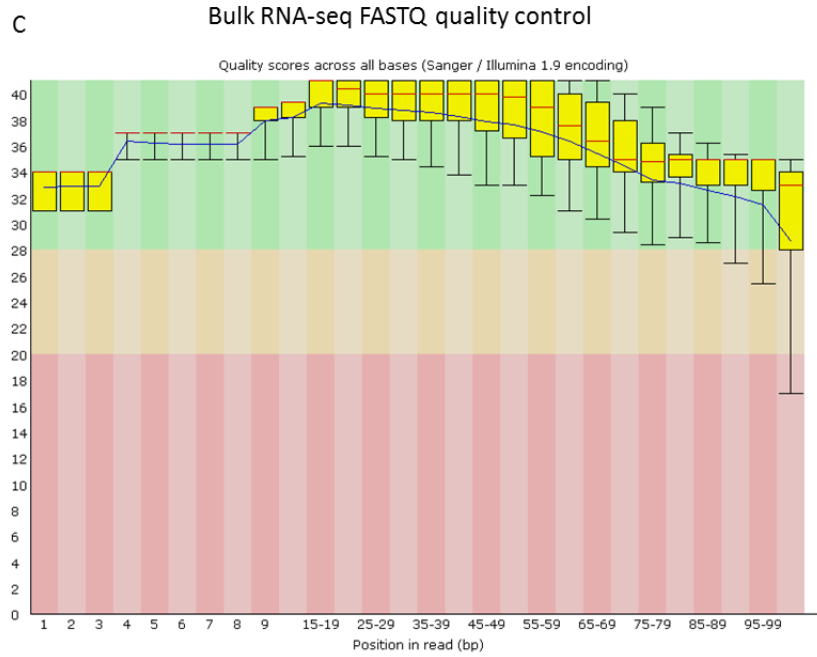
Supplementary Figure 8 Mapping statistics for bulk RNA sequencing reads.
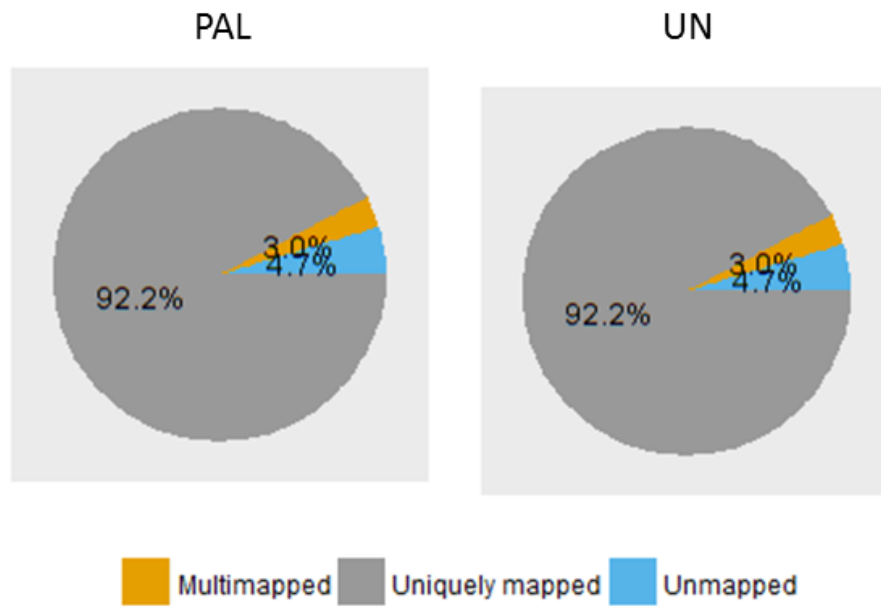
Supplementary Figure 9 Comparison of different read normalization strategies represented in ICA coordinates for palmitate-stimulated and unstimulated cells.
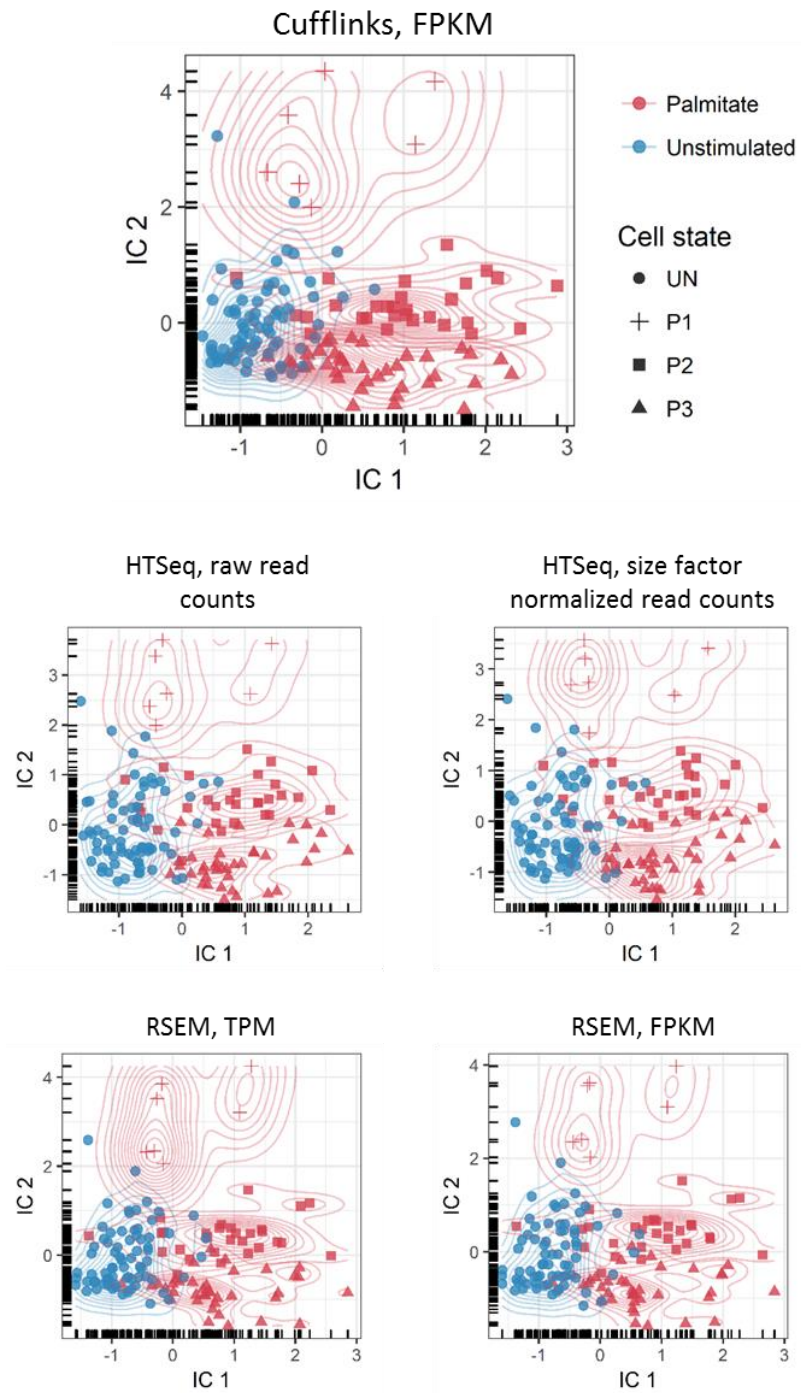
Supplementary Figure 10 Independent Component Analysis (ICA) based on different selected genes.

All genes, mean expression > 50 FPKM (N genes=880)
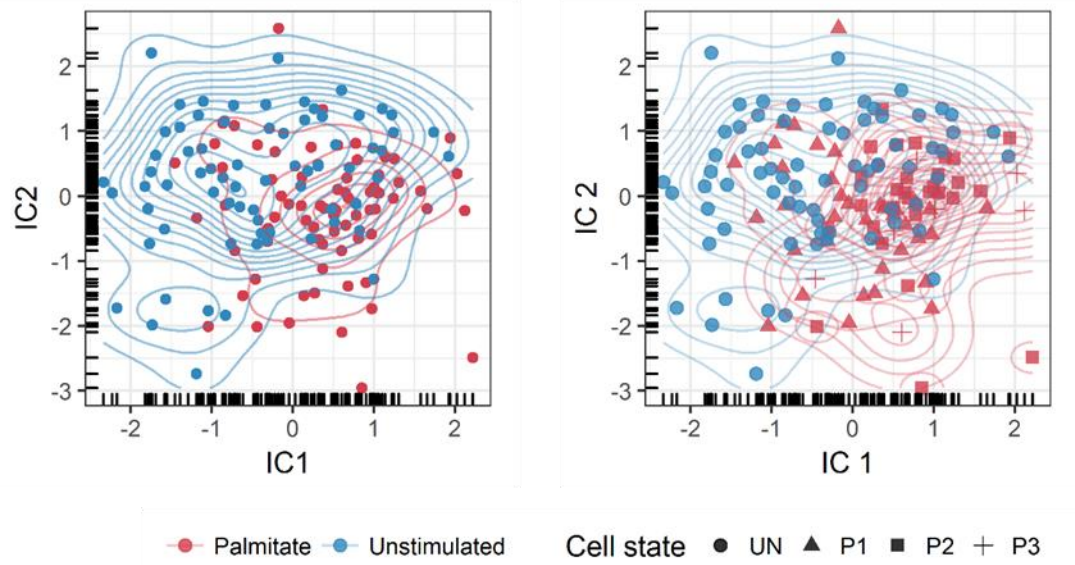
Top 500 highly variable genes
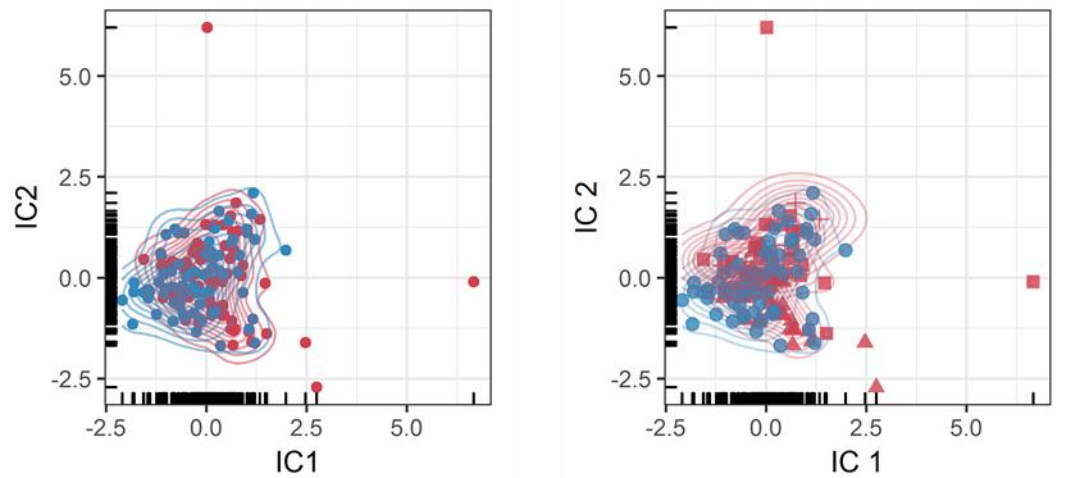
Supplementary Figure 11 Principal Component Analysis (PCA) of individual cells based on palmitate-induced genes.
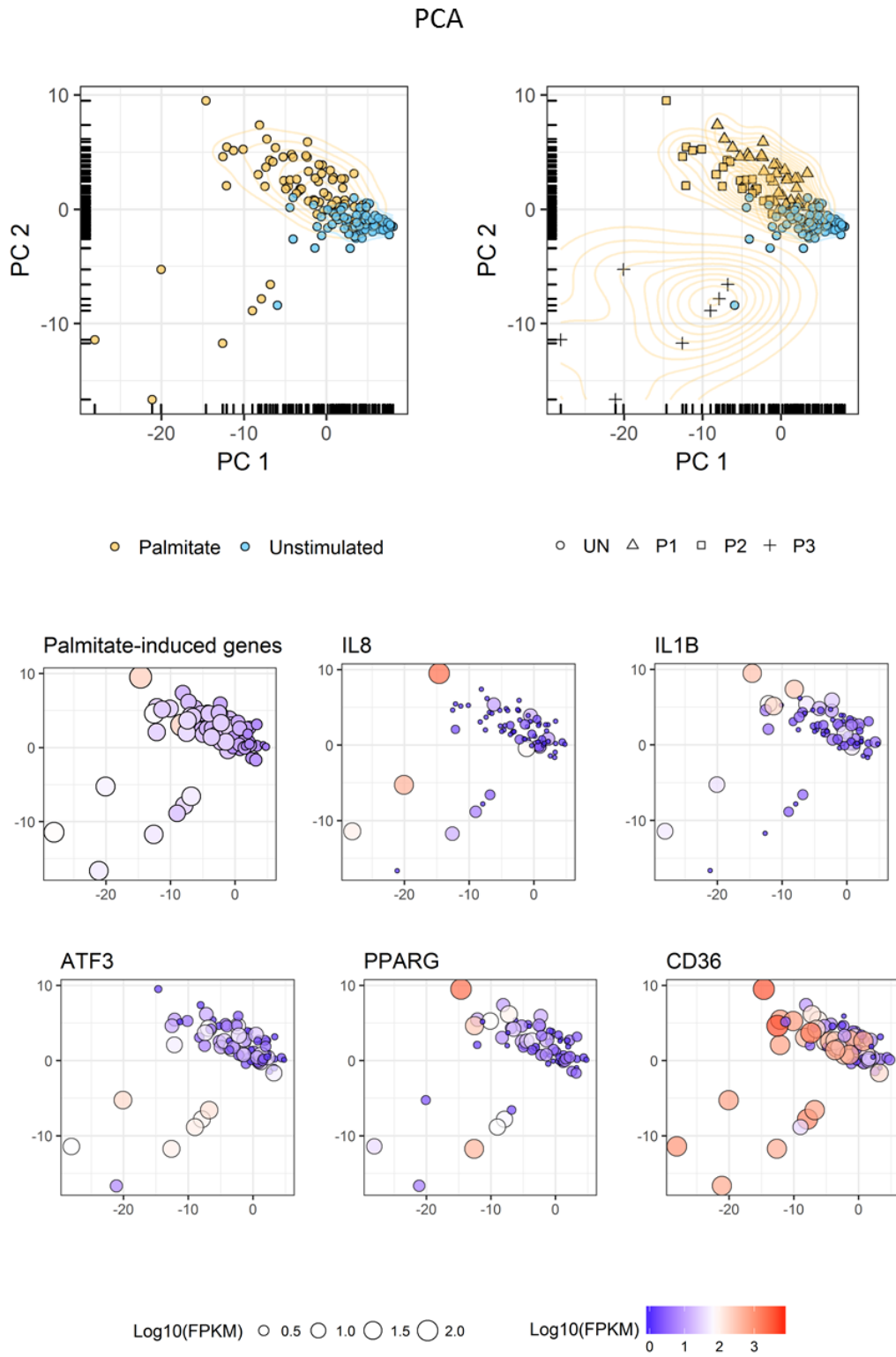
Supplementary Figure 12 tSNE analysis of individual cells based on palmitate-induced genes.
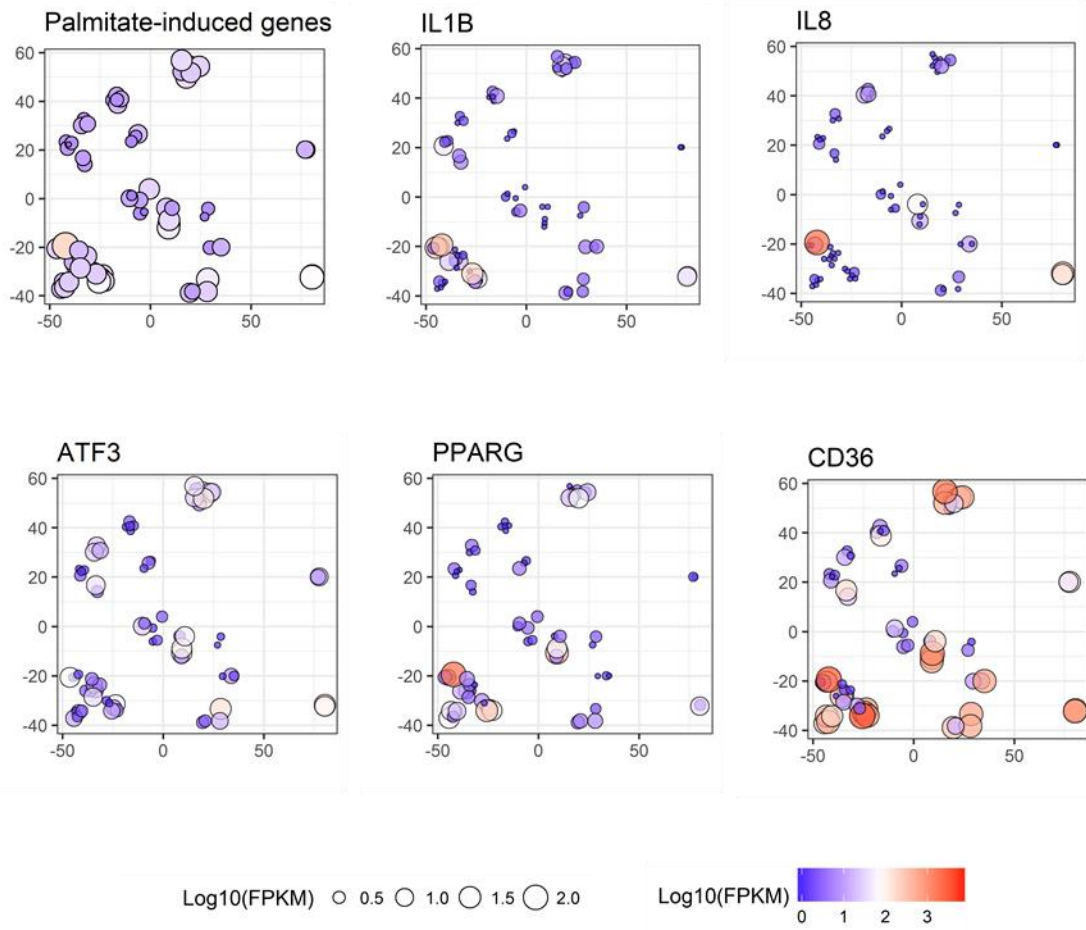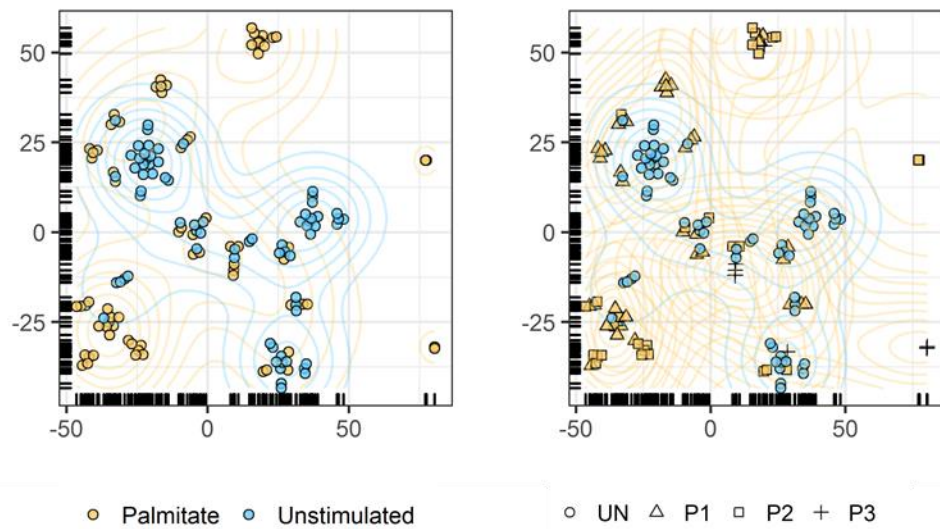
Supplementary Figure 13 96-well plate and Fluidigm C1 IFC layout reconstruction with identified cell transcriptional states.

No technical bias related to well position was observed to potentially influence cell transcriptional state identity.

	1	2	3	4	5	6	7	8	9	10	11	12
A	C03	C02	C01	C49	C50	C51	C06	C05	C04	C52	C53	C54
B	C09	C08	C07	C55	C56	C57	C12	C11	C10	C58	C59	C60
C	C15	C14	C13	C61	C62	C63	C18	C17	C16	C64	C65	C66
D	C21	C20	C19	C67	C68	C69	C24	C23	C22	C70	C71	C72
E	C25	C26	C27	C75	C74	C73	C28	C29	C30	C78	C77	C76
F	C31	C32	C33	C81	C80	C79	C34	C35	C36	C84	C83	C82
G	C37	C38	C39	C87	C86	C85	C40	C41	C42	C90	C89	C88
H	C43	C44	C45	C93	C92	C91	C46	C47	C48	C96	C95	C94

|			
C01	C49	C25	C73
C02	C50	C26	C74
C03	C51	C27	C75
C04	C52	C28	C76
C05	C53	C29	C77
C06	C54	C30	C78
C07	C55	C31	C79
C08	C56	C32	C80
C09	C57	C33	C81
C10	C58	C34	C82
C11	C59	C35	C83
C12	C60	C36	C84
C13	C61	C37	C85
C14	C62	C38	C86
C15	C63	C39	C87
C16	C64	C40	C88
C17	C65	C41	C89
C18	C66	C42	C90
C19	C67	C43	C91
C20	C68	C44	C92
C21	C69	C45	C93
C22	C70	C46	C94
C23	C71	C47	C95
C24	C72	C48	C96
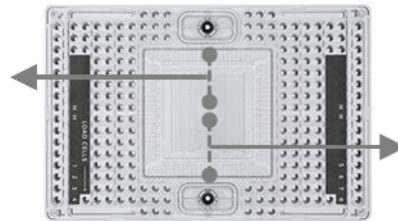
Legend:
- Filtered out
- P1 cell state
- P2 cell state
- P3 cell state

Supplementary Figure 14 Expression of selected transcription factors in individual cells (ICA coordinates) and cell states.

Gene module I
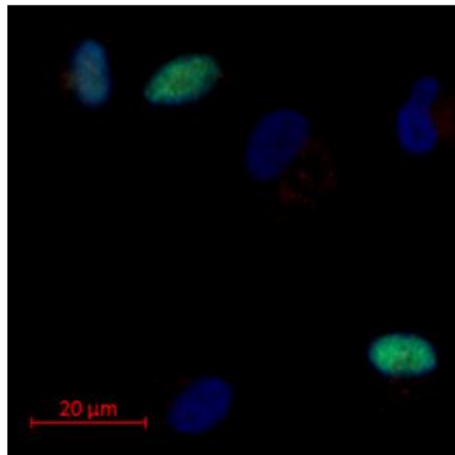

Gene module II

Gene module III

Gene module IV

Gene module V
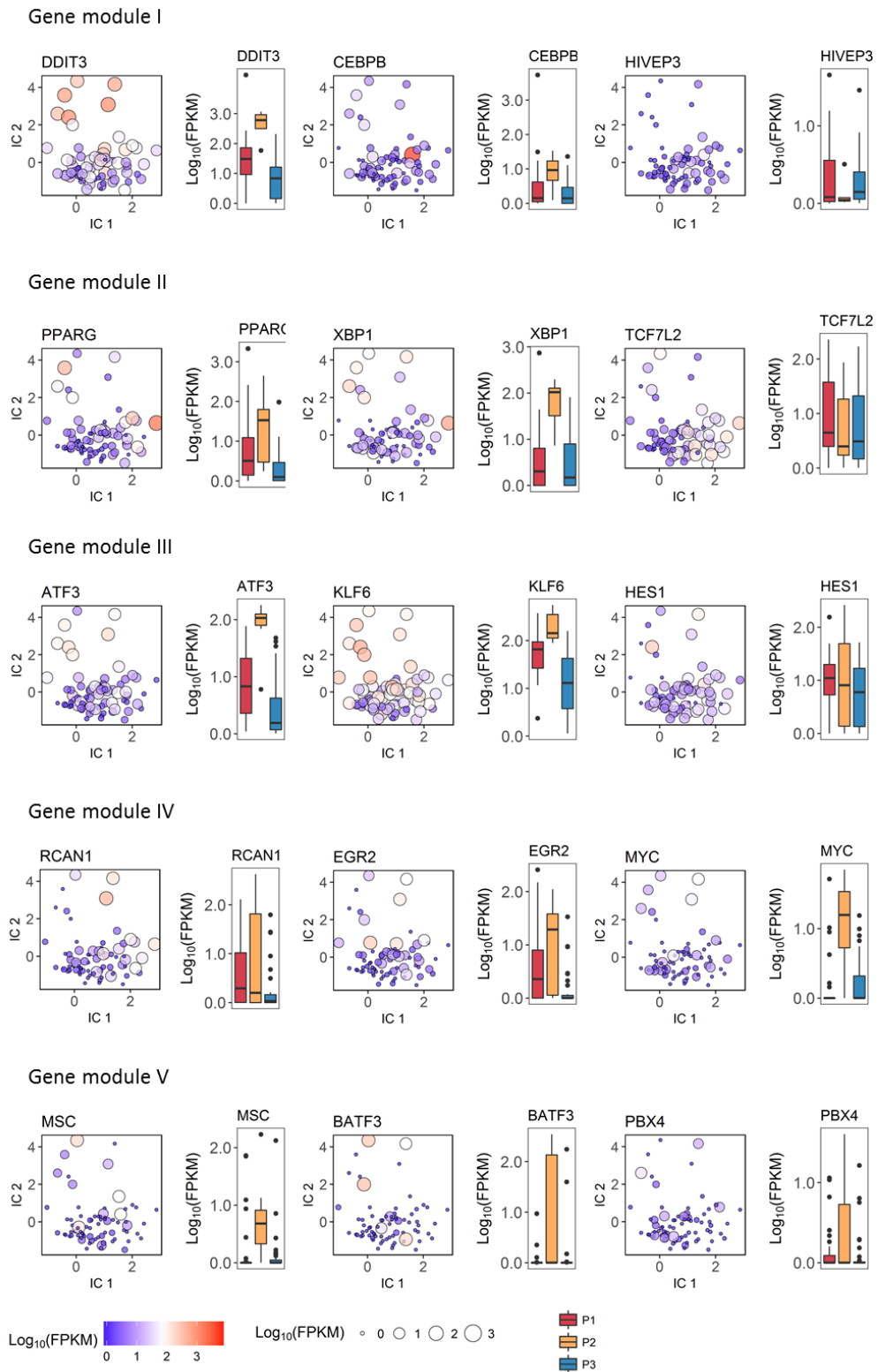
Supplementary Figure 15 Generation of extended depth of focus image from 4 Z-stacked IF image.
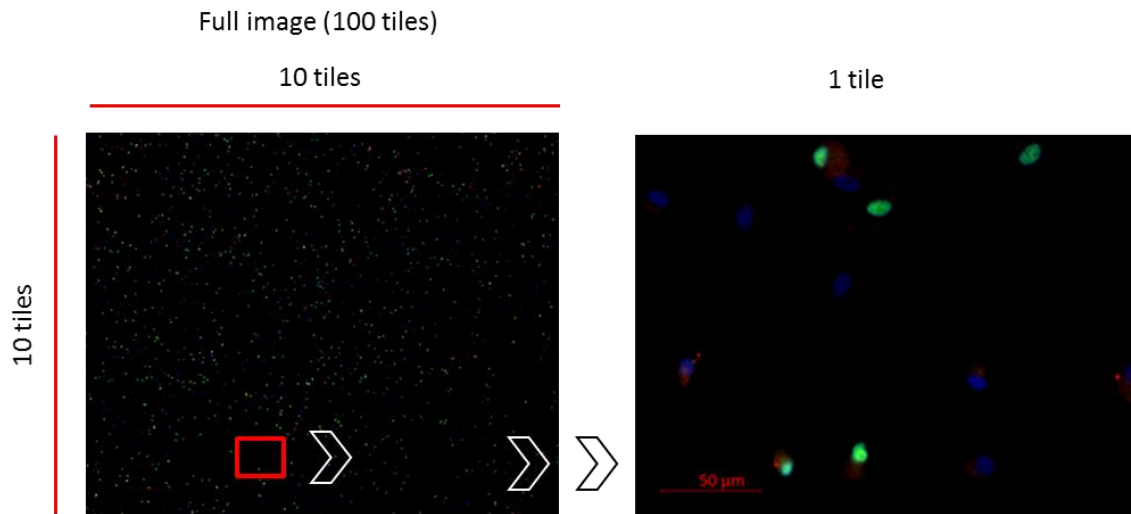
Z-Stack image (4 slices, 4,5µm distance)
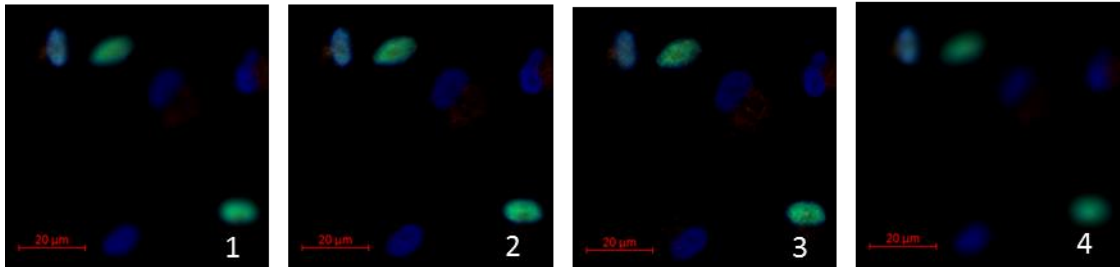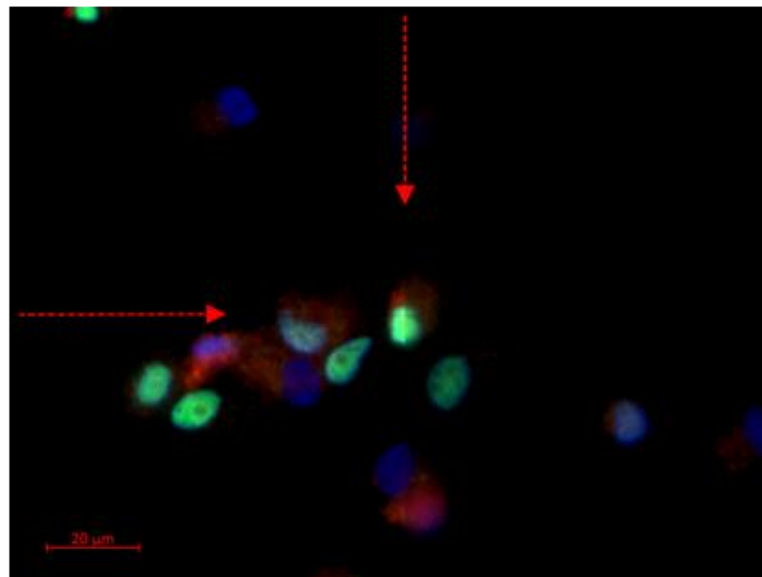

Extended Depth of Focus image

Supplementary Figure 16 Representation of 100-tiled IF image.

**Supplementary Figure 17 IF image of 4 tiles stitching borders.**

Supplementary Figure 18 EBImage-based analysis of IF images.
A-C Nuclei detection, thresholding and labeling (A, B) and watershed transformation-based separation of nuclei including closely located nuclei (C).
**D-I** For cell segmentation, cell borders were firstly defined based on combined unfiltered signal from Alexa 488 and Alexa 595 (D-F). Identified cells were filtered based on surface area, labeled, empty segments inside cell surface were filled (F). Incomplete cells were removed from image borders (G). Cell segmentation was performed using previously defined nuclei as seeds (H, I). Finally, total signal was quantified within defined cell borders for all 3 channels along with other parameters of all detected cells (cell surface area etc.).
Scale – 20 μM
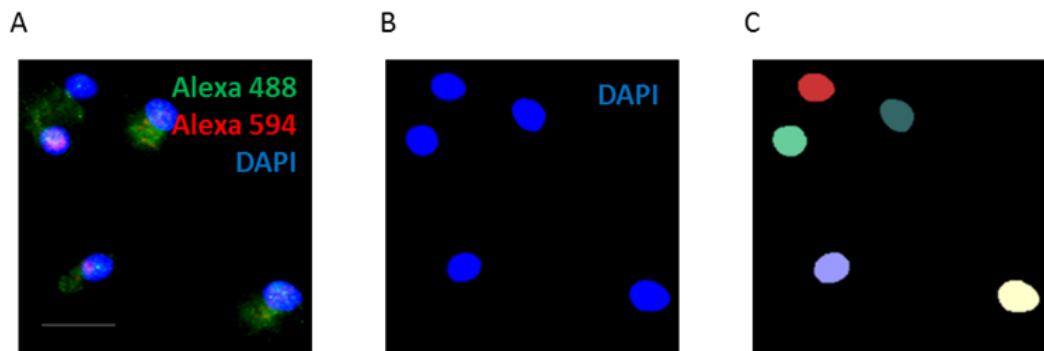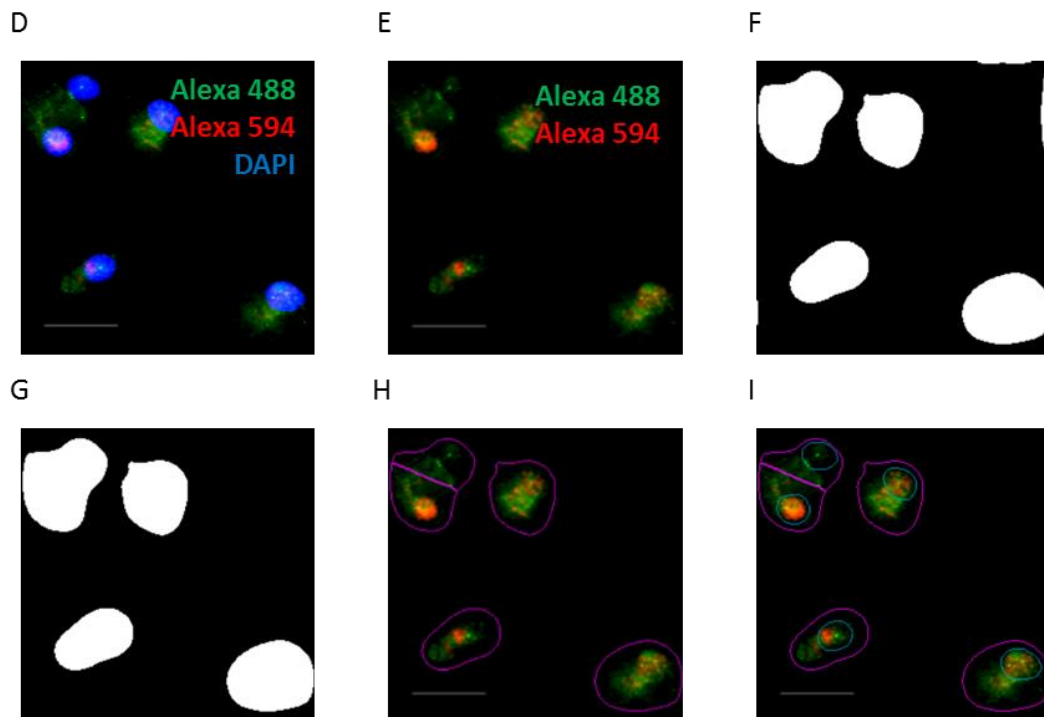
Supplementary Figure 19 Quantification of cell-to cell gene expression variance score.
A Each dot represents a gene. On the scatter plot variance across all palmitate-stimulated and unstimulated single cell versus mean expression for each detected gene is shown. Variance is estimated as a distance between quantified gene variance and generalized linear fit for corresponding expression level.
B Correlation between estimated variance score and gene expression level.
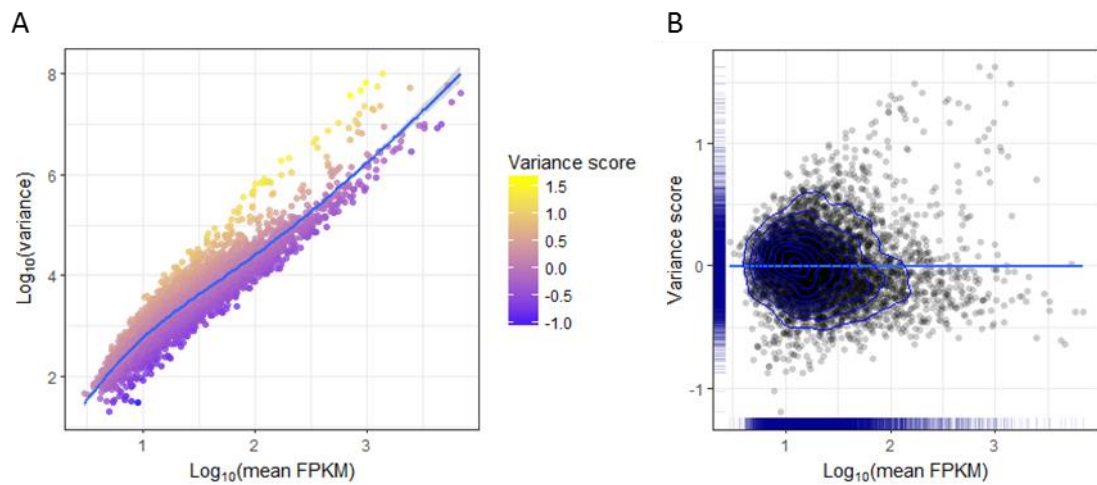
Supplementary Materials

Supplementary Table 1 DAVID gene functional annotation analysis results for palmitate-induced differentially expressed genes.
Enriched pathways with minimum gene count 15 and corrected P-Value lower than 10^{-3} are shown.

Category	Term		Gene count	P-Value	Benjamini-Hochberg corrected P-Value
KEGG Pathway		Cytokine-cytokine receptor interaction	26	1.9E-8	2.0E-6
KEGG Pathway		MAPK signaling pathway	23	7.2E-6	1.6E-4
KEGG Pathway		TNF signaling pathway	22	3.0E-12	7.5E-10
KEGG Pathway		Chemokine signaling pathway	20	2.7E-6	8.5E-5
KEGG Pathway		NF-kappa B signaling pathway	16	3.5E-8	2.6E-6
KEGG Pathway		Rheumatoid arthritis	15	2.9E-7	1.6E-5
KEGG Pathway		Toll-like receptor signaling pathway	15	3.0E-6	8.1E-5

Supplementary Table 2 Assignment of palmitate-induced genes to gene co-expression modules with computed connectivity based on weighted gene co-expression network analysis.

Gene	Gene module	Cell state	Total connectivity	Connectivity within assigned module
CEBPB	I	P2	3.7297	3.7293
DDIT3	I	P2	3.6967	3.6958
DENND3	I	P2	0.0028	0.0005
GPRC5A	I	P2	1.8608	1.8600
HBEGF	I	P2	1.5432	1.5414
HIVEP3	I	P2	0.4362	0.4360
KCNN4	I	P2	1.1305	1.1304
KIAA0020	I	P2	0.0156	0.0144
PLAUR	I	P2	0.5766	0.4561
RGCC	I	P2	0.6355	0.6354
RRP12	I	P2	0.0293	0.0293
TLR2	I	P2	0.0029	0.0021
TNFRSF10B	I	P2	3.6888	3.6884
TPM4	I	P2	1.1873	1.1871
WT1	I	P2	1.0566	1.0566
ZCCHC14	I	P2	0.1072	0.1066
ACSL1	II	P2	0.0118	0.0062
AMPD3	II	P2	0.0314	0.0279
ARAP3	II	P2	0.0004	0.0000
C5AR1	II	P2	4.4135	4.3763
CCL20	II	P2	7.6831	7.6768
CD36	II	P2	0.1208	0.0772
CD40	II	P2	5.6293	5.6256
DUSP1	II	P2	0.5052	0.4720
EHD1	II	P2	0.0209	0.0207
FFAR2	II	P2	8.0006	7.9927
FHOD1	II	P2	4.1079	4.1052
FLOT1	II	P2	0.2759	0.2704
G0S2	II	P2	0.0168	0.0163
GFPT1	II	P2	0.2855	0.2508

GPR84	II	P2	0.0043	0.0039
IL1β	II	P2	0.2614	0.2605
IL32	II	P2	2.6352	2.6323
IL8	II	P2	7.2064	7.1983
ISG20	II	P2	0.0106	0.0095
IVNS1ABP	II	P2	3.3772	3.3707
LFNG	II	P2	7.4028	7.3899
MAP1B	II	P2	0.2337	0.1622
MAP2K3	II	P2	6.7136	6.6934
NCF1	II	P2	0.0167	0.0130
NRIP3	II	P2	0.2327	0.2298
OPTN	II	P2	0.0118	0.0110
PDGFA	II	P2	0.0036	0.0016
PHC2	II	P2	2.6650	2.6632
PLIN2	II	P2	3.6933	3.6760
PPARG	II	P2	6.6337	6.6278
RAI14	II	P2	0.0609	0.0488
RGS1	II	P2	0.0729	0.0716
RGS16	II	P2	0.0439	0.0409
RHOB	II	P2	2.3575	2.3554
S100A10	II	P2	0.2863	0.2696
SCD	II	P2	0.1169	0.1003
SH3RF1	II	P2	0.0366	0.0329
SLAMF8	II	P2	0.3537	0.3375
SLC20A1	II	P2	0.0182	0.0153
SLC43A3	II	P2	0.0612	0.0471
SNAI1	II	P2	0.1999	0.1918
SPOCD1	II	P2	0.0104	0.0099
STARD4	II	P2	0.0879	0.0553
TCF7L2	II	P2	0.0457	0.0446
UBALD2	II	P2	0.0884	0.0618
XBP1	II	P2	4.4599	4.4542
ZFYVE28	II	P2	4.6444	4.6405
ATF3	III	P3	3.3363	3.3322
CADPS2	III	P3	1.2169	1.2001
CD44	III	P3	0.6351	0.6327
CKAP4	III	P3	0.6118	0.5933

CRELD2	III	P3	0.6100	0.5680
DERL3	III	P3	0.5313	0.5277
DNAJB9	III	P3	0.5079	0.4952
HES1	III	P3	0.2271	0.2216
IER2	III	P3	0.1801	0.1799
KLF6	III	P3	0.1882	0.1674
MMP19	III	P3	0.1359	0.1337
NME1-NME2	III	P3	0.1001	0.0931
PHLDA1	III	P3	0.0891	0.0856
RASGEF1B	III	P3	0.0659	0.0409
SERPINE1	III	P3	0.0161	0.0160
STK10	III	P3	0.0064	0.0045
TFAP2A	III	P3	0.0066	0.0045
VASP	III	P3	0.0010	0.0005
ASNS	IV	P3	3.5759	3.5733
BHLHE40	IV	P3	1.5855	1.5733
BIRC3	IV	P3	1.4295	1.3951
CCL3	IV	P3	0.9832	0.9568
CCL3L3	IV	P3	0.9785	0.9393
CCL4	IV	P3	0.8420	0.8320
DUSP2	IV	P3	0.4711	0.4572
EGR1	IV	P3	0.3356	0.3315
EGR2	IV	P3	0.3320	0.3311
FAM129B	IV	P3	0.3399	0.3184
HDAC7	IV	P3	0.2574	0.2320
HMGCS1	IV	P3	0.2241	0.2174
HS3ST3A1	IV	P3	0.2323	0.2153
HSD17B7	IV	P3	0.2097	0.2069
ICAM1	IV	P3	0.1963	0.1803
LDLR	IV	P3	0.1583	0.1554
MAFF	IV	P3	0.1731	0.1504
MSMO1	IV	P3	0.1272	0.1112
MYC	IV	P3	0.1281	0.1075
NAMPT	IV	P3	0.0978	0.0959
PER2	IV	P3	0.1025	0.0890
PIM1	IV	P3	0.0774	0.0727

RCAN1	IV	P3	0.0431	0.0393
SESN2	IV	P3	0.0164	0.0155
SGK1	IV	P3	0.0251	0.0144
SH2B3	IV	P3	0.0138	0.0133
SHISA2	IV	P3	0.0150	0.0116
SNX9	IV	P3	0.0050	0.0049
SQLE	IV	P3	0.0056	0.0045
TNFAIP3	IV	P3	0.0030	0.0029
TNFAIP6	IV	P3	0.0054	0.0028
TNFRSF10D	IV	P3	0.0025	0.0020
AEN	V	P3	3.9781	3.9730
AK4	V	P3	3.6924	3.6891
BAG3	V	P3	2.7483	2.7413
BATF3	V	P3	2.4360	2.4299
CBLB	V	P3	1.1804	1.1667
CBWD6	V	P3	1.1272	1.1150
CCL18	V	P3	1.0224	1.0022
CCR7	V	P3	0.8664	0.8222
CD300A	V	P3	0.6500	0.6494
CSF1	V	P3	0.5665	0.5635
DUSP5	V	P3	0.3590	0.3406
EMP1	V	P3	0.3277	0.3196
FKBP14	V	P3	0.3493	0.3004
GDF15	V	P3	0.2492	0.2444
HSPA1A	V	P3	0.1907	0.1885
IL23A	V	P3	0.1799	0.1796
KCNQ4	V	P3	0.1759	0.1756
MEI1	V	P3	0.1812	0.1346
MSC	V	P3	0.1425	0.1322
MST1	V	P3	0.1251	0.1082
MYO10	V	P3	0.1194	0.1023
PBX4	V	P3	0.0956	0.0920
PER1	V	P3	0.1024	0.0897
PIM3	V	P3	0.0689	0.0683
PLEK2	V	P3	0.0753	0.0629
PLK3	V	P3	0.0568	0.0504
PPP1R15A	V	P3	0.0478	0.0473

PSAT1	V	P3	0.0430	0.0430
RHBDF2	V	P3	0.0918	0.0319
RRP9	V	P3	0.0304	0.0208
SAPCD1	V	P3	0.0170	0.0164
SHB	V	P3	0.0171	0.0129
SLC17A9	V	P3	0.0128	0.0113
SLC2A1	V	P3	0.0224	0.0100
SLC39A14	V	P3	0.0163	0.0093
SLC7A11	V	P3	0.0279	0.0086
TMEM135	V	P3	0.0030	0.0029
TRIB3	V	P3	0.0013	0.0011
TRIM16L	V	P3	0.0008	0.0008
TULP3	V	P3	0.0007	0.0006
ZFAND2A	V	P3	0.0005	0.0003

7.2 Abbreviations

Abbreviation	Full term
7-AAD	7-Aminoactinomycin D
ATM	Adipose tissue macrophage
BMI	Body mass index
BSA	Bovine Serum Albumin
CV	Coefficient of variation
CVD	Cardiovascular disease
DAG	Diacylglycerol
DAMP	Damage-associated molecular patterns
DE	Differential expression
DHA	Docosahexanoic acid
DM	Distance to median
EPA	Eicosapentanoic acid
ER	Endoplasmatic reticulum
ERCC	External RNA control consortium
FATP	Fatty acid transport proteins
FBS	Fetal bovine serum
FetA	fetuin A
FFA	Free fatty acid
HFD	High fat diet
ICA	Independent component analysis
IF	Immunofluorescence
IFC	Integrated fluidic circuit
IFD	International diabetes federation
IPC	Interplate calibrator
KC	Kupfer cell
LpL	Lipoprotein lipase
LPS	Lipopolysacharide
NAFLD	Non-alcoholic fatty liver disease
NEFA	Nonesterified fatty acids
NK	Natural killer cell
nPKC	Novel protein kinase C
PBMC	Peripheral blood mononuclear cells
PBS	Dulbecco's phosphate buffered saline
PCR	Polymerase chain reaction

PKC	Protein kinase C
PMA	Phorbol 12-myristate 13-acetate
RHM	Recruited hepatic macrophage
RT	Reverse transcription
T2D	Type 2 diabetes
TAM	Tumor associated macrophage
Th1, Th2	T helper cell 1, T helper cell2
TLR	Toll-like receptor
TOM	Topological overlap matrix
TZD	Thiazolidinediones
UPR	Unfolded protein response
WAT	White adipose tissue
WGCNA	Weighted gene co-expression network analysis
WT	Wild type

7.3 List of figures and tables

7.3.1 List of figures

7.3.2 List of supplementary figures

7.3.3 List of tables

7.3.4 List of supplementary tables

8 References

1.   McNelis, J.C. and J.M. Olefsky, *Macrophages, immunity, and metabolic disease.* Immunity, 2014. **41**(1): p. 36-48.
2.   *IDF diabetes atlas - 7th edition*. Internatioanl diabetes federation
3.   Tuomilehto, J. and S. Bahijri, *Epidemiology: Lifetime risk of diabetes mellitus--how high?* Nat Rev Endocrinol, 2016. **12**(3): p. 127-8.
4.   Fuchsberger, C., et al., *The genetic architecture of type 2 diabetes.* Nature, 2016. **536**(7614): p. 41-7.
5.   Locke, A.E., et al., *Genetic studies of body mass index yield new insights for obesity biology.* Nature, 2015. **518**(7538): p. 197-206.
6.   Lumeng, C.N. and A.R. Saltiel, *Inflammatory links between obesity and metabolic disease.* J Clin Invest, 2011. **121**(6): p. 2111-7.
7.   Olefsky, J.M. and C.K. Glass, *Macrophages, inflammation, and insulin resistance.* Annu Rev Physiol, 2010. **72**: p. 219-46.
8.   Hotamisligil, G.S., N.S. Shargill, and B.M. Spiegelman, *Adipose expression of tumor necrosis factor-alpha: direct role in obesity-linked insulin resistance.* Science, 1993. **259**(5091): p. 87-91.
9.   Weisberg, S.P., et al., *Obesity is associated with macrophage accumulation in adipose tissue.* J Clin Invest, 2003. **112**(12): p. 1796-808.
10.   Spite, M., et al., *Deficiency of the leukotriene B4 receptor, BLT-1, protects against systemic insulin resistance in diet-induced obesity.* J Immunol, 2011. **187**(4): p. 1942-9.
11.   Mothe-Satney, I., et al., *Adipocytes secrete leukotrienes: contribution to obesity-associated inflammation and insulin resistance in mice.* Diabetes, 2012. **61**(9): p. 2311-9.
12.   Chen, A., et al., *Diet induction of monocyte chemoattractant protein-1 and its impact on obesity.* Obes Res, 2005. **13**(8): p. 1311-20.
13.   Weisberg, S.P., et al., *CCR2 modulates inflammatory and metabolic effects of high-fat feeding.* J Clin Invest, 2006. **116**(1): p. 115-24.
14.   Randolph, G.J., *Emigration of monocyte-derived cells to lymph nodes during resolution of inflammation and its failure in atherosclerosis.* Curr Opin Lipidol, 2008. **19**(5): p. 462-8.
15.   McLaughlin, T., et al., *T-cell profile in adipose tissue is associated with insulin resistance and systemic inflammation in humans.* Arterioscler Thromb Vasc Biol, 2014. **34**(12): p. 2637-43.
16.   Winer, D.A., et al., *B Lymphocytes in obesity-related adipose tissue inflammation and insulin resistance.* Cell Mol Life Sci, 2014. **71**(6): p. 1033-43.
17.   Liu, J., et al., *Genetic deficiency and pharmacological stabilization of mast cells reduce diet-induced obesity and diabetes in mice.* Nat Med, 2009. **15**(8): p. 940-5.
18.   Talukdar, S., et al., *Neutrophils mediate insulin resistance in mice fed a high-fat diet through secreted elastase.* Nat Med, 2012. **18**(9): p. 1407-12.
19.   Wu, D., et al., *Eosinophils sustain adipose alternatively activated macrophages associated with glucose homeostasis.* Science, 2011. **332**(6026): p. 243-7.
20.   Devisscher, L., et al., *The role of macrophages in obesity-driven chronic liver disease.* J Leukoc Biol, 2016. **99**(5): p. 693-8.
21.   Fink, L.N., et al., *Expression of anti-inflammatory macrophage genes within skeletal muscle correlates with insulin sensitivity in human obesity and type 2 diabetes.* Diabetologia, 2013. **56**(7): p. 1623-8.
22.   Fink, L.N., et al., *Pro-inflammatory macrophages increase in skeletal muscle of high fat-fed mice and correlate with metabolic risk markers in humans.* Obesity (Silver Spring), 2014. **22**(3): p. 747-57.
23.   Tugal, D., X. Liao, and M.K. Jain, *Transcriptional control of macrophage polarization.* Arterioscler Thromb Vasc Biol, 2013. **33**(6): p. 1135-44.
24.   Lawrence, T. and G. Natoli, *Transcriptional regulation of macrophage polarization: enabling diversity with identity.* Nat Rev Immunol, 2011. **11**(11): p. 750-61.
25.   Gordon, S., *Alternative activation of macrophages.* Nat Rev Immunol, 2003. **3**(1): p. 23-35.

References

26. Gordon, S. and F.O. Martinez, *Alternative activation of macrophages: mechanism and functions.* Immunity, 2010. **32**(5): p. 593-604.

27. Chistiakov, D.A., Y.V. Bobryshev, and A.N. Orekhov, *Changes in transcriptome of macrophages in atherosclerosis.* J Cell Mol Med, 2015. **19**(6): p. 1163-73.

28. Ferrante, C.J. and S.J. Leibovich, *Regulation of Macrophage Polarization and Wound Healing.* Adv Wound Care (New Rochelle), 2012. **1**(1): p. 10-16.

29. Mosser, D.M. and J.P. Edwards, *Exploring the full spectrum of macrophage activation.* Nat Rev Immunol, 2008. **8**(12): p. 958-69.

30. Martinez, F.O. and S. Gordon, *The M1 and M2 paradigm of macrophage activation: time for reassessment.* F1000Prime Rep, 2014. **6**: p. 13.

31. Murray, P.J., et al., *Macrophage activation and polarization: nomenclature and experimental guidelines.* Immunity, 2014. **41**(1): p. 14-20.

32. Sica, A. and A. Mantovani, *Macrophage plasticity and polarization: in vivo veritas.* J Clin Invest, 2012. **122**(3): p. 787-95.

33. May, R.D. and M. Fung, *Strategies targeting the IL-4/IL-13 axes in disease.* Cytokine, 2015. **75**(1): p. 89-116.

34. Mueller, T.D., et al., *Structure, binding, and antagonists in the IL-4/IL-13 receptor system.* Biochim Biophys Acta, 2002. **1592**(3): p. 237-50.

35. Stone, K.D., C. Prussin, and D.D. Metcalfe, *IgE, mast cells, basophils, and eosinophils.* J Allergy Clin Immunol, 2010. **125**(2 Suppl 2): p. S73-80.

36. Novak, M.L. and T.J. Koh, *Macrophage phenotypes during tissue repair.* J Leukoc Biol, 2013. **93**(6): p. 875-81.

37. Lee, C.G., et al., *Role of chitin and chitinase/chitinase-like proteins in inflammation, tissue remodeling, and injury.* Annu Rev Physiol, 2011. **73**: p. 479-501.

38. Lumeng, C.N., et al., *Increased inflammatory properties of adipose tissue macrophages recruited during diet-induced obesity.* Diabetes, 2007. **56**(1): p. 16-23.

39. Patsouris, D., et al., *Ablation of CD11c-positive cells normalizes insulin sensitivity in obese insulin resistant animals.* Cell Metab, 2008. **8**(4): p. 301-9.

40. Robbins, G.R., H. Wen, and J.P. Ting, *Inflammasomes and metabolic disorders: old genes in modern diseases.* Mol Cell, 2014. **54**(2): p. 297-308.

41. Kanneganti, T.D. and V.D. Dixit, *Immunological complications of obesity.* Nat Immunol, 2012. **13**(8): p. 707-12.

42. Roden, M., et al., *Mechanism of free fatty acid-induced insulin resistance in humans.* J Clin Invest, 1996. **97**(12): p. 2859-65.

43. Staehr, P., et al., *Effects of free fatty acids per se on glucose production, gluconeogenesis, and glycogenolysis.* Diabetes, 2003. **52**(2): p. 260-7.

44. Jocken, J.W., et al., *Adipose triglyceride lipase and hormone-sensitive lipase protein expression is decreased in the obese insulin-resistant state.* J Clin Endocrinol Metab, 2007. **92**(6): p. 2292-9.

45. Langin, D., et al., *Adipocyte lipases and defect of lipolysis in human obesity.* Diabetes, 2005. **54**(11): p. 3190-7.

46. Shi, H., et al., *TLR4 links innate immunity and fatty acid-induced insulin resistance.* J Clin Invest, 2006. **116**(11): p. 3015-25.

47. Lee, J.Y., et al., *Saturated fatty acids, but not unsaturated fatty acids, induce the expression of cyclooxygenase-2 mediated through Toll-like receptor 4.* J Biol Chem, 2001. **276**(20): p. 16683-9.

48. Institute, N.C., *Risk Factor Monitoring and Methods: Table 1. Top Food Sources of Saturated Fats among U.S. Population, 2005-2006 NHANES.*

49. D'Eliseo, D. and F. Velotti, *Omega-3 Fatty Acids and Cancer Cell Cytotoxicity: Implications for Multi-Targeted Cancer Therapy.* J Clin Med, 2016. **5**(2).

50. Spencer, M., et al., *Omega-3 fatty acids reduce adipose tissue macrophages in human subjects with insulin resistance.* Diabetes, 2013. **62**(5): p. 1709-17.

51. Yan, Y., et al., *Omega-3 fatty acids prevent inflammation and metabolic disorder through inhibition of NLRP3 inflammasome activation.* Immunity, 2013. **38**(6): p. 1154-63.

References

52.   Harris, W.S., et al., *Towards establishing dietary reference intakes for eicosapentaenoic and docosahexaenoic acids.* J Nutr, 2009. **139**(4): p. 804S-19S.

53.   Barberger-Gateau, P., et al., *Fish, meat, and risk of dementia: cohort study.* BMJ, 2002. **325**(7370): p. 932-3.

54.   Blad, C.C., C. Tang, and S. Offermanns, *G protein-coupled receptors for energy metabolites as new therapeutic targets.* Nat Rev Drug Discov, 2012. **11**(8): p. 603-19.

55.   Oh, D.Y. and W.S. Lagakos, *The role of G-protein-coupled receptors in mediating the effect of fatty acids on inflammation and insulin sensitivity.* Curr Opin Clin Nutr Metab Care, 2011. **14**(4): p. 322-7.

56.   Oh, D.Y., et al., *GPR120 is an omega-3 fatty acid receptor mediating potent anti-inflammatory and insulin-sensitizing effects.* Cell, 2010. **142**(5): p. 687-98.

57.   Oh, D.Y., et al., *A Gpr120-selective agonist improves insulin resistance and chronic inflammation in obese mice.* Nat Med, 2014. **20**(8): p. 942-7.

58.   Lackey, D.E. and J.M. Olefsky, *Regulation of metabolism by the innate immune system.* Nat Rev Endocrinol, 2016. **12**(1): p. 15-28.

59.   Samuel, V.T. and G.I. Shulman, *Mechanisms for insulin resistance: common threads and missing links.* Cell, 2012. **148**(5): p. 852-71.

60.   Goudriaan, J.R., et al., *CD36 deficiency increases insulin sensitivity in muscle, but induces insulin resistance in the liver in mice.* J Lipid Res, 2003. **44**(12): p. 2270-7.

61.   Wang, H., et al., *Skeletal muscle-specific deletion of lipoprotein lipase enhances insulin signaling in skeletal muscle but causes insulin resistance in liver and other tissues.* Diabetes, 2009. **58**(1): p. 116-24.

62.   Falcon, A., et al., *FATP2 is a hepatic fatty acid transporter and peroxisomal very long-chain acyl-CoA synthetase.* Am J Physiol Endocrinol Metab, 2010. **299**(3): p. E384-93.

63.   Magkos, F., et al., *Intrahepatic diacylglycerol content is associated with hepatic insulin resistance in obese subjects.* Gastroenterology, 2012. **142**(7): p. 1444-6 e2.

64.   Fabbrini, E., et al., *Intrahepatic fat, not visceral fat, is linked with metabolic complications of obesity.* Proc Natl Acad Sci U S A, 2009. **106**(36): p. 15430-5.

65.   Itani, S.I., et al., *Lipid-induced insulin resistance in human muscle is associated with changes in diacylglycerol, protein kinase C, and IkappaB-alpha.* Diabetes, 2002. **51**(7): p. 2005-11.

66.   Szendroedi, J., et al., *Role of diacylglycerol activation of PKCtheta in lipid-induced muscle insulin resistance in humans.* Proc Natl Acad Sci U S A, 2014. **111**(26): p. 9597-602.

67.   Kim, J.K., et al., *PKC-theta knockout mice are protected from fat-induced insulin resistance.* J Clin Invest, 2004. **114**(6): p. 823-7.

68.   Lam, T.K., et al., *Free fatty acid-induced hepatic insulin resistance: a potential role for protein kinase C-delta.* Am J Physiol Endocrinol Metab, 2002. **283**(4): p. E682-91.

69.   Raddatz, K., et al., *Time-dependent effects of Prkce deletion on glucose homeostasis and hepatic lipid metabolism on dietary lipid oversupply in mice.* Diabetologia, 2011. **54**(6): p. 1447-56.

70.   Wen, H., et al., *Fatty acid-induced NLRP3-ASC inflammasome activation interferes with insulin signaling.* Nat Immunol, 2011. **12**(5): p. 408-15.

71.   Vandanmagsar, B., et al., *The NLRP3 inflammasome instigates obesity-induced inflammation and insulin resistance.* Nat Med, 2011. **17**(2): p. 179-88.

72.   Hotamisligil, G.S., *Endoplasmic reticulum stress and the inflammatory basis of metabolic disease.* Cell, 2010. **140**(6): p. 900-17.

73.   Li, Y., et al., *Free cholesterol-loaded macrophages are an abundant source of tumor necrosis factor-alpha and interleukin-6: model of NF-kappaB- and map kinase-dependent inflammation in advanced atherosclerosis.* J Biol Chem, 2005. **280**(23): p. 21763-72.

74.   Ozcan, U., et al., *Endoplasmic reticulum stress links obesity, insulin action, and type 2 diabetes.* Science, 2004. **306**(5695): p. 457-61.

75.   Li, P., et al., *LTB4 promotes insulin resistance in obese mice by acting on macrophages, hepatocytes and myocytes.* Nat Med, 2015. **21**(3): p. 239-47.

76.   Nakatani, Y., et al., *Involvement of endoplasmic reticulum stress in insulin resistance and diabetes.* J Biol Chem, 2005. **280**(1): p. 847-51.

References

77. Lim, Y.J., et al., *Roles of endoplasmic reticulum stress-mediated apoptosis in M1-polarized macrophages during mycobacterial infections.* Sci Rep, 2016. **6**: p. 37211.

78. Wang, Y., et al., *Role of C/EBP homologous protein (CHOP) and Endoplasmic Reticulum in Asthma Exacerbation by Regulating the IL-4/STAT6/Tfec/IL-4Ralpha Positive Feedback Loop in M2 Macrophages.* J Allergy Clin Immunol, 2017.

79. Suzuki, T., et al., *ER Stress Protein CHOP Mediates Insulin Resistance by Modulating Adipose Tissue Macrophage Polarity.* Cell Rep, 2017. **18**(8): p. 2045-2057.

80. Chou, R.C., et al., *Lipid-cytokine-chemokine cascade drives neutrophil recruitment in a murine model of inflammatory arthritis.* Immunity, 2010. **33**(2): p. 266-78.

81. Subbarao, K., et al., *Role of leukotriene B4 receptors in the development of atherosclerosis: potential mechanisms.* Arterioscler Thromb Vasc Biol, 2004. **24**(2): p. 369-75.

82. Odegaard, J.I., et al., *Macrophage-specific PPARgamma controls alternative activation and improves insulin resistance.* Nature, 2007. **447**(7148): p. 1116-20.

83. Johnson, A.M. and J.M. Olefsky, *The origins and drivers of insulin resistance.* Cell, 2013. **152**(4): p. 673-84.

84. De Nardo, D., et al., *High-density lipoprotein mediates anti-inflammatory reprogramming of macrophages via the transcriptional regulator ATF3.* Nat Immunol, 2014. **15**(2): p. 152-60.

85. Donath, M.Y., *Targeting inflammation in the treatment of type 2 diabetes: time to start.* Nat Rev Drug Discov, 2014. **13**(6): p. 465-76.

86. Rojas, L.B. and M.B. Gomes, *Metformin: an old but still the best treatment for type 2 diabetes.* Diabetol Metab Syndr, 2013. **5**(1): p. 6.

87. Saisho, Y., *Metformin and Inflammation: Its Potential Beyond Glucose-lowering Effect.* Endocr Metab Immune Disord Drug Targets, 2015. **15**(3): p. 196-205.

88. Koh, S.J., et al., *Anti-inflammatory mechanism of metformin and its effects in intestinal inflammation and colitis-associated colon cancer.* J Gastroenterol Hepatol, 2014. **29**(3): p. 502-10.

89. An, H. and L. He, *Current understanding of metformin effect on the control of hyperglycemia in diabetes.* J Endocrinol, 2016. **228**(3): p. R97-106.

90. Charo, I.F., *Macrophage polarization and insulin resistance: PPARgamma in control.* Cell Metab, 2007. **6**(2): p. 96-8.

91. Sauer, S., *Ligands for the Nuclear Peroxisome Proliferator-Activated Receptor Gamma.* Trends Pharmacol Sci, 2015. **36**(10): p. 688-704.

92. Weidner, C., et al., *Amorfrutins are potent antidiabetic dietary natural products.* Proc Natl Acad Sci U S A, 2012. **109**(19): p. 7257-62.

93. Huvers, F.C., et al., *Improved insulin sensitivity by anti-TNFalpha antibody treatment in patients with rheumatic diseases.* Ann Rheum Dis, 2007. **66**(4): p. 558-9.

94. Marra, M., et al., *Effect of etanercept on insulin sensitivity in nine patients with psoriasis.* Int J Immunopathol Pharmacol, 2007. **20**(4): p. 731-6.

95. Timper, K., et al., *Infliximab in the treatment of Crohn disease and type 1 diabetes.* Diabetes Care, 2013. **36**(7): p. e90-1.

96. Jiang, P., H. Li, and X. Li, *Diabetes mellitus risk factors in rheumatoid arthritis: a systematic review and meta-analysis.* Clin Exp Rheumatol, 2015. **33**(1): p. 115-21.

97. Goldfine, A.B., et al., *The effects of salsalate on glycemic control in patients with type 2 diabetes: a randomized trial.* Ann Intern Med, 2010. **152**(6): p. 346-57.

98. Goldfine, A.B., et al., *Salicylate (salsalate) in patients with type 2 diabetes: a randomized trial.* Ann Intern Med, 2013. **159**(1): p. 1-12.

99. Stegle, O., S.A. Teichmann, and J.C. Marioni, *Computational and analytical challenges in single-cell transcriptomics.* Nat Rev Genet, 2015. **16**(3): p. 133-45.

100. Grun, D. and A. van Oudenaarden, *Design and Analysis of Single-Cell Sequencing Experiments.* Cell, 2015. **163**(4): p. 799-810.

101. Bacher, R. and C. Kendziorski, *Design and computational analysis of single-cell RNA-sequencing experiments.* Genome Biol, 2016. **17**: p. 63.

102. Wu, A.R., et al., *Quantitative assessment of single-cell RNA-sequencing methods.* Nat Methods, 2014. **11**(1): p. 41-6.

References

103. Ramskold, D., et al., *Full-length mRNA-Seq from single-cell levels of RNA and individual circulating tumor cells.* Nat Biotechnol, 2012. **30**(8): p. 777-82.

104. Macosko, E.Z., et al., *Highly Parallel Genome-wide Expression Profiling of Individual Cells Using Nanoliter Droplets.* Cell, 2015. **161**(5): p. 1202-14.

105. Pollen, A.A., et al., *Low-coverage single-cell mRNA sequencing reveals cellular heterogeneity and activated signaling pathways in developing cerebral cortex.* Nat Biotechnol, 2014. **32**(10): p. 1053-8.

106. Andrews, S., *FastQC A Quality Control tool for High Throughput Sequence Data.* http://www.bioinformatics.babraham.ac.uk/projects/fastqc/.

107. Wang, L., S. Wang, and W. Li, *RSeQC: quality control of RNA-seq experiments.* Bioinformatics, 2012. **28**(16): p. 2184-5.

108. Li, H., et al., *The Sequence Alignment/Map format and SAMtools.* Bioinformatics, 2009. **25**(16): p. 2078-9.

109. Anders, S., P.T. Pyl, and W. Huber, *HTSeq--a Python framework to work with high-throughput sequencing data.* Bioinformatics, 2015. **31**(2): p. 166-9.

110. Li, B. and C.N. Dewey, *RSEM: accurate transcript quantification from RNA-Seq data with or without a reference genome.* BMC Bioinformatics, 2011. **12**: p. 323.

111. Trapnell, C., et al., *Transcript assembly and quantification by RNA-Seq reveals unannotated transcripts and isoform switching during cell differentiation.* Nat Biotechnol, 2010. **28**(5): p. 511-5.

112. Shalek, A.K., et al., *Single-cell transcriptomics reveals bimodality in expression and splicing in immune cells.* Nature, 2013. **498**(7453): p. 236-40.

113. Buettner, F., et al., *Computational analysis of cell-to-cell heterogeneity in single-cell RNA-sequencing data reveals hidden subpopulations of cells.* Nat Biotechnol, 2015. **33**(2): p. 155-60.

114. Kolodziejczyk, A.A., et al., *Single Cell RNA-Sequencing of Pluripotent States Unlocks Modular Transcriptional Variation.* Cell Stem Cell, 2015. **17**(4): p. 471-85.

115. Treutlein, B., et al., *Dissecting direct reprogramming from fibroblast to neuron using single-cell RNA-seq.* Nature, 2016. **534**(7607): p. 391-5.

116. Katayama, S., et al., *SAMstrt: statistical test for differential expression in single-cell transcriptome with spike-in normalization.* Bioinformatics, 2013. **29**(22): p. 2943-5.

117. Ding, B., et al., *Normalization and noise reduction for single cell RNA-seq experiments.* Bioinformatics, 2015. **31**(13): p. 2225-7.

118. Tung, P.Y., et al., *Batch effects and the effective design of single-cell gene expression studies.* Sci Rep, 2017. **7**: p. 39921.

119. Grun, D., et al., *Single-cell messenger RNA sequencing reveals rare intestinal cell types.* Nature, 2015. **525**(7568): p. 251-5.

120. Xu, C. and Z. Su, *Identification of cell types from single-cell transcriptomes using a novel clustering method.* Bioinformatics, 2015. **31**(12): p. 1974-80.

121. Pierson, E. and C. Yau, *ZIFA: Dimensionality reduction for zero-inflated single-cell gene expression analysis.* Genome Biol, 2015. **16**: p. 241.

122. Durruthy-Durruthy, R., et al., *Reconstruction of the mouse otocyst and early neuroblast lineage at single-cell resolution.* Cell, 2014. **157**(4): p. 964-78.

123. Pettit, J.B., et al., *Identifying cell types from spatially referenced single-cell expression datasets.* PLoS Comput Biol, 2014. **10**(9): p. e1003824.

124. Brennecke, P., et al., *Accounting for technical noise in single-cell RNA-seq experiments.* Nat Methods, 2013. **10**(11): p. 1093-5.

125. Langfelder, P. and S. Horvath, *WGCNA: an R package for weighted correlation network analysis.* BMC Bioinformatics, 2008. **9**: p. 559.

126. Moore, F.E., et al., *Single-cell transcriptional analysis of normal, aberrant, and malignant hematopoiesis in zebrafish.* J Exp Med, 2016. **213**(6): p. 979-92.

127. Luo, Y., et al., *Single-cell transcriptome analyses reveal signals to activate dormant neural stem cells.* Cell, 2015. **161**(5): p. 1175-86.

128. Li, X., et al., *miR-155 acts as an anti-inflammatory factor in atherosclerosis-associated foam cell formation by repressing calcium-regulated heat stable protein 1.* Sci Rep, 2016. **6**: p. 21789.

129. Cheung, Y.F., et al., *Induction of MCP1, CCR2, and iNOS expression in THP-1 macrophages by serum of children late after Kawasaki disease.* Pediatr Res, 2005. **58**(6): p. 1306-10.

130. Miao, F., et al., *Lymphocytes from patients with type 1 diabetes display a distinct profile of chromatin histone H3 lysine 9 dimethylation: an epigenetic study in diabetes.* Diabetes, 2008. **57**(12): p. 3189-98.

131. Tsuchiya, S., et al., *Establishment and characterization of a human acute monocytic leukemia cell line (THP-1).* Int J Cancer, 1980. **26**(2): p. 171-6.

132. Park, E.K., et al., *Optimized THP-1 differentiation is required for the detection of responses to weak stimuli.* Inflamm Res, 2007. **56**(1): p. 45-50.

133. Choi, S.E., et al., *Capsaicin attenuates palmitate-induced expression of macrophage inflammatory protein 1 and interleukin 8 by increasing palmitate oxidation and reducing c-Jun activation in THP-1 (human acute monocytic leukemia cell) cells.* Nutr Res, 2011. **31**(6): p. 468-78.

134. Bunn, R.C., et al., *Palmitate and insulin synergistically induce IL-6 expression in human monocytes.* Cardiovasc Diabetol, 2010. **9**: p. 73.

135. L'Homme, L., et al., *Unsaturated fatty acids prevent activation of NLRP3 inflammasome in human monocytes/macrophages.* J Lipid Res, 2013. **54**(11): p. 2998-3008.

136. Ye, J., et al., *Primer-BLAST: a tool to design target-specific primers for polymerase chain reaction.* BMC Bioinformatics, 2012. **13**: p. 134.

137. Stahlberg, A., et al., *Defining cell populations with single-cell gene expression profiling: correlations and identification of astrocyte subpopulations.* Nucleic Acids Res, 2011. **39**(4): p. e24.

138. Stahlberg, A. and M. Bengtsson, *Single-cell gene expression profiling using reverse transcription quantitative real-time PCR.* Methods, 2010. **50**(4): p. 282-8.

139. Stahlberg, A., et al., *RT-qPCR work-flow for single-cell data analysis.* Methods, 2013. **59**(1): p. 80-8.

140. Livak, K.J. and T.D. Schmittgen, *Analysis of relative gene expression data using real-time quantitative PCR and the 2(-Delta Delta C(T)) Method.* Methods, 2001. **25**(4): p. 402-8.

141. Bolger, A.M., M. Lohse, and B. Usadel, *Trimmomatic: a flexible trimmer for Illumina sequence data.* Bioinformatics, 2014. **30**(15): p. 2114-20.

142. Harrow, J., et al., *GENCODE: the reference human genome annotation for The ENCODE Project.* Genome Res, 2012. **22**(9): p. 1760-74.

143. Dobin, A., et al., *STAR: ultrafast universal RNA-seq aligner.* Bioinformatics, 2013. **29**(1): p. 15-21.

144. Love, M.I., W. Huber, and S. Anders, *Moderated estimation of fold change and dispersion for RNA-seq data with DESeq2.* Genome Biol, 2014. **15**(12): p. 550.

145. Dennis, G., Jr., et al., *DAVID: Database for Annotation, Visualization, and Integrated Discovery.* Genome Biol, 2003. **4**(5): p. P3.

146. Huang da, W., B.T. Sherman, and R.A. Lempicki, *Systematic and integrative analysis of large gene lists using DAVID bioinformatics resources.* Nat Protoc, 2009. **4**(1): p. 44-57.

147. Julia, M., A. Telenti, and A. Rausell, *Sincell: an R/Bioconductor package for statistical assessment of cell-state hierarchies from single-cell RNA-seq.* Bioinformatics, 2015. **31**(20): p. 3380-2.

148. Dong, J. and S. Horvath, *Understanding network concepts in modules.* BMC Syst Biol, 2007. **1**: p. 24.

149. Zhang, B. and S. Horvath, *A general framework for weighted gene co-expression network analysis.* Stat Appl Genet Mol Biol, 2005. **4**: p. Article17.

150. Pau, G., et al., *EBImage--an R package for image processing with applications to cellular phenotypes.* Bioinformatics, 2010. **26**(7): p. 979-81.

151. Reaven, G.M., et al., *Measurement of plasma glucose, free fatty acid, lactate, and insulin for 24 h in patients with NIDDM.* Diabetes, 1988. **37**(8): p. 1020-4.

152. Karpe, F., J.R. Dickmann, and K.N. Frayn, *Fatty acids, obesity, and insulin resistance: time for a reevaluation.* Diabetes, 2011. **60**(10): p. 2441-9.

153. Glass, C.K. and J.M. Olefsky, *Inflammation and lipid signaling in the etiology of insulin resistance.* Cell Metab, 2012. **15**(5): p. 635-45.

154. Milanski, M., et al., *Saturated fatty acids produce an inflammatory response predominantly through the activation of TLR4 signaling in hypothalamus: implications for the pathogenesis of obesity.* J Neurosci, 2009. **29**(2): p. 359-70.

References

155. Kotani, A., T. Fuse, and F. Kusu, *Determination of plasma free fatty acids by high-performance liquid chromatography with electrochemical detection.* Anal Biochem, 2000. **284**(1): p. 65-9.

156. Zong, G., et al., *Intake of individual saturated fatty acids and risk of coronary heart disease in US men and women: two prospective longitudinal cohort studies.* BMJ, 2016. **355**: p. i5796.

157. Thrush, A.B., et al., *Palmitate acutely induces insulin resistance in isolated muscle from obese but not lean humans.* Am J Physiol Regul Integr Comp Physiol, 2008. **294**(4): p. R1205-12.

158. Pillon, N.J., et al., *Palmitate-induced inflammatory pathways in human adipose microvascular endothelial cells promote monocyte adhesion and impair insulin transcytosis.* Am J Physiol Endocrinol Metab, 2015. **309**(1): p. E35-44.

159. Lancaster, G.I., et al., *PKR is not obligatory for high-fat diet-induced obesity and its associated metabolic and inflammatory complications.* Nat Commun, 2016. **7**: p. 10626.

160. Ramkhelawon, B., et al., *Netrin-1 promotes adipose tissue macrophage retention and insulin resistance in obesity.* Nat Med, 2014. **20**(4): p. 377-84.

161. Kim, S.M., et al., *Role of Inflammatory Signaling in the Differential Effects of Saturated and Poly-unsaturated Fatty Acids on Peripheral Circadian Clocks.* EBioMedicine, 2016. **7**: p. 100-11.

162. Lee, G.H., et al., *Effect of BI-1 on insulin resistance through regulation of CYP2E1.* Sci Rep, 2016. **6**: p. 32229.

163. Traore, K., et al., *Signal transduction of phorbol 12-myristate 13-acetate (PMA)-induced growth inhibition of human monocytic leukemia THP-1 cells is reactive oxygen dependent.* Leuk Res, 2005. **29**(8): p. 863-79.

164. Grishman, E.K., P.C. White, and R.C. Savani, *Toll-like receptors, the NLRP3 inflammasome, and interleukin-1beta in the development and progression of type 1 diabetes.* Pediatr Res, 2012. **71**(6): p. 626-32.

165. Schaeffler, A., et al., *Fatty acid-induced induction of Toll-like receptor-4/nuclear factor-kappaB pathway in adipocytes links nutritional signalling with innate immunity.* Immunology, 2009. **126**(2): p. 233-45.

166. Makita, N., et al., *IL-10 enhances the phenotype of M2 macrophages induced by IL-4 and confers the ability to increase eosinophil migration.* Int Immunol, 2015. **27**(3): p. 131-41.

167. Fujisaka, S., et al., *Regulatory mechanisms for adipose tissue M1 and M2 macrophages in diet-induced obese mice.* Diabetes, 2009. **58**(11): p. 2574-82.

168. Levine, A.J., et al., *Systems analysis of human brain gene expression: mechanisms for HIV-associated neurocognitive impairment and common pathways with Alzheimer's disease.* BMC Med Genomics, 2013. **6**: p. 4.

169. Haas, B.E., et al., *Adipose co-expression networks across Finns and Mexicans identify novel triglyceride-associated genes.* BMC Med Genomics, 2012. **5**: p. 61.

170. Horvath, S., et al., *Aging effects on DNA methylation modules in human brain and blood tissue.* Genome Biol, 2012. **13**(10): p. R97.

171. Thomsen, E.R., et al., *Fixed single-cell transcriptomic characterization of human radial glial diversity.* Nat Methods, 2016. **13**(1): p. 87-93.

172. Xue, Z., et al., *Genetic programs in human and mouse early embryos revealed by single-cell RNA sequencing.* Nature, 2013. **500**(7464): p. 593-7.

173. Oyadomari, S. and M. Mori, *Roles of CHOP/GADD153 in endoplasmic reticulum stress.* Cell Death Differ, 2004. **11**(4): p. 381-9.

174. Willy, J.A., et al., *CHOP links endoplasmic reticulum stress to NF-kappaB activation in the pathogenesis of nonalcoholic steatohepatitis.* Mol Biol Cell, 2015. **26**(12): p. 2190-204.

175. Yao, S., et al., *Oxidized high-density lipoprotein induces macrophage apoptosis via toll-like receptor 4-dependent CHOP pathway.* J Lipid Res, 2016.

176. Krug, U., et al., *Cyclin A1 regulates WT1 expression in acute myeloid leukemia cells.* Int J Oncol, 2009. **34**(1): p. 129-36.

177. Sciesielski, L.K., et al., *Wilms' tumor protein Wt1 regulates the Interleukin-10 (IL-10) gene.* FEBS Lett, 2010. **584**(22): p. 4665-71.

References

178.   Rahman, S.M., et al., *CCAAT/enhancer-binding protein beta (C/EBPbeta) expression regulates dietary-induced inflammation in macrophages and adipose tissue in mice.* J Biol Chem, 2012. **287**(41): p. 34349-60.

179.   Ruffell, D., et al., *A CREB-C/EBPbeta cascade induces M2 macrophage-specific gene expression and promotes muscle injury repair.* Proc Natl Acad Sci U S A, 2009. **106**(41): p. 17475-80.

180.   Poli, V., *The role of C/EBP isoforms in the control of inflammatory and native immunity functions.* J Biol Chem, 1998. **273**(45): p. 29279-82.

181.   Jablonski, K.A., et al., *Novel Markers to Delineate Murine M1 and M2 Macrophages.* PLoS One, 2015. **10**(12): p. e0145342.

182.   Oukka, M., et al., *A mammalian homolog of Drosophila schnurri, KRC, regulates TNF receptor-driven responses and interacts with TRAF2.* Mol Cell, 2002. **9**(1): p. 121-31.

183.   Bouhlel, M.A., et al., *PPARgamma activation primes human monocytes into alternative M2 macrophages with anti-inflammatory properties.* Cell Metab, 2007. **6**(2): p. 137-43.

184.   Lefterova, M.I., et al., *Cell-specific determinants of peroxisome proliferator-activated receptor gamma function in adipocytes and macrophages.* Mol Cell Biol, 2010. **30**(9): p. 2078-89.

185.   Martinon, F., et al., *TLR activation of the transcription factor XBP1 regulates innate immune responses in macrophages.* Nat Immunol, 2010. **11**(5): p. 411-8.

186.   Bettigole, S.E. and L.H. Glimcher, *Endoplasmic reticulum stress in immunity.* Annu Rev Immunol, 2015. **33**: p. 107-38.

187.   Hotz, B., et al., *Beyond epithelial to mesenchymal transition: a novel role for the transcription factor Snail in inflammation and wound healing.* J Gastrointest Surg, 2010. **14**(2): p. 388-97.

188.   Baek, Y.S., et al., *Identification of novel transcriptional regulators involved in macrophage differentiation and activation in U937 cells.* BMC Immunol, 2009. **10**: p. 18.

189.   Gilchrist, M., et al., *Systems biology approaches identify ATF3 as a negative regulator of Toll-like receptor 4.* Nature, 2006. **441**(7090): p. 173-8.

190.   Labzin, L.I., et al., *ATF3 Is a Key Regulator of Macrophage IFN Responses.* J Immunol, 2015. **195**(9): p. 4446-55.

191.   Date, D., et al., *Kruppel-like transcription factor 6 regulates inflammatory macrophage polarization.* J Biol Chem, 2014. **289**(15): p. 10318-29.

192.   Shang, Y., et al., *The transcriptional repressor Hes1 attenuates inflammation by regulating transcription elongation.* Nat Immunol, 2016. **17**(8): p. 930-7.

193.   Feng, W., et al., *Identification and analysis of a conserved Tcfap2a intronic enhancer element required for expression in facial and limb bud mesenchyme.* Mol Cell Biol, 2008. **28**(1): p. 315-25.

194.   Orso, F., et al., *AP-2alpha and AP-2gamma regulate tumor progression via specific genetic programs.* FASEB J, 2008. **22**(8): p. 2702-14.

195.   Krishnaraju, K., et al., *The zinc finger transcription factor Egr-1 potentiates macrophage differentiation of hematopoietic cells.* Mol Cell Biol, 1995. **15**(10): p. 5499-507.

196.   Krishnaraju, K., B. Hoffman, and D.A. Liebermann, *The zinc finger transcription factor Egr-1 activates macrophage differentiation in M1 myeloblastic leukemia cells.* Blood, 1998. **92**(6): p. 1957-66.

197.   Pello, O.M., et al., *Role of c-MYC in alternative activation of human macrophages and tumor-associated macrophage biology.* Blood, 2012. **119**(2): p. 411-21.

198.   Junkins, R.D., et al., *Regulator of calcineurin 1 suppresses inflammation during respiratory tract infections.* J Immunol, 2013. **190**(10): p. 5178-86.

199.   Mendez-Barbero, N., et al., *A major role for RCAN1 in atherosclerosis progression.* EMBO Mol Med, 2013. **5**(12): p. 1901-17.

200.   Frantz, B., et al., *Calcineurin acts in synergy with PMA to inactivate I kappa B/MAD3, an inhibitor of NF-kappa B.* EMBO J, 1994. **13**(4): p. 861-70.

201.   Lin, C.C., et al., *Bhlhe40 controls cytokine production by T cells and is essential for pathogenicity in autoimmune neuroinflammation.* Nat Commun, 2014. **5**: p. 3551.

202.   Roy, S., et al., *Redefining the transcriptional regulatory dynamics of classically and alternatively activated macrophages by deepCAGE transcriptomics.* Nucleic Acids Res, 2015. **43**(14): p. 6969-82.

References

203. Rosales-Avina, J.A., et al., *MEIS1, PREP1, and PBX4 are differentially expressed in acute lymphoblastic leukemia: association of MEIS1 expression with higher proliferation and chemotherapy resistance.* J Exp Clin Cancer Res, 2011. **30**: p. 112.

204. Shortman, K., *How does batf3 determine dendritic cell development?* Immunol Cell Biol, 2015. **93**(8): p. 681-2.

205. Chiu, Y.K., et al., *Transcription factor ABF-1 suppresses plasma cell differentiation but facilitates memory B cell formation.* J Immunol, 2014. **193**(5): p. 2207-17.

206. Avraham, R., et al., *Pathogen Cell-to-Cell Variability Drives Heterogeneity in Host Immune Responses.* Cell, 2015. **162**(6): p. 1309-21.

207. Miranville, A., et al., *Reversal of inflammation-induced impairment of glucose uptake in adipocytes by direct effect of CB1 antagonism on adipose tissue macrophages.* Obesity (Silver Spring), 2010. **18**(12): p. 2247-54.

208. Ortega, F.J., et al., *Inflammation triggers specific microRNA profiles in human adipocytes and macrophages and in their supernatants.* Clin Epigenetics, 2015. **7**: p. 49.

209. Unoki, H., et al., *Macrophages regulate tumor necrosis factor-alpha expression in adipocytes through the secretion of matrix metalloproteinase-3.* Int J Obes (Lond), 2008. **32**(6): p. 902-11.

210. Bouckenooghe, T., et al., *Adipose tissue macrophages (ATM) of obese patients are releasing increased levels of prolactin during an inflammatory challenge: a role for prolactin in diabesity?* Biochim Biophys Acta, 2014. **1842**(4): p. 584-93.

211. Qin, Z., *The use of THP-1 cells as a model for mimicking the function and regulation of monocytes and macrophages in the vasculature.* Atherosclerosis, 2012. **221**(1): p. 2-11.

212. Lun, A.T., D.J. McCarthy, and J.C. Marioni, *A step-by-step workflow for low-level analysis of single-cell RNA-seq data with Bioconductor.* F1000Res, 2016. **5**: p. 2122.

213. Ahmadian, M., et al., *PPARgamma signaling and metabolism: the good, the bad and the future.* Nat Med, 2013. **19**(5): p. 557-66.

214. Pless, O., et al., *G9a-mediated lysine methylation alters the function of CCAAT/enhancer-binding protein-beta.* J Biol Chem, 2008. **283**(39): p. 26357-63.

215. Cesena, T.I., et al., *Acetylation and deacetylation regulate CCAAT/enhancer binding protein beta at K39 in mediating gene transcription.* Mol Cell Endocrinol, 2008. **289**(1-2): p. 94-101.

216. Lim, R., et al., *ATF3 is a negative regulator of inflammation in human fetal membranes.* Placenta, 2016. **47**: p. 63-72.

217. Wang, J., et al., *ATF3 inhibits the inflammation induced by Mycoplasma pneumonia in vitro and in vivo.* Pediatr Pulmonol, 2017.

218. Lin, H., et al., *Activating transcription factor 3 protects against pressure-overload heart failure via the autophagy molecule Beclin-1 pathway.* Mol Pharmacol, 2014. **85**(5): p. 682-91.

219. Qian, L., et al., *Activating transcription factor 3 (ATF3) protects against lipopolysaccharide-induced acute lung injury via inhibiting the expression of TL1A.* J Cell Physiol, 2017.

220. Rosenberger, C.M., et al., *ATF3 regulates MCMV infection in mice by modulating IFN-gamma expression in natural killer cells.* Proc Natl Acad Sci U S A, 2008. **105**(7): p. 2544-9.

221. Nguyen, T.T., et al., *Differential gene expression downstream of Toll-like receptors (TLRs): role of c-Src and activating transcription factor 3 (ATF3).* J Biol Chem, 2010. **285**(22): p. 17011-9.

222. Kwon, J.W., et al., *Activating transcription factor 3 represses inflammatory responses by binding to the p65 subunit of NF-kappaB.* Sci Rep, 2015. **5**: p. 14470.

223. Peiris, H., et al., *A Syntenic Cross Species Aneuploidy Genetic Screen Links RCAN1 Expression to beta-Cell Mitochondrial Dysfunction in Type 2 Diabetes.* PLoS Genet, 2016. **12**(5): p. e1006033.

224. Zenobi, R., *Single-cell metabolomics: analytical and biological perspectives.* Science, 2013. **342**(6163): p. 1243259.

225. Macaulay, I.C., C.P. Ponting, and T. Voet, *Single-Cell Multiomics: Multiple Measurements from Single Cells.* Trends Genet, 2017. **33**(2): p. 155-168.

226. Macaulay, I.C., et al., *G&T-seq: parallel sequencing of single-cell genomes and transcriptomes.* Nat Methods, 2015. **12**(6): p. 519-22.

227. Gawad, C., W. Koh, and S.R. Quake, *Single-cell genome sequencing: current state of the science.* Nat Rev Genet, 2016. **17**(3): p. 175-88.

228.   Clark, S.J., et al., *Single-cell epigenomics: powerful new methods for understanding gene regulation and cell identity.* Genome Biol, 2016. **17**: p. 72.

229.   Cabili, M.N., et al., *Localization and abundance analysis of human lncRNAs at single-cell and single-molecule resolution.* Genome Biol, 2015. **16**: p. 20.

230.   Moffitt, J.R., et al., *High-throughput single-cell gene-expression profiling with multiplexed error-robust fluorescence in situ hybridization.* Proc Natl Acad Sci U S A, 2016. **113**(39): p. 11046-51.

231.   Satija, R., et al., *Spatial reconstruction of single-cell gene expression data.* Nat Biotechnol, 2015. **33**(5): p. 495-502.

232.   Halpern, K.B., et al., *Single-cell spatial reconstruction reveals global division of labour in the mammalian liver.* Nature, 2017. **542**(7641): p. 352-356.

233.   *Human Cell Atlas*. 2017; Available from: https://www.humancellatlas.org/.